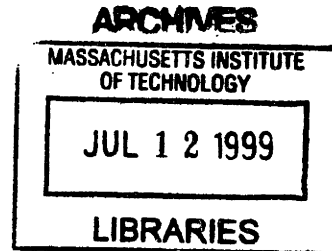


# CREEP CHARACTERIZATION OF SINGLE CRYSTAL SILICON IN SUPPORT OF THE MIT MICRO-ENGINE PROJECT

By

Douglas S. Walters  
B.S. Mechanical Engineering  
Clarkson University, 1995

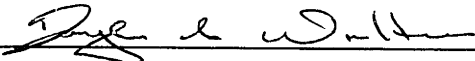


Submitted to the Department of Mechanical Engineering in Partial Fulfillment of the Requirements for the Degree of

MASTERS OF SCIENCE IN MECHANICAL ENGINEERING  
at the  
MASSACHUSETTS INSTITUTE OF TECHNOLOGY

JUNE 1999

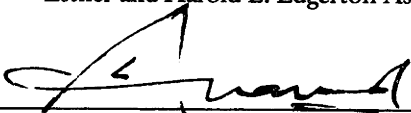
©Massachusetts Institute of Technology 1999, All Rights Reserved

Signature of Author 

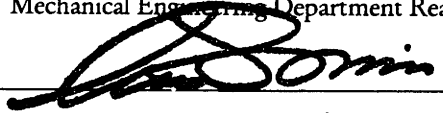
Department of Mechanical Engineering  
May 24, 1999

Certified by 

Prof. S. Mark Spearing  
Esther and Harold E. Edgerton Assistant Professor of Aeronautics and Astronautics  
Thesis Advisor

Certified by 

Prof. Lallit Anand  
Professor of Mechanical Engineering  
Mechanical Engineering Department Reader

Accepted by 

Prof. Ain A. Sonin  
Professor of Mechanical Engineering  
Chairman, Department Committee on Graduate Students

# Creep Characterization of Single Crystal Silicon in Support of the MIT Micro-Engine Project

by

Douglas S. Walters

Submitted to the Department of Mechanical Engineering on May 24, 1999  
in Partial Fulfillment of the Requirements for the Degree of Master of  
Science in Mechanical Engineering

## ABSTRACT

In 1995, a program was initiated at the Massachusetts Institute of Technology (MIT) to develop the technology to design and manufacture a micro-gas turbine generator. The objective of the research is to demonstrate a full-scale, functional micro-gas turbine generator by the year 2000. To meet this milestone, the first engine to test will be constructed of single-crystal silicon. Due to its low brittle-to-ductile transition temperature, silicon is not ideal for a production engine. However, the microfabrication technology for silicon is far more advanced than other candidate materials making it the best short-term option. In support of the micro-engine project, this thesis investigates the high temperature creep capability of silicon. The goal of the investigation is to develop a creep relationship upon which the demonstration engine can be designed.

The proposed micro-turbine will initially be designed for a power generation application. With a 20 mm diameter and 4 mm axial length, the micro-engine should be able to generate electrical power at over 10 times the power density of a comparably sized battery. Other applications for this technology have been identified, including; propulsion for small unmanned air vehicles, boundary layer control, a micro-turbine expander for miniature cooling systems, a turbo pump for micro-rocket engines, and a micro-motor driven pump or compressor for fluid handling applications.

To characterize the creep behavior, representative samples of single-crystal silicon were tested in bending using a silicon carbide 4-point bend fixture. For a given applied stress, tests were run at several temperatures between 600 and 850°C. The creep of specimens in this temperature range was dominated by localized deformation at the inner loading point. Etching of the specimens revealed a high density of slip bands on the  $\langle 111 \rangle$  planes at these locations. The overall specimen deformation proceeded via the formation of "plastic hinges" at the inner loading points. The localized nature of the creep response is not amenable to the application of standard continuum power law models, however an empirical Larson-Miller fit was applied in order to provide some guidance for micro-engine design.

Finally, it is important to note the implications that the observed specimen plastic collapse has for the design of the micro-engine. The strain-softening characteristic of yielding silicon must be accounted for in the detailed design. Improper treatment of localized stress concentrations could result in premature engine failure.

Thesis Supervisor: Prof. S. Mark Spearing

Title: Esther and Harold E. Edgerton Assistant Professor of Aeronautics and Astronautics

This thesis is dedicated to my wife

Jackie

without your support and understanding, this would not have  
been possible.



This thesis would not be complete without taking the time to thank those that made it possible. First and foremost, thanks to my advisor Mark Spearing for presenting me with the opportunity to work on the micro-engine team. Your support and willingness to accommodate my professional work schedule were greatly appreciated. Also, thanks to Lallit Ananad, who provided invaluable technical input and took time to read my thesis on behalf of the Mechanical Engineering department.

Additional special thanks are warranted to John Kane for his guidance in TELAC; Kuo-Shen Chen for sharing his knowledge, experience and time; and Kevin Lohner for spending many valuable hours to get me started on the right foot. Also, thanks go out to my family for their endless support and encouragement; Leslie Regan in the Mechanical Engineering Graduate Office; Alan Epstein and the MIT Micro-Engine team, including Todd Harrison, Bruno Miller, Jonathan Protz and Wenjing Ye; Carl Brown, Don Steeves and Al Dix in the General Electric Aircraft Engines (GEAE) Thompson Lab; my GEAE managers, for allowing me the flexibility to attend daytime classes, the GEAE Advanced Course Staff, including Martha Learned and Peter Rock, for giving me this educational opportunity; GEAE Chief Engineer Dave Klaasen; and my fellow GEAE Technical Leadership Program members attending MIT, including Brent Brunell, Alan Grissino and Garth Grover.

# TABLE OF CONTENTS

ABSTRACT .....	ii
TABLE OF CONTENTS .....	iv
LIST OF FIGURES .....	vi
LIST OF TABLES .....	viii
CHAPTER 1 INTRODUCTION .....	9
1.1 MICROENGINE PROJECT OVERVIEW .....	9
1.2 MICROENGINE DESIGN AND MATERIAL CONSIDERATIONS .....	10
1.3 THESIS CONTRIBUTIONS .....	11
CHAPTER 2 CREEP CHARACTERIZATION - BACKGROUND .....	12
2.1 CREEP MECHANISMS .....	12
2.2 CREEP MODELS .....	16
2.3 SILICON CREEP CHARACTERIZATION .....	17
2.4 BRITTLE MATERIAL CREEP TESTING .....	21
1.1.1 AVAILABLE TESTING METHODOLOGIES .....	21
2.4.2 4-POINT BEND TEST TECHNIQUES - A LITERATURE REVIEW .....	23
CHAPTER 3 CREEP TEST SETUP AND METHODOLOGY .....	27
3.1 TEST EQUIPMENT .....	27
3.1.1 THE LOADING APPARATUS .....	27
3.1.2 THE HEATING UNIT .....	27
3.1.3 THE SENSING MECHANISMS .....	28
3.1.4 THE DATA ACQUISITION EQUIPMENT .....	28
3.2 TEST PROCEDURE .....	33
3.2.1 SPECIMEN PREPARATION AND SETUP .....	33
3.2.2 LOADING CONDITIONS .....	33
3.2.3 DATA COLLECTION AND STORAGE .....	34
3.2.4 METALLOGRAPHY .....	36

<b>CHAPTER 4 RESULTS.....</b>	<b>37</b>
4.1 CREEP TEST DATA.....	37
4.2 DATA REDUCTION.....	42
4.2.1 <i>HOLLENBERG ET AL. POWER LAW APPROACH</i> .....	42
4.2.2 <i>FINITE ELEMENT ANALYSIS CORRELATION</i> .....	47
4.2.3 <i>FINITE ELEMENT ANALYSIS REALITY CHECK</i> .....	49
4.3 PLASTIC HINGE INVESTIGATION.....	50
4.3.1 <i>DISLOCATION PILE-UP</i> .....	50
4.3.2 <i>SOURCES OF STRESS</i> .....	56
<b>CHAPTER 5 DISCUSSION.....</b>	<b>62</b>
5.1 IMPLICATIONS FOR THE MICROENGINE PROJECT.....	62
5.2 IMPROVED CREEP TEST SUGGESTIONS.....	66
5.2.1 <i>MODIFIED 4-POINT BEND TEST</i> .....	66
5.2.2 <i>COMPRESSION TEST</i> .....	68
5.3 MODELING.....	69
5.4 IMPACT ON THE MICRO-ENGINE DESIGN.....	70
<b>CHAPTER 6 CONCLUSIONS.....</b>	<b>71</b>
6.1 SUMMARY.....	71
6.2 CONCLUSIONS.....	72
6.3 FUTURE WORK.....	72
<b>APPENDIX.....</b>	<b>74</b>
<b>REFERENCES.....</b>	<b>135</b>

## LIST OF FIGURES

Figure 1.1.1: Demonstration micro-gas turbine engine schematic. ....	10
Figure 2.1.1: Typical three-stage creep curve. ....	12
Figure 2.1.2: Typical creep deformation-mechanism map. ....	15
Figure 2.1.3: Deformation mechanism map for silicon of grain size 100 $\mu\text{m}$ (compiled by Ashby and Frost <sup>8</sup> ). ....	15
Figure 2.3.1: A typical creep curve of D.S. crystals. ....	18
Figure 2.3.2: Myshlyaev et al. creep rate plotted versus temperature for stresses of 50 (1), 60 (2), 70 (3), 80 (4), 90 (5), and 100 MPa (6).....	20
Figure 2.4.1: Specimen shapes for direct tensile testing. (a) "Dog bone" shape. (b) Cylindrical "buttonhead" shape.....	22
Figure 2.4.2: Flexural testing types. (a) 3-point bending. (b) 4-point bending.....	23
Figure 2.4.3: Shear-Moment diagram for a 4-point bend test. ....	25
Figure 3.1.1: MTS 810 material testing system with split cylindrical furnace.....	29
Figure 3.1.2: Silicon Carbide 4-Point bend fixture. ....	30
Figure 3.1.3: INSTRON <sup>TM</sup> 8500 electronic controller.....	31
Figure 3.1.4: Furnace temperature controller.....	32
Figure 3.1.5: Labview <sup>TM</sup> interface screen. ....	32
Figure 3.2.1: Silicon test specimen dimensions.....	33
Figure 3.2.2: Test Procedure Flowchart. ....	35
Figure 4.1.1: Silicon creep test matrix.....	37
Figure 4.1.2: Raw test data at 750°C and 30 N. ....	38
Figure 4.1.3: Location of incremental test points at 700°C and 45 N. ....	39

Figure 4.1.4: Incremental test at 700°C and 45N, displacement versus time plots. Centerpoint deflections prior to unload are (a) -0.50 mm, (b) -0.76 mm, (c) -1.21 mm, and (d) 1.88 mm. ....	40
Figure 4.1.5: Silicon incremental test specimens sideviews. Centerpoint deflections prior to unload are (a) -0.50 mm, (b) -0.76 mm, (c) -1.21 mm, and (d) 1.88 mm.....	41
Figure 4.1.6: Profilometer traces of deformed shapes of specimens shown in Figure 4.1.5. Centerpoint deflections prior to unload are (a) -0.50 mm, (b) -0.76 mm, (c) -1.21 mm, and (d) 1.88 mm.....	41
Figure 4.2.1: Displacement rate versus time plot at 750°C and 30N.....	43
Figure 4.2.2: Plot to determine the creep exponent n. ....	44
Figure 4.2.3: Strain Rate versus Time Plot at 750°C and 30N. ....	45
Figure 4.2.4: Plot to determine the creep ratio Q/R.....	46
Figure 4.2.5: Fintite element model.....	48
Figure 4.2.6: 700°C interval test specimen profiles. ....	49
Figure 4.3.1: Silicon load vs. deflection curve at 800°C.....	51
Figure 4.3.2: Silicon specimen inner load-point surface (SEM image). (a) 100X, (b) 1000X, (c) 1000X away from load-point. ....	53
Figure 4.3.3: Magnified views of the specimen cross-section. (a) 20X, (b) 100X, (c) SEM image near top, 1000X. Photos are not to scale. ....	55
Figure 4.3.4: Creep test stresses versus yield strength.....	56
Figure 4.3.5: Contact stresses between two cylinders.....	58
Figure 4.3.6: Contact + maximum bending stress versus yield strength. ....	59
Figure 4.3.7: 700°C yield test specimen profiles.....	60
Figure 4.3.8: Yield test specimens inner load-point surface (SEM images). (a) 100X, (b) 1000X.....	61
Figure 5.1.1: Turbine temperatures (K) .....	62
Figure 5.1.2: Fillet radius tradeoff study.....	63
Figure 5.1.3: Plot to determine Larson-Miller Parameter C.....	64

Figure 5.1.4: Larson-Miller Parameter design curve.....65  
Figure 5.2.1: Modified 4-point bend test method. ....67  
Figure 5.2.2: Typical compression fixture. ....68

## LIST OF TABLES

Table 4.1.1: Assumed load-to-stress equivalents. ....37



# CHAPTER 1 INTRODUCTION

## 1.1 MICROENGINE PROJECT OVERVIEW

In 1995, the Massachusetts Institute of Technology (MIT) received funding from the U.S. Army Research Office to pursue the design and manufacture of a micro-gas turbine generator. The scale of the proposed turbine is to be approximately 20 mm in diameter by 4 mm in axial length. Analysis predicts that a micro-engine of this scale could generate electrical power at over 10 times the power density of the best comparably sized battery<sup>1</sup>. The objective of the research is to develop the necessary micro-engine technology base and demonstrate a full-scale, functional micro-gas turbine generator by the year 2000.

Preliminary design studies, performed at the inception of the project, suggest that a micro-engine of this scale could ultimately produce 50-100W of power. This estimate assumes the micro-engine to be running with efficiencies equivalent to those of a modern, large scale, gas turbine<sup>2</sup>. However, the goal for the first engine to test on this project is a more feasible power of 10W.

A "demonstration engine" has been designed as shown in Figure 1.1.1. This configuration consists of a single spool centrifugal flow compressor and turbine. The engine will consume 11-15 g/hr of gaseous H<sub>2</sub> and spin at 1.2 million rpm on gas bearings. The combustor exit gas temperature will exceed 1600K. The demonstration engine will not have any electrical machinery, and could be used as the baseline for thrust producing devices for propulsion or flow-control applications. Additional engine configuration information is included in APPENDIX A.1. The challenge to obtain this level of performance is being undertaken by a team of faculty and students, organized in a manner to simulate an actual jet engine manufacturing company.

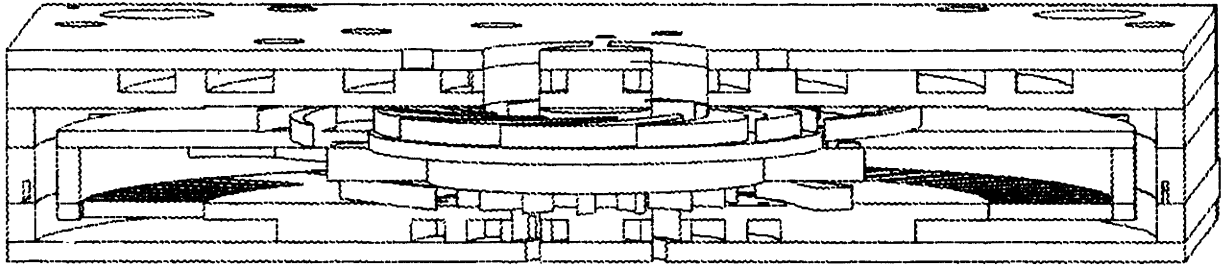


Figure 1.1.1: Demonstration micro-gas turbine engine schematic.

In addition to the micro-gas turbine generator project, several other applications of this micro-machine technology have been identified for further research and development. Among those offshoot projects are a micro-jet engine for small unmanned air vehicles and control of boundary layers in large aircraft or engines, a micro-turbine expander for miniature cooling systems, a turbo pump for micro-rocket engines, and a micro-motor driven pump or compressor for fluid handling applications.

## 1.2 MICROENGINE DESIGN AND MATERIAL CONSIDERATIONS

Considering the high combustor exit temperature and a calculated maximum rotor stress on the order of 100 MPa for the demonstration engine, proper material selection is critical. In most turbine applications, performance is limited by material capability. The micro-engine is no exception. The chosen material must have a high strength to density ratio to withstand the severe centrifugal loads and be capable of resisting creep at high operating temperatures.

The most promising class of materials for the micro-engine application are ceramics. Ceramics have relatively low densities compared to the metals used in conventional large-scale gas turbine engines, but maintain a high stiffness, a high strength and a low coefficient of thermal expansion, over a wider range of temperatures<sup>1</sup>. Ceramics have been used sparingly in large-scale applications due to their low fracture toughness. However, the ability to resist fracture has proven to be scale dependent<sup>3,4,5</sup>. As parts get smaller, their fracture strength increases. Therefore, ceramics are an attractive option for use in the micro-engine. Unfortunately, the technology for micro-fabrication of the most refractory ceramics (SiC, Si<sub>3</sub>N<sub>4</sub>, Al<sub>2</sub>O<sub>3</sub>) is still in its

infancy. At the present time, there is no proven method for generating the smallest details of the micro-engine, which have scales on the order of 1-10 $\mu$ m, out of preferred ceramic materials such as silicon carbide (SiC).

The difficulties associated with ceramic micro-fabrication led to the investigation of single crystal silicon (Si) as a short-term substitute. Due to the wide use of silicon in microelectromechanical systems (MEMS) applications, silicon micro-fabrication techniques are highly developed and thus can be more easily adapted to the construction of a micro-engine than those of silicon carbide. Therefore, in order to meet the contract commitment to demonstrate the demonstration engine by the year 2000, silicon was chosen as the primary engine material. Silicon has superior specific strength characteristics to that of silicon carbide at low temperatures, and comparable specific stiffness. Unfortunately, silicon has a brittle-to-ductile transition temperature (BDTT) of only 550°C<sup>6</sup>, making it susceptible to creep at relatively low temperatures in comparison to the engine operating environment. To this date, very little work has been done to characterize the creep properties of silicon in the temperature and stress envelopes of the micro-engine. The purpose of this thesis is to develop a constitutive relation to describe the creep characteristics of silicon for use in designing the demonstration micro-engine.

### 1.3 THESIS CONTRIBUTIONS

The lack of available creep data for single-crystal silicon prompted the MIT micro-engine team to initiate a series of creep characterization tests. Material behavior is paramount to the overall performance of the micro-engine, therefore accurate material data is essential. This thesis documents the results obtained from the silicon creep experiments performed at MIT in support of the micro-engine project. Plastic collapse, due to local load point stress concentrations, was observed in the creep specimens. This phenomenon prohibited the development of constitutive equations, which could be used to design the engine. However, with the unexpected results come great insight into the high temperature behavior of silicon and its impact on the design requirements of the micro-engine. In addition, methods for supplementary creep testing are outlined.

## CHAPTER 2 . CREEP CHARACTERIZATION - BACKGROUND

### 2.1 CREEP MECHANISMS

When a material is heated to greater than approximately 40% of its homologous melting temperature and a constant stress is applied, significant deformation can occur over time<sup>7</sup>. This rate-dependent deformation is known as creep and if sustained will ultimately lead to component failure. In many materials the entire creep process can be broken down into three distinct regimes; primary, secondary and tertiary as shown in Figure 2.1.1. The primary stage is characterized by a decelerating rate of deformation; the secondary stage exhibits a steady-state creep rate; and the tertiary stage has an accelerating creep rate that often results in material rupture. Although the three-stage creep definition is common for many materials it is not always appropriate.

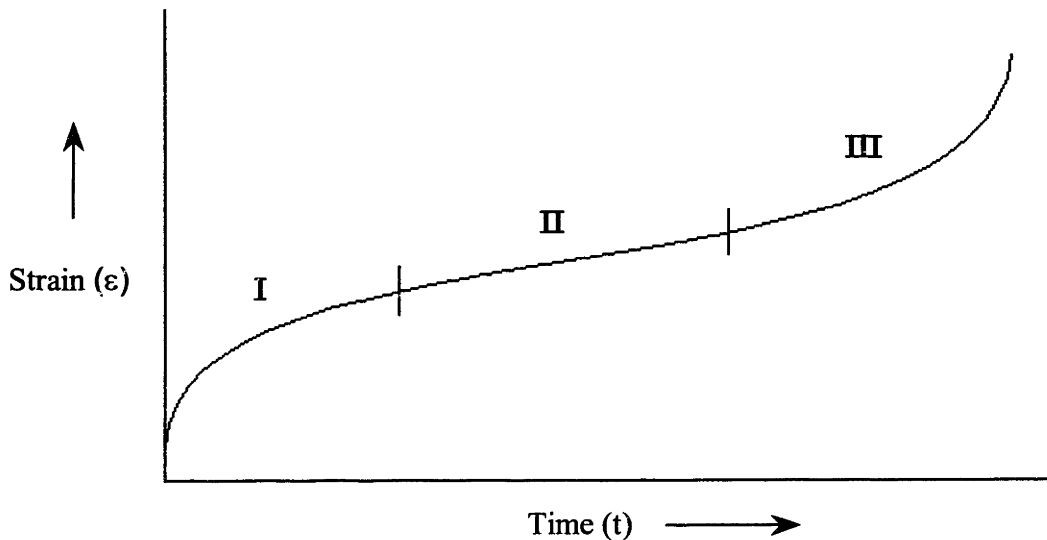


Figure 2.1.1: Typical three-stage creep curve.

The mechanisms causing creep deformation vary depending on the material microstructure, loading temperature and stress level. Some of the more common mechanisms are described in

the following paragraphs.

#### DISLOCATION GLIDE:

Although creep is generally thought of as a high temperature phenomenon, given sufficient stress levels, creeping dislocation glide can occur at relatively low temperatures. As a dislocation travels along a glide plane it will invariably encounter obstacles. During dislocation glide creep, thermal energy supplies a dislocation with the additional activation energy it needs to bypass the obstacle. Using chemical kinetic principles, the dislocation glide creep rate can be approximated by<sup>10</sup>,

$$\dot{\epsilon} = \dot{\epsilon}_0 \exp\left(-\frac{U_0}{kT}\right) \exp\left(\frac{\tau b a_s}{kT}\right) \quad (2.1.1)$$

where,  $\dot{\epsilon}_0$  is a material parameter,  $U_0$  is the work required to overcome the obstacle,  $\tau$  is the applied stress,  $b$  is the Burgers vector,  $a_s$  is the slip plane area,  $k$  is the gas constant and  $T$  is the temperature. The process of dislocation glide creep involves no diffusional flow mechanisms.

#### DIFFUSIONAL FLOW CREEP:

Diffusional flow creep can be subdivided into two separate mechanisms; Nabarro-Herring Creep and Coble Creep. Nabarro-Herring Creep is the opposite of dislocation glide in that it is accomplished entirely through diffusional mass transport<sup>10</sup>. This type of diffusional creep is prevalent in regimes of low stress and high temperature. As a material is subjected to stress, a shift is seen in the atomic volumes. Areas of tensile stress experience an increase in volume, while areas of compressive stress experience a decrease. A difference in vacancy concentrations between the tensile and compressive regions results in vacancy flow. To maintain equilibrium, there is an equal mass flow in the opposite direction. The result is grain elongation and thus creep. The creep rate for Nabarro-Herring Creep can be represented as,

$$\dot{\epsilon} = A_{NH} \left(\frac{D_L}{d^2}\right) \left(\frac{\sigma \Omega}{kT}\right) \quad (2.1.2)$$

where,  $A_{NH}$  is a geometrical factor,  $D_L$  is the lattice self-diffusion coefficient,  $d$  is the grain size, and  $\Omega$  is the atomic volume.

Coble Creep is closely related to Nabarro-Herring Creep in that it is driven by the same vacancy concentration gradient<sup>10</sup>. The difference in Coble Creep is that the mass flux is directed along the grain boundaries for polycrystals and along the surface for single crystals. The equation for Coble Creep is given by,

$$\dot{\epsilon} = A_C \left( \frac{D_{GB} \delta'}{d^3} \right) \left( \frac{\sigma \Omega}{kT} \right) \quad (2.1.3)$$

where,  $A_C$  is a geometrical factor,  $D_{GB}$  is the grain boundary (or surface) diffusivity, and  $\delta'$  is the grain boundary thickness. Like Nabarro-Herring Creep, Coble Creep is dominant in a low stress, high temperature environment, but clearly there are differences in the two mechanisms, most notably grain size effects. Due to the higher exponent value, Coble Creep is much more sensitive to grain size. Since there is an inverse relationship between creep rate and grain size, it is likely that Coble Creep will dominate in materials of particularly small grain size.

#### DISLOCATION CREEP:

For many materials, dislocation creep dominates over a broad range of moderate stresses and temperatures. Although several mechanisms to describe this type of creep have been postulated, there is little experimental evidence of their applicability<sup>10</sup>. However, it is known that there is a strong dependence on stress magnitude in dislocation creep. Unlike the diffusional flow creep mechanisms that have a linear dependence on stress, dislocation creep has a stress exponent typically in the range of 3 to 7. The power law creep model, described later in section 2.2, is often an effective tool for fitting experimental data in the dislocation creep range.

To track the different creep regimes for a given material, deformation-mechanism maps have been created. These graphs plot temperature, normalized by the melting temperature, versus the natural log of stress, normalized by the shear modulus. A typical deformation-mechanism map is shown in Figure 2.1.2. Ashby and Frost<sup>8</sup> have compiled information and generated deformation-mechanism maps for a wide range of materials including silicon. Their map of silicon, as presented in Figure 2.1.3, shows that in the operating temperature and stress ranges of the micro-engine, silicon creep is expected to be dominated by power law dislocation

mechanisms. Note that this map is constructed for polycrystalline silicon, but that single-crystal data is overlaid.

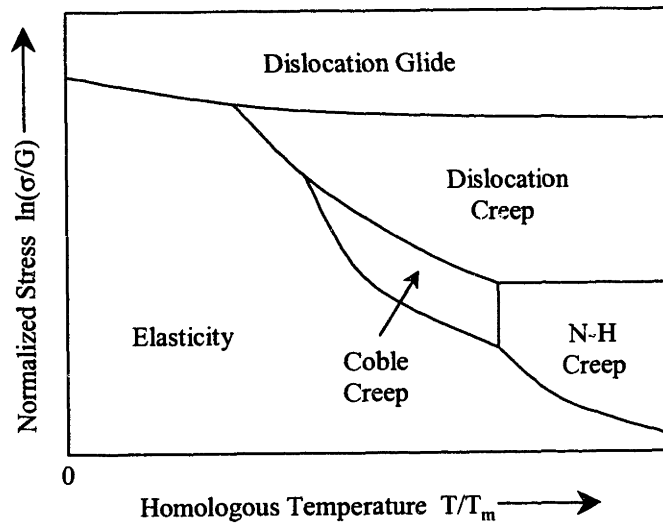


Figure 2.1.2: Typical creep deformation-mechanism map.

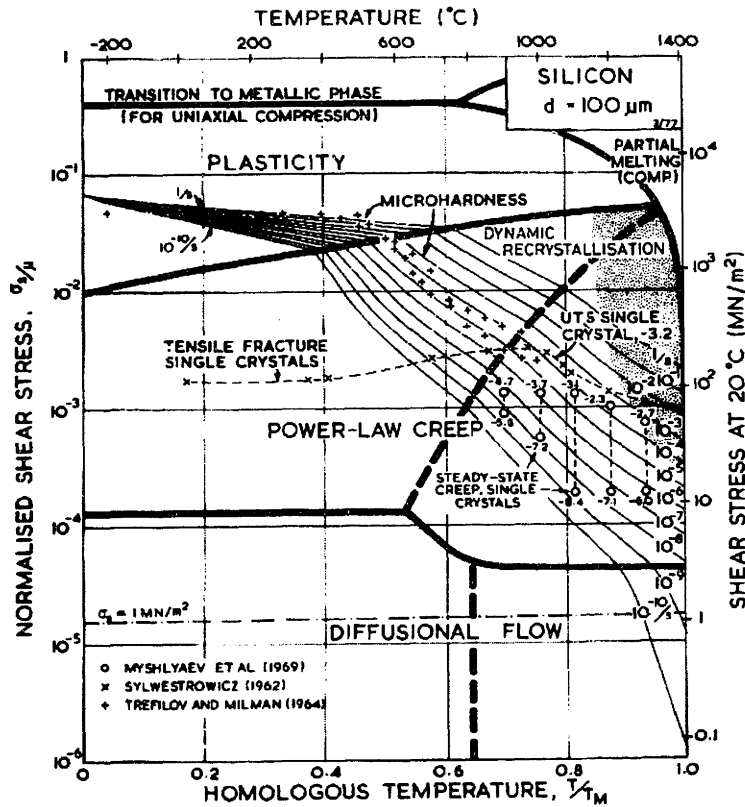


Figure 2.1.3: Deformation mechanism map for silicon of grain size  $100 \mu\text{m}$  (compiled by Ashby and Frost<sup>8</sup>).

## 2.2 CREEP MODELS

To effectively design components with sufficient creep life for high temperature applications, an engineer must be able to characterize the creep growth rate. Much work has been done to develop empirical models that accurately describe this deformation phenomenon. Traditionally, the models have concentrated on describing only the steady-state portion of the creep curve. This method has proven successful over the past thirty years in many applications where part life is expired prior to tertiary creep due to achieving a specified accumulated strain level. Unfortunately, these models have no means to characterize the primary stage incubation period and can thus be overly conservative. However, recently some success has been achieved in developing relationships to describe the entire creep strain curvature. Two of the more common methodologies are described in the following paragraphs.

### POWER LAW CREEP:

The power law relationship for describing steady-state creep is a commonly used model. The underlying assumption in the power law model is that the strain rate ( $\dot{\epsilon}$ ) is an independent function of stress ( $\sigma$ ) and temperature ( $T$ ) such that<sup>9</sup>,

$$\dot{\epsilon} = u(\sigma) \cdot v(T) \quad (2.2.1)$$

Although there is more than one interpretation of what these functions of stress and temperature should be, by far the most common are,

$$u(\sigma) \propto \sigma^n \quad (2.2.2)$$

$$v(T) \propto \exp\left(-\frac{Q}{RT}\right) \quad (2.2.3)$$

Substituting the functions  $u$  and  $v$  into equation 2.2.1 yields the power law equation for creep,

$$\dot{\epsilon} = A\sigma^n \exp\left(-\frac{Q}{RT}\right) \quad (2.2.4)$$

where  $A$  is a constant of proportionality,  $n$  is a constant exponent,  $Q$  is the creep activation



energy and R is the gas constant. Although A, n and Q are often thought of as constants, in actuality they are generally all found to be weak functions of stress and temperature. Fortunately, over limited ranges of stress and temperature, they can often be considered constant. In addition, when the material temperature is greater than half of the melting temperature, Q behaves independent of stress and temperature and is approximately equal to the energy for self-diffusion<sup>10</sup>.

### $\theta$ PROJECTION CONCEPT:

To address the shortcomings inherent in the power law creep methodology, significant effort has gone to developing a general equation describing the entirety of the three-stage creep curve. One such method, which is currently receiving much attention, is the  $\theta$  Projection Concept. This method is molded around the notion that the entire three-stage creep curve can be modeled as the sum of a decaying primary stage and an accelerating tertiary stage<sup>9</sup>. Using this method, the strain as a function of time is described as,

$$\varepsilon = \theta_1(1 - e^{-\theta_2 t}) + \theta_3(e^{\theta_4 t} - 1) \quad (2.2.5)$$

The constants  $\theta_1$  and  $\theta_2$  are scaling factors relating to the primary and tertiary components of the creep curve respectively. The exponential powers  $\theta_3$  and  $\theta_4$  define the deceleration and acceleration of the primary and tertiary stages respectively. Each of these parameters relates to stress and temperature by the general equation,

$$\ln \theta_i = a_i + b_i \sigma + c_i T + d_i \sigma T \quad (2.2.6)$$

Constant stress creep tests can be used to determine the values of each of the 20 coefficients (5 for each of the 4 values of  $\theta$ ), so given the stress and temperature, a creep curve can be generated.

### 2.3 SILICON CREEP CHARACTERIZATION

Although, to date, there is limited creep data available for silicon, there have been some experiments run over limited stress and temperature ranges. Most of the data comes from a series of tests performed in the late 1960's and early 1970's. The most notable of this work comes

from Alexander and Haasen<sup>11</sup>, Myshlyayev et al.<sup>12</sup>, and Taylor and Barrett<sup>13</sup>. Details of the contributions from each of these papers are described in the following paragraphs.

#### ALEXANDER AND HAASEN:

Alexander and Haasen<sup>11</sup> explored dislocations in materials with the diamond cubic structure (D.S.). A portion of the paper is devoted to creep experimentation with particular focus on single-crystal silicon. The creep tests were performed in bending over a temperature range of 800 to 940°C and a shear stress range of 2 to 7 MPa. The experiments revealed an accelerating primary stage and decelerating tertiary stage resulting in an S-shaped creep curve similar to that shown in Figure 2.3.1. Although this shape differs greatly from the classic three-stage creep curve (Figure 2.1.1) Alexander and Haasen found this shape consistent among D.S. crystals. In addition, extraction of a power law model was possible, due to the steady-state secondary stage.

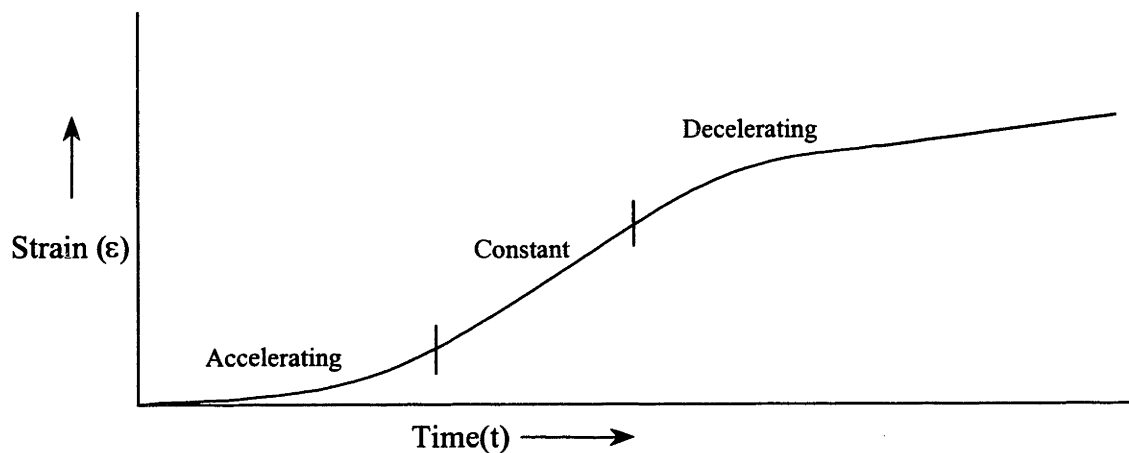


Figure 2.3.1: A typical creep curve of D.S. crystals.

Based on the power law model, Alexander and Haasen derive from their experiments an exponential power coefficient  $n=3$  and an activation energy  $Q=232$  kJ/mol. A proportionality constant,  $A$ , was not evaluated in the study.

#### MYSHLYAEV ET AL.:

Myshlyayev et.al.<sup>12</sup>, writing one year after Haasen and Alexander in 1969, concentrated solely on the creep of silicon. Single-crystal silicon was tested under uniaxial compression in an argon

atmosphere. The tests ranged in temperature from 900 to 1300°C and in stress from 20 to 147 MPa. As Alexander and Haasen had observed, Myshlyaev et al. found the creep curve to have an S-shape. However, Myshlyaev et al. also noted that the tertiary stage, at significantly low pressures and temperatures, eventually settled at a constant rate and remained there through the completion of the test, as presented in Figure 2.3.1. In addition, at sufficiently high pressures and temperatures, the specimens followed the classic three-stage creep curve. These tests ended with an accelerating tertiary stage culminating in rupture.

Myshlyaev et al. focused their results on the steady-state portion of the tertiary stage. They concluded that up to a maximum stress of approximately 100 MPa, the steady-state creep rate could be described by the equation,

$$\dot{\epsilon} = 10^{11} \text{ s}^{-1} \exp\left(-\frac{5.6\text{eV} - 2.7 \times 10^{-21} \text{ cm}^3 \sigma}{RT}\right) \quad (2.3.1)$$

where the value  $2.7 \times 10^{-21} \text{ cm}^3$  is the activation volume, 5.6eV is the height of the energy barrier and  $10^{11} \text{ s}^{-1}$  is  $\dot{\epsilon}$  at  $1/T=0$ . Figure 2.3.2 shows the creep equation plotted as log strain rate versus temperature for various values of stress.

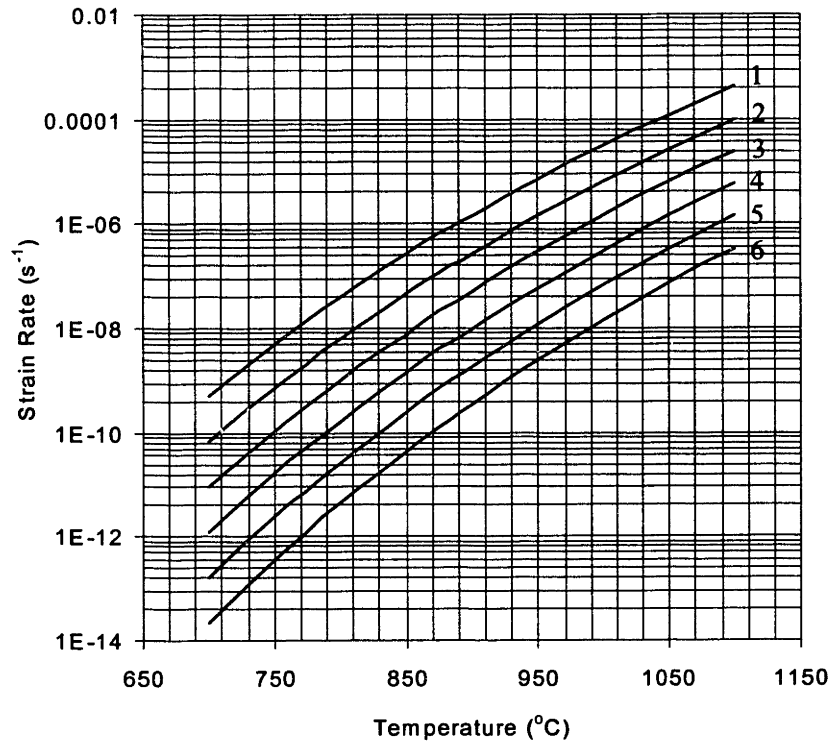


Figure 2.3.2: Myshlyaev et al. creep rate plotted versus temperature for stresses of 50 (1), 60 (2), 70 (3), 80 (4), 90 (5), and 100 MPa (6).

#### TAYLOR AND BARRETT:

Three years after Myshlyaev et al. completed their study, Taylor and Barrett<sup>13</sup> conducted their own experiments on the creep characterization of single-crystal silicon. One of the primary differences between the two studies is the crystal orientation. Myshlyaev et al. had oriented the crystals such that the load was applied along the  $\langle 111 \rangle$  direction. This orientation ensured the interaction of multiple slip systems. Taylor and Barrett wished to characterize the creep differences between single slip and multiple slip. To do this, they oriented their single-crystal specimens such that the  $(\bar{1}11), \langle 01\bar{1} \rangle$  slip system had the maximum shear stress for uniaxial compressive loading<sup>13</sup>.

Taylor and Barrett conducted their tests at temperatures above 0.6 times the absolute melting temperature of single-crystal silicon. They too saw creep behavior similar to that shown

in Figure 2.3.1. However their tests concentrated on the behavior after the decelerating Tertiary stage, as did Myshylaev et al. Based on their study, the creep in this region can be described by the equation,

$$y = \alpha \ln(vt + 1) \quad (2.3.2)$$

where, representative values for  $\alpha$  and  $\nu$  are  $10^{-3}$  and  $2.5 \text{ min}^{-1}$  respectively. In addition, Taylor and Barrett evaluated the activation energy of single-crystal silicon. They found the average apparent activation energy to be  $264 \pm 38 \text{ kJ/mol}$ .

## 2.4 BRITTLE MATERIAL CREEP TESTING

### 2.4.1 AVAILABLE TESTING METHODOLOGIES

#### DIRECT TENSION METHODS

"Direct tension" refers to the class of material tests that are performed by placing a specimen in pure tension. These tests are popular because the analysis of their results is straightforward. A specimen tested using a direct tension method will have a gage section with a simple and predictable stress state. Unfortunately, due to the brittle nature of silicon, traditional direct tension testing techniques are unlikely to be practical.

Many direct tension test setups involve friction gripping at both ends of a flat "dog bone" shaped specimen, as shown in Figure 2.4.1(a). The specimen has a larger cross-sectional area at the grip points to ensure that the maximum stress occurs at the midpoint in the gage section of the specimen. Unfortunately, friction gripping causes high shear stresses often resulting in premature fracture at the grip interface for brittle materials like silicon. This issue can be avoided by incorporating high grip-to-gage cross-sectional area ratios, but this creates additional difficulties. In particular, errors can result due to the increased probability of machining damage of the relatively large gage section surface area compared to the relatively small gage cross-sectional area<sup>14</sup>. To avoid these shortcomings, cylindrical "buttonhead" specimens have been developed, as shown in Figure 2.4.1(b). For these specimens, the load is transferred through a "buttonhead" instead of through frictional gripping. This technique can only be used for materials of moderate tensile strength because of the stress limitations at the "buttonhead" and

unfortunately, determination of this stress limit is extremely difficult. In addition, the cost of the grips and specimens are relatively expensive compared to traditional methods.

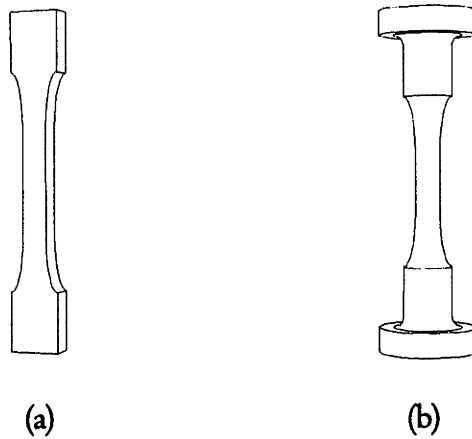


Figure 2.4.1: Specimen shapes for direct tensile testing. (a) "Dog bone" shape. (b) Cylindrical "buttonhead" shape.

## INDIRECT TENSION AND FLEXURAL METHODS

Several alternative methods of performing tension tests have been developed for use when direct tension can not be used or is impractical. One such method is the theta test<sup>14</sup>. For this test, a specimen is machined in a shape similar to the Greek letter theta ( $\theta$ ). The test piece is loaded on the top and bottom of the "theta" creating a uniaxial state of tension in the horizontal cross bar. Another example is the C-ring test<sup>14</sup>. This test involves loading a "C" shaped specimen at the top and bottom in either tension or compression. If testing is performed in tension, then tensile stresses are generated on the interior of the C at the axis of symmetry. Conversely, if testing is performed in compression, then tensile stresses are generated on the exterior of the C at the axis of symmetry.

The most common of the indirect tension testing methods are the 3-point and 4-point bend tests. For these methods, a rectangular beam is subjected to a known bending moment by the application of 3 or 4 point loads as shown in Figure 2.4.2. Although the test is simple and inexpensive to set up and run, it presents some difficulties for analysis and data reduction. In particular, the strain can not be measured as easily as it can using direct tension tests. Instead it must be estimated based on the measured deflection of the specimen and on beam-bending

theory. Also, since the test specimen is in bending, there is a stress gradient from the top of the specimen that is in compression, to the bottom that is in tension. This can create a problem for materials that behave differently in compression and tension. In addition, the presence of the maximum stress at the surface of the specimen can result in preferential failure from surface flaws<sup>14</sup>. Despite the analytical drawbacks, the 4-point bend test was found to be the most appropriate method for creep testing of silicon in support of the micro-engine program. This was largely due to the availability and affordability of single-crystal silicon wafers, which can be easily cut into rectangular specimens. The following section provides additional details regarding the use of 4-point bend tests to obtain creep data.

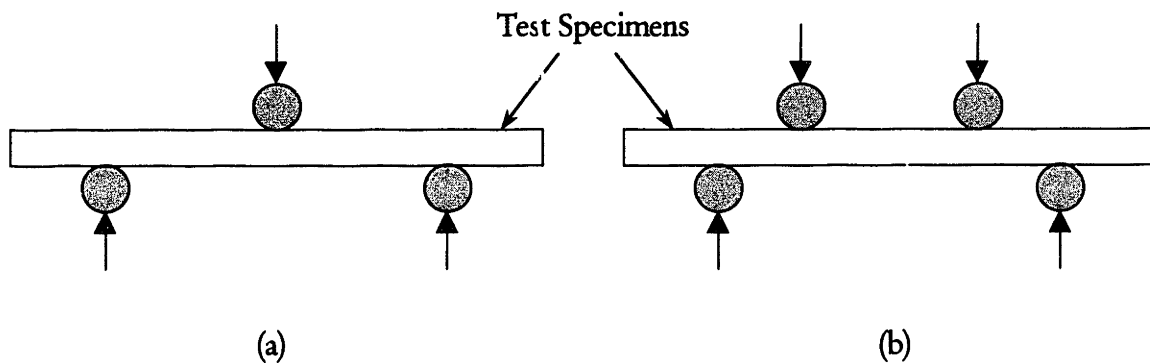


Figure 2.4.2: Flexural testing types. (a) 3-point bending. (b) 4-point bending.

#### 2.4.2 4-POINT BEND TEST TECHNIQUES - A LITERATURE REVIEW

The following paragraphs are a compilation from the literature, of techniques used to perform 4-point bend tests to determine creep characteristics. This summary will focus on those studies and papers that helped to define the methodology used in the micro-engine silicon creep tests. Before the methodology can be derived, some assumptions must be made. In particular, a mathematical model for the creep deformation, such as the ones presented in section 2.2, must be selected. For the purpose of this research, the power law model is chosen. There is no guarantee that the power law model will accurately represent the test data, but it is a good starting point and one that is supported by the work of Alexander and Haasen<sup>11</sup>.

Although 4-point bend tests are easy to perform, they are usually not accompanied by a

simple data analysis. In particular, it is often difficult to accurately determine the strains within the test beam. A 4-point bend test works by generating a constant moment across the gage section of the specimen. The shear-moment diagram for this setup is shown in Figure 2.4.3. Assuming ideal beam-bending theory applies, a constant moment will yield a constant curvature between the inner loading points. Therefore a test setup which measures the specimen center point deflection relative to the deflection of the two inner load points can fully characterize the beam curvature. From this starting point, Hollenberg et al.<sup>15</sup> derived an expression for the maximum strain,

$$\epsilon_{\max} = \frac{4h}{a^2}(y_C - y_L) \quad (2.4.1)$$

where  $h$  is the specimen thickness,  $a$  is the distance between the inner load points,  $y_C$  is the deflection at the center of the specimen and  $y_L$  is the deflection at the load points. To make the experimentation easier, Hollenberg et al. also derived equations assuming that only load point deflection measurements were available. Making certain geometric assumptions, it was concluded that for small deflections the maximum strain is,

$$\epsilon_{\max} = \frac{2hy_L}{a[L - a]} \quad (2.4.2)$$

where  $L$  is the distance between the outer load points.



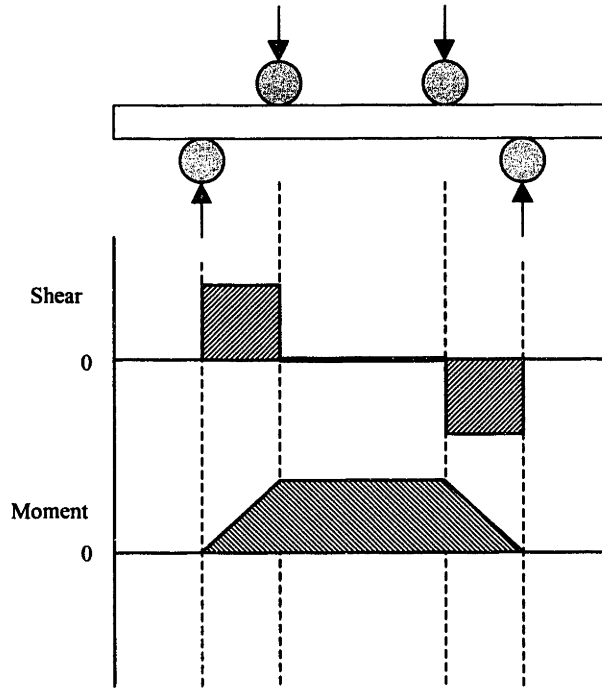


Figure 2.4.3: Shear-Moment diagram for a 4-point bend test.

Assuming that creep rate is proportional to stress raised to the "nth" power, as is consistent with the power law theory, Hollenberg et al. set out to relate the maximum stress and strain to the creep exponent "n". Using the method of creep compliance, they developed the equations,

$$\sigma_{\max} = \frac{3(L - a)P}{bh^2} \frac{(2n + 1)}{3n} \quad (2.4.3)$$

$$\epsilon_{\max} = \frac{2h(n + 2)}{(L - a)[L + a(n + 1)]} y_L \quad (2.4.4)$$

where  $2P$  is the applied load. Note that only the deflection at the inner load points is required for these calculations. However, the test setup for the micro-engine silicon creep testing only has center point deflection measurement capability. Sato et al.<sup>16</sup> had this configuration as well and developed a revised expression for the maximum strain, which only requires a center point measurement. The new expression is,

$$\epsilon_{\max} = -y_c \frac{4h(n + 2)}{2L^2 + an(2L - a)} \quad (2.4.5)$$

The testing method proposed by Hollenberg et al. is seen often in the literature including in the works of, Sato et al., Wilshire and Jiang<sup>17</sup>, Jakus and Wiederhorn<sup>18</sup>, Talty and Dirks<sup>19</sup>, Jou et al.<sup>20</sup> and Chuang<sup>21</sup>. Each of these studies incorporated a common approach to deriving the power law constants "n" and "Q" (refer back to the power law relationship in equation 2.2.4. The tests followed this general procedure:

1. At a specific temperature, a series of tests are run at different stress points within the desired stress range. Then, another temperature point is tested at the identical stress values. This continues until the desired temperature range has been tested.
2. From Hollenberg et al., it is known that the deflection is a function of the applied force raised to the "nth" power where n is the creep exponent. Therefore, a plot of  $\log(y_c)$  versus  $\log(2P)$  at each temperature point will have a slope of n. (Note: if the stress is known, n will also be the slope from the plot of  $\log(\dot{\epsilon})$  versus  $\log(\sigma)$ .)
3. Additionally, a plot of  $\log(\dot{\epsilon})$  versus  $1/T$ , for each stress, will have the slope of  $-(Q/R)$ . Since R is known, Q can be directly calculated.
4. Finally, if accurate values of stress are known at each test point, then for a given test condition the proportionality constant "A" can be found. Unfortunately, accurate stress data is usually not readily available, therefore the test data must be correlated to an analytical model to back out a value for the constant A.

Creep characterization using the above methodology is well documented in the literature. In addition, the errors involved in 4-point bend testing have been meticulously analyzed. Refer to Baratta's<sup>22</sup> paper on flexural testing for a thorough examination of the potential sources of error in 4-point bend testing.

## CHAPTER 3 CREEP TEST SETUP AND METHODOLOGY

### 3.1 TEST EQUIPMENT

The silicon creep tests performed for the micro-engine project were conducted in the MIT Technology Laboratory for Advanced Composites (TELAC). A testing system was assembled in the lab to simulate the high temperature environment of the micro-engine. The test equipment can be broken down into four sub-systems: the heating unit, the loading apparatus, the sensing mechanisms and the data acquisition equipment.

#### 3.1.1 THE LOADING APPARATUS

The load is applied to the specimen using an MTS 810 material testing system fitted with a 4-point bend fixture and controlled by an INSTRON™ 8500 electronic controller. The pushrods that transmit the load to the 4-point bend fixture are constructed of alumina and the 4-point bend fixture is made of silicon carbide. These materials are necessary due to the high temperatures associated with creep testing.

Figure 3.1.1, Figure 3.1.2 and Figure 3.1.3 show the MTS 810, the 4-point bend fixture and the electronic controller respectively. The 4-point bend fixture is composed of a system of unrestrained cylindrical rollers and semicircular supports to ensure that the load is applied evenly and to reduce errors due to load-point friction. The upper and lower rollers are spaced 20 and 40 mm apart respectively. Details of the loading apparatus are included in APPENDIX A.2.

#### 3.1.2 THE HEATING UNIT

The silicon specimens are brought up to test temperatures using a split insulated furnace that is attached to the MTS 810 material testing system and completely surrounds the test specimens. The furnace has a maximum operating temperature of 1500°C and is driven by a fully automated electronic controller. Heat within the furnace is generated through a series of molybdenum disilicide ( $\text{MoSi}_2$ ) heating elements and the temperature is monitored with an array of three thermocouples (see APPENDIX A.3 for specification details).

Figure 3.1.1 and Figure 3.1.4 show photographs of the entire TELAC heating system.

### *3.1.3 THE SENSING MECHANISMS*

To properly execute the creep test, accurate measurements of applied load and specimen deflection are necessary. The load is measured through a 10 kN INSTRON™ load cell, and the deflection is measured at the specimen centerpoint with an INSTRON™ LVDT. The LVDT has a maximum range of 2 mm and has a 1  $\mu$ m sensitivity.

Figure 3.1.1 and Figure 3.1.2 show the sensing mechanisms, and their specifications can be found in APPENDIX A.3.

### *3.1.4 THE DATA ACQUISITION EQUIPMENT*

Analog data is collected via the INSTRON™ 8500 controller (shown in Figure 3.1.3) and then output through an A/D converter to a Macintosh Power PC. The personal computer is equipped with LabView™ for the purpose of data collection. Kuo-Shen Chen, of the MIT Gas Turbine Lab, created the LabView™ interface that was used in this testing. The program allows for real-time viewing of the output data and can be used to control the data collection frequency. A picture of the LabView™ interface control screen is shown in Figure 3.1.5. Details of the LabView™ program used are included in APPENDIX A.5.

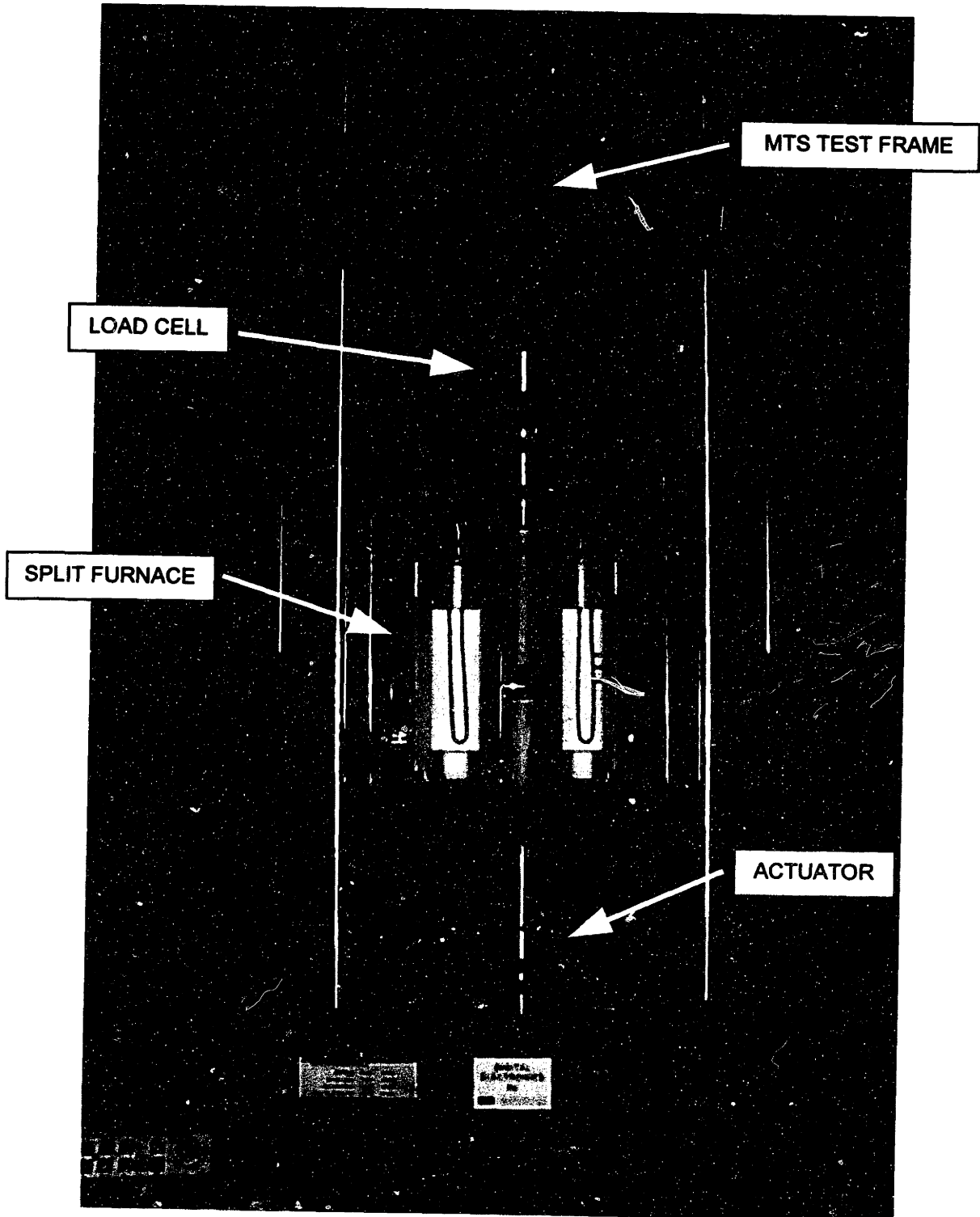


Figure 3.1.1: MTS 810 material testing system with split cylindrical furnace.

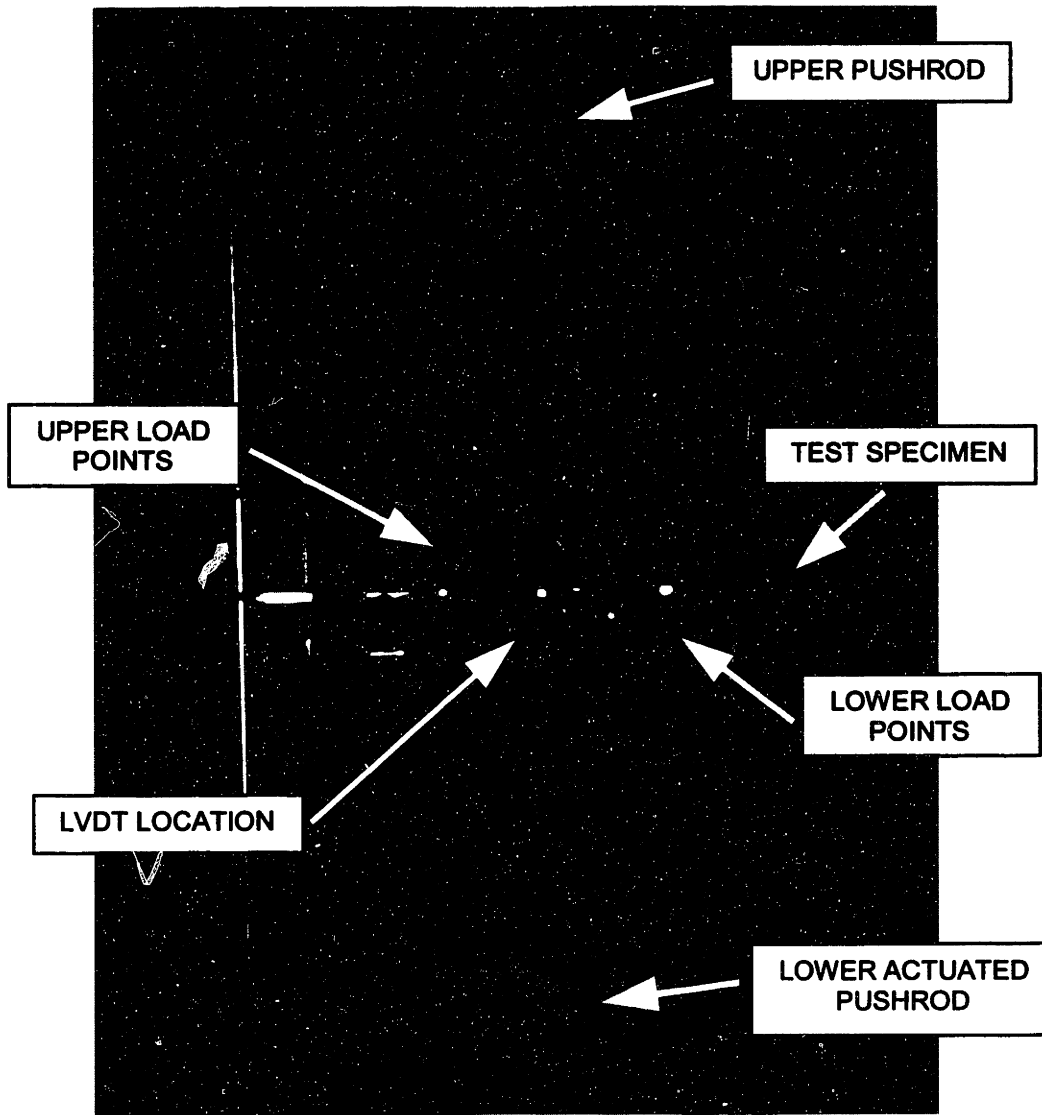


Figure 3.1.2: Silicon Carbide 4-Point bend fixture.



Figure 3.1.3: INSTRON™ 8500 electronic controller.



Figure 3.1.4: Furnace temperature controller.

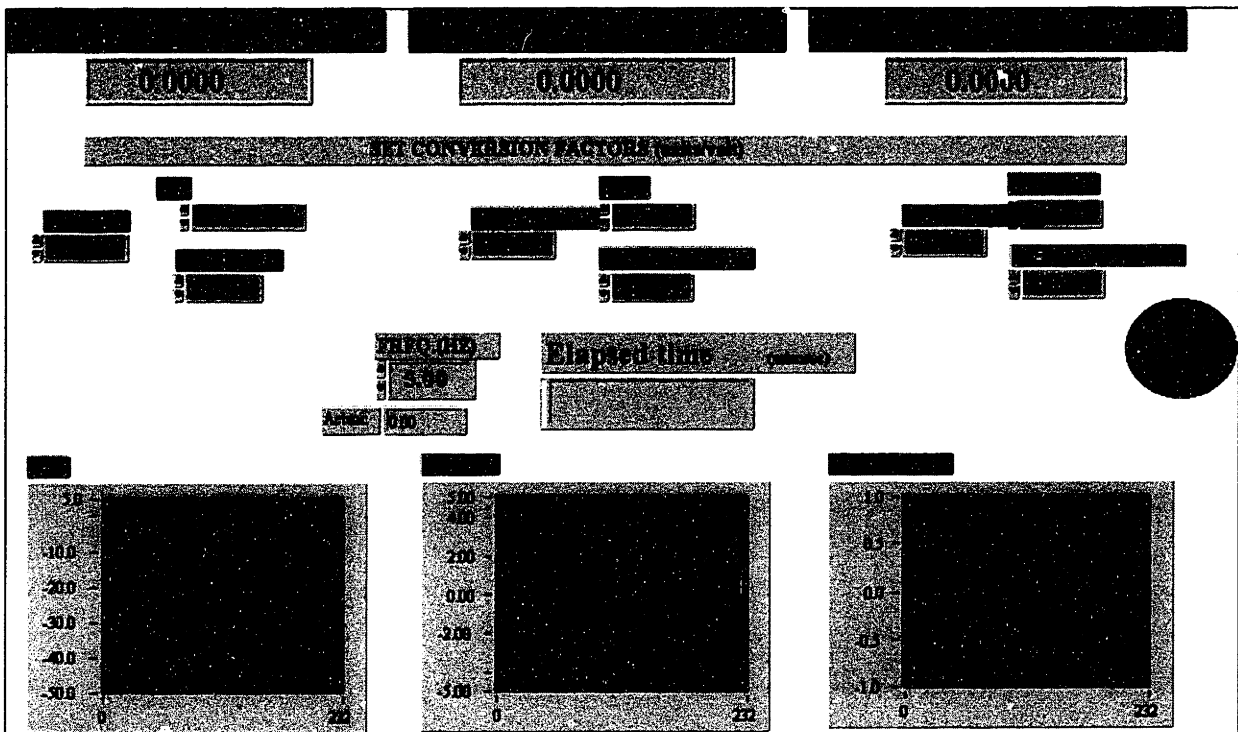


Figure 3.1.5: Labview™ interface screen.



## 3.2 TEST PROCEDURE

The following paragraphs give a general description of the procedure used for testing the creep properties of silicon. A formal list of instructions was created to ensure that a consistent methodology was used. These instructions are included in APPENDIX A.6.

### 3.2.1 SPECIMEN PREPARATION AND SETUP

Prior to testing, the silicon specimens are cut, using a diesaw, from a 1 mm (100) n-type single-crystal silicon wafer. The specimens were cut with the  $\langle 110 \rangle$  directions as the long axis of the beam. This crystal orientation was chosen because it offers the highest yield strength<sup>23</sup>. Each specimen measures at least 45 mm in length, with a width of 9mm as shown in Figure 3.2.1. The sharp edges of the specimens are polished progressively, using 600 to 1200 grit SiC paper, to ensure that premature failure does not occur due to brittle fracture from edge flaws. Finally, the silicon is cleaned with methanol to remove all contaminants.

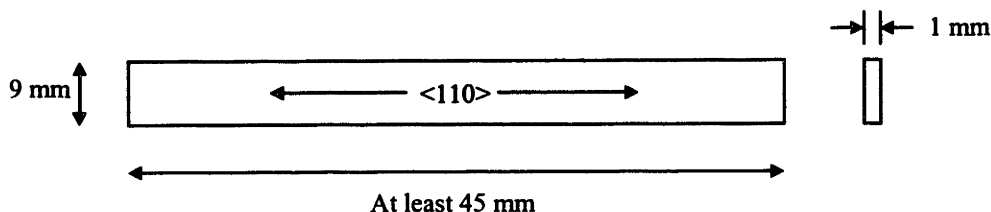


Figure 3.2.1: Silicon test specimen dimensions.

The specimen is loaded into the 4-point bend fixture, ensuring that it is aligned axially and that the top rollers are properly centered between the bottom rollers. Using the hydraulic actuators of the 810 MTS system, the fixture and specimen are raised until they almost contact the upper pushrod. This is the initial position for the specimen during the test, so at this point the furnace can be closed and locked. With the temperature controller set to the desired temperature, the controller program is executed to begin heating the specimen at a rate no greater than 12°C/minute.

### 3.2.2 LOADING CONDITIONS

Once the specimen has soaked at the test temperature for 15 minutes (to ensure thermal

equilibrium), the loading portion of the test begins. The MTS 810 actuator is used to lift the specimen and 4-point bend fixture until it just barely contacts the upper push rod. This point is signified by a shift in the load cell output from approximately zero to a negative (compressive) force value. The INSTRON™ 8500 is now programmed to increase the load by 1 N/s until the appropriate test load is reached. The load is maintained at a constant level until the test is complete, at which point the actuator is manually moved to unload the specimen. The end of the test is the point at which the LVDT exceeds its maximum range or when it is determined that the specimen has ceased to creep.

### *3.2.3 DATA COLLECTION AND STORAGE*

Data collection commences just prior to load application. The "RUN" button is selected on the LabView™ interface to begin this process. The data collection rate is also controlled via the interface and can be altered throughout the test as necessary typical rates. Upon completion of the test, the "RECORD" button is selected in LabView™. This button allows the collected data to be written to a specified file. The data is written in a columnar format to permit easy translation into a spreadsheet for further data reduction.

A flowchart of the entire test procedure is shown in Figure 3.2.2.

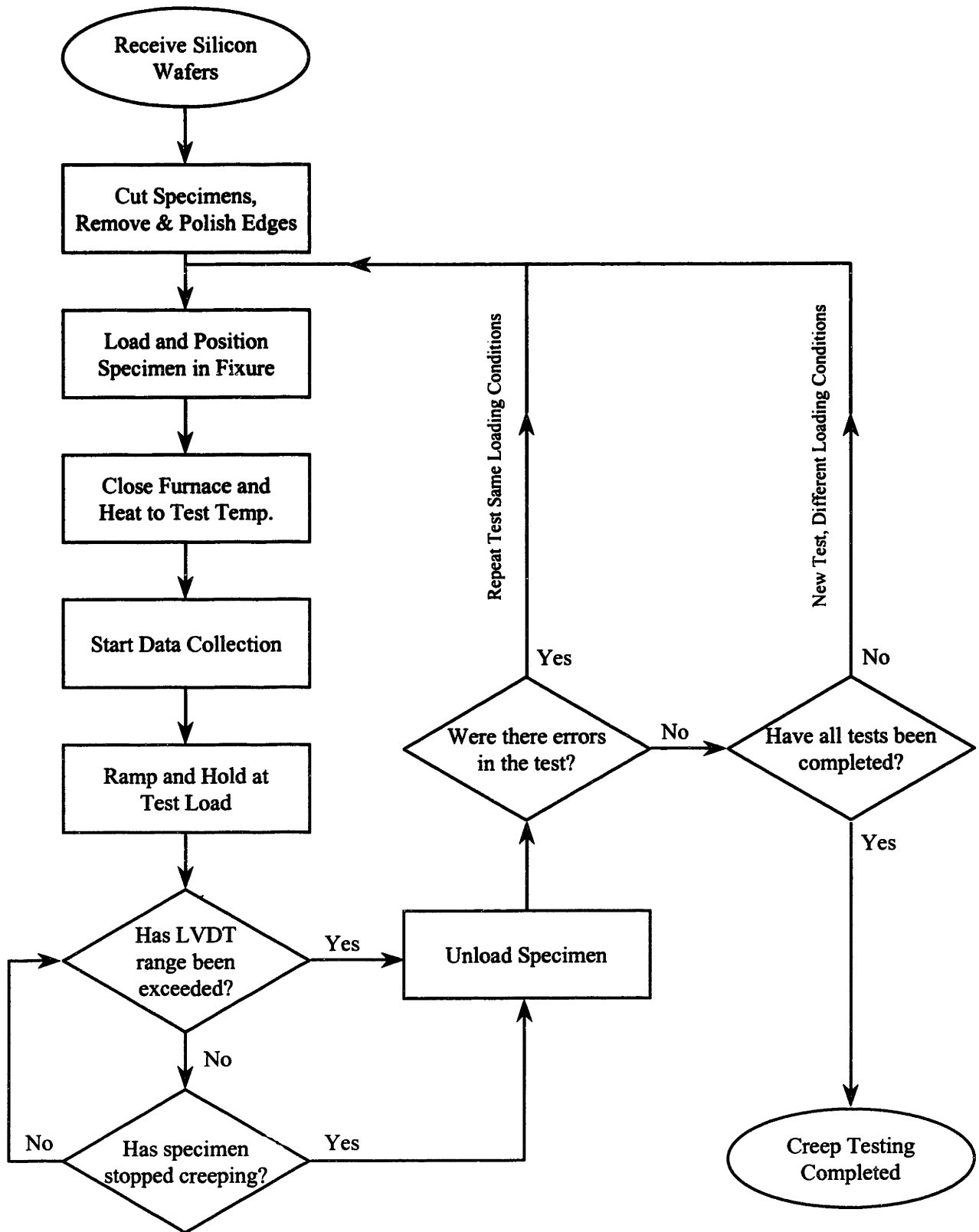


Figure 3.2.2: Test Procedure Flowchart.

### 3.2.4 METALLOGRAPHY

To fully understand the nature of the creep within a specimen, it is necessary to study the microstructure of the tested silicon. To view features such as dislocation pile-ups and slip bands, the following procedure is used:

- First, the specimen is mounted in a slow-setting epoxy that is allowed to cure overnight.
- Next, the specimen is cut to the desired size using a high speed diamond saw lubricated with water and soluble oil.
- The cut section is then mounted in a quick-setting epoxy with the feature of interest facing out.
- The specimen is then polished to expose the surface of interest using the following sequence on a rotary machine at a force of 30N,

Silicon Carbide paper at 300RPM,

240 grit for 2 minutes  
320 grit for 2 minutes  
400 grit for 2 minutes  
600 grit for 2 minutes  
1200 grit for 2 minutes

Diamond grit at 150 RPM,

6  $\mu\text{in}$  for 3 minutes  
3  $\mu\text{in}$  for 3 minutes  
1  $\mu\text{in}$  for 3 minutes

Alumina grit at 150 RPM,

.5  $\mu\text{in}$  for 1 minute

- Finally, the surface is chemically etched for 60 seconds with a solution of 97% HNO<sub>3</sub> and 3% HF (55% conc.).

## CHAPTER 4 RESULTS

### 4.1 CREEP TEST DATA

The scope of the MIT creep testing was defined by the needs of the micro-engine project. To fully characterize the creep of silicon for this project, creep curves are needed for the temperature range of 600-850°C and a stress range of 30-200 MPa. Based on these ranges and the known yield strength of silicon a testing matrix was created as shown in Figure 4.1.1. The darkened blocks indicate the specific test points of the experiment.

		Stress Level (MPa)					
		30	50	80	100	150	200
Temperature °C	600						
	650						
	700						
	750						
	800						
	850						

Figure 4.1.1: Silicon creep test matrix.

Unfortunately though, the exact test specimen stress can not be calculated because it is a function of the creep exponent, as seen in equation 2.2.2. Therefore the required constant load to generate the desired stress is not known. To determine the test loads,  $n$  in equation 2.4.3 is assumed to be 1.0 (no creep). The input forces and their corresponding stress levels are shown in Table 4.1.1.

Load Level (N)	Stress Level (MPa)
9	30
15	50
24	80
30	100
45	150
60	200

Table 4.1.1: Assumed load-to-stress equivalents.

The creep tests are set up to output a continuous flow of three parameters; time, load and specimen center point deflection. As described above, the creep tests are run at a constant load, therefore once the load is set, only displacement changes over time. The relationship between displacement and time is the heart of the creep characterization tests. An actual displacement versus time plot from the creep testing, at a temperature of 750°C and a constant load of 30 N, is shown in Figure 4.1.2. There are several distinct features common to all of the curves from this testing. Recall from the test procedure that the fixture and specimen are raised until the fixture just comes into contact with the pushrod. This first contact occurs at point "A" Figure 4.1.2. The actuators are then programmed to raise the fixture further until the desired load is obtained. This is the first constant rate displacement and is marked with a "B" in the figure. During, what is termed here, the "stage one" portion of the creep test, the material creeps at an increasing rate. This is consistent with the stage one creep described by Alexander and Haasen, and Myshlyaev et al. Also consistent with these papers is the constant rate "stage two". This is the creep regime to which Alexander and Haasen concentrated on and will be the focus of the present study as well. Notice that the stage two creep ends abruptly near a displacement of 2 mm. This is the point at which the 4-point bend fixture reaches its displacement limit and "bottoms out". The fixture and specimen thickness limitations prohibit us from testing into the "stage 3" region which was tested extensively by Myshlyaev et al.

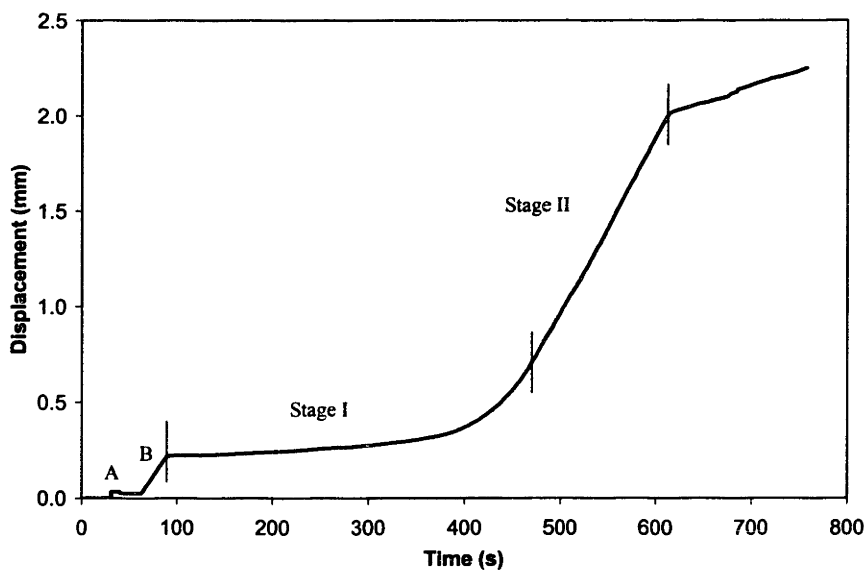


Figure 4.1.2: Raw test data at 750°C and 30 N.

The displacement versus time curves for each test point can be found in APPENDIX A.7. The actual output displacement data for this test setup is recorded as negative, therefore the curve shapes in the appendix are inverted from that shown above.

In addition to the tests performed according to the matrix in Figure 4.1.1, a separate series of tests were conducted at a temperature of 700°C and 45 N. There are a total of four tests completed at these conditions. In each case the test is terminated at a different incremental time point. The purpose of these tests is to document the overall creep deformation history throughout an entire test as opposed to the center point displacement obtained by the LVDT. The four chosen time points are shown on the original displacement-time graph (from APPENDIX A.6) in Figure 4.1.3. The points are selected to represent each stage of the creep curve. Point 1 is at the end of the incubation portion of stage I; point 2 is in the middle of the stage I acceleration; point 3 is at the steady-state stage II initiation; and point 4 is at the end of stage II.

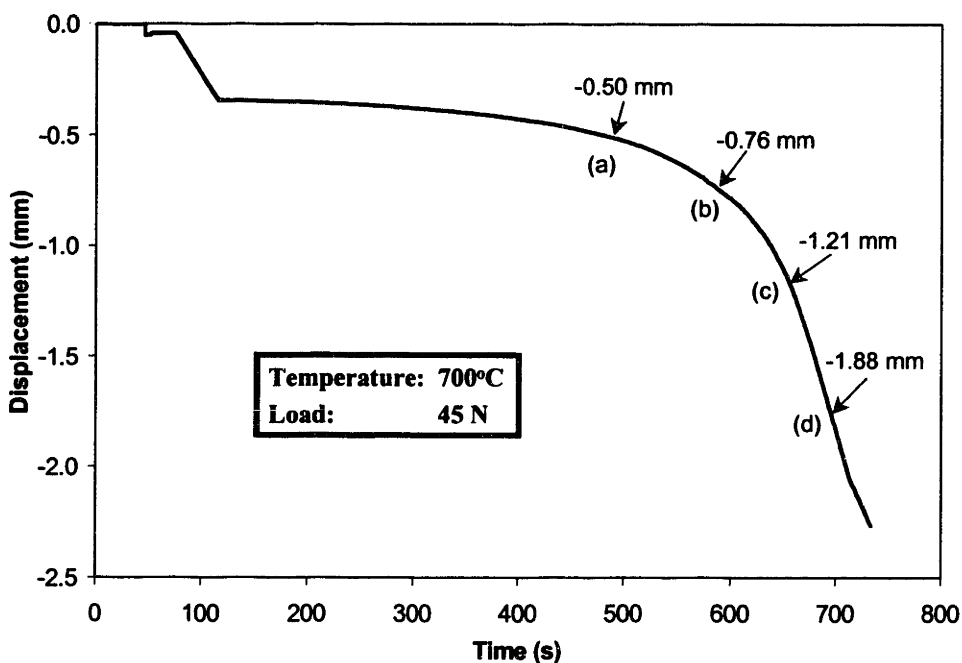


Figure 4.1.3: Location of incremental test points at 700°C and 45 N.

The displacement versus time output from each of the four tests is overlaid in Figure 4.1.4 and individually included in APPENDIX A.8. Photographs of each of the four test specimens are shown in Figure 4.1.5. A profilometer was used to measure the contours of each of the specimens as well. A plot of these measurements is shown in Figure 4.1.6.

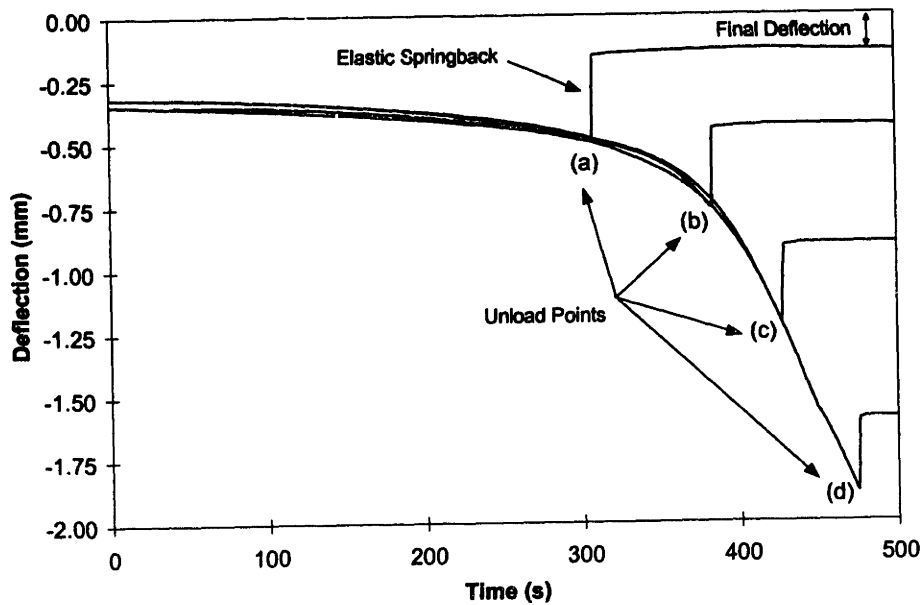


Figure 4.1.4: Incremental test at 700°C and 45N, displacement versus time plots. Centerpoint deflections prior to unload are (a) -0.50 mm, (b) -0.76 mm, (c) -1.21 mm, and (d) 1.88 mm.



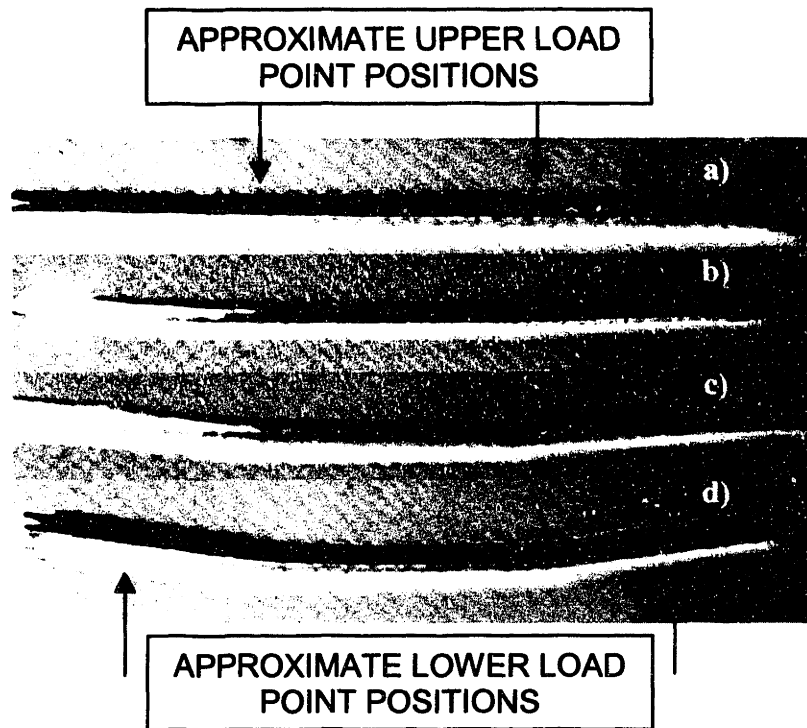


Figure 4.1.5: Silicon incremental test specimens sideviews. Centerpoint deflections prior to unload are (a) -0.50 mm, (b) -0.76 mm, (c) -1.21 mm, and (d) 1.88 mm.

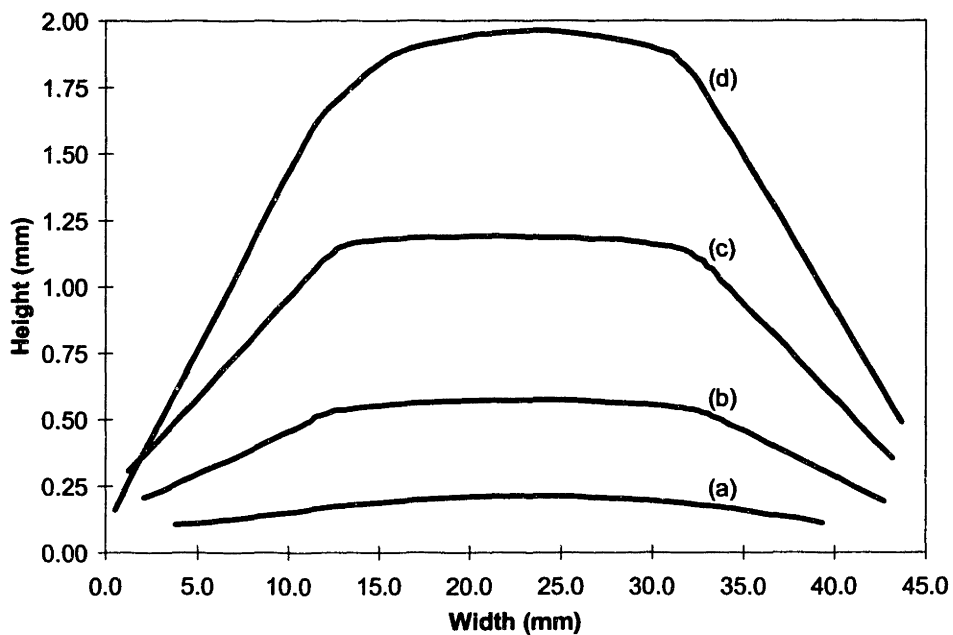


Figure 4.1.6: Profilometer traces of deformed shapes of specimens shown in Figure 4.1.5. Centerpoint deflections prior to unload are (a) -0.50 mm, (b) -0.76 mm, (c) -1.21 mm, and (d) 1.88 mm.

## 4.2 DATA REDUCTION

Reducing the raw data from the silicon creep tests proved to be a less than straightforward task. The following sections walk through the procedures used to attempt to convert the test data into useful constitutive relationships. The approaches are presented in the chronological order in which they were applied.

### 4.2.1 HOLLENBERG ET AL. POWER LAW APPROACH

Based on the successful use of the power law relationship by Alexander and Haasen, the first attempt to reduce the data centers on solving the power law equation using the Hollenberg et al. relationships. At the end of each test the output (centerpoint displacement, time and load) is imported into a spreadsheet for data reduction. The specific data reduction process is as follows:

1. The goal of this analysis is to solve for the power law creep equation unknowns, A, n and Q as seen in equation 2.2.4. As mentioned in section 2.4.2, the first step is to derive the creep exponent n from the relationship between centerpoint displacement rate and the applied force. Based on the work of Hollenberg et al, Sato et al.<sup>16</sup> found that in the steady-state regime, where the strain rate is proportional to stress, the centerpoint displacement rate is also proportional to stress. Therefore we can write,

$$\dot{\epsilon} \propto \sigma^n \quad (4.2.1)$$

Also from Sato et al., strain rate is proportional to deflection rate and stress is proportional to the applied load. It therefore follows that,

$$\dot{y} \propto (2P)^n \quad (4.2.2)$$

Therefore if the logarithm is taken on each side of this equation then the following relation results,

$$\log(\dot{y}) = n \cdot \log(2P) + C \quad (4.2.3)$$

where  $\dot{y}$  is the centerpoint displacement and 2P is the applied load. Displacement rate is calculated by taking differential intervals ( $\Delta y/\Delta t$ ) throughout the data set. The rate is then

plotted versus time so that the steady-state rate can be determined graphically. A plot of displacement rate versus time for the test point 750°C and 30N is shown for reference in Figure 4.2.1. The entire set of displacement rate versus time plots is included in APPENDIX A.9.

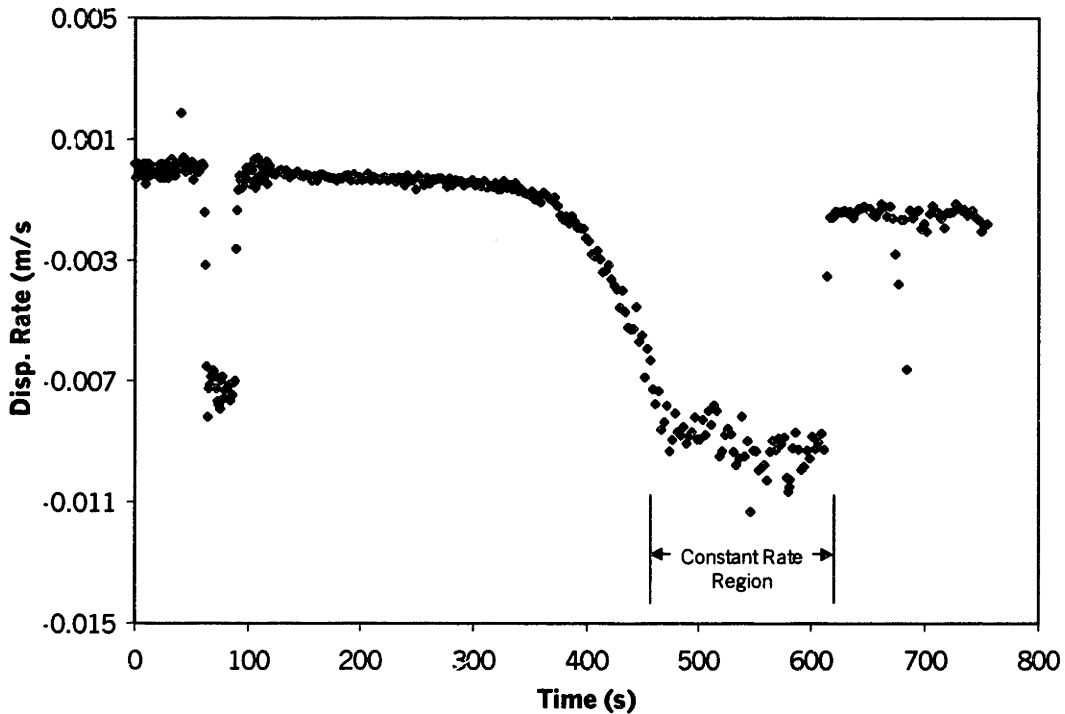


Figure 4.2.1: Displacement rate versus time plot at 750°C and 30N.

Next, the logarithm of the displacement rate is plotted versus the log of the applied force for each testing temperature. The resulting slope of the lines is the creep exponent  $n$ . Figure 4.2.2 is the plot generated for the silicon creep tests. A best-fit linear line is included for the test points at each temperature. The equation defining each best-fit line is shown adjacent to the corresponding line. The slopes vary from just under 3 to almost 5. Since the creep exponent can only be considered constant over small ranges of stress and temperature, it is not surprising to see this variation. A closer examination of the data reveals that the extreme low stress points appear to skew the data in their associated temperature towards higher values of  $n$ . Upon removal of the extreme test points, it appears that a creep exponent near 3 is appropriate over a large portion of the temperature and stress range that was studied.

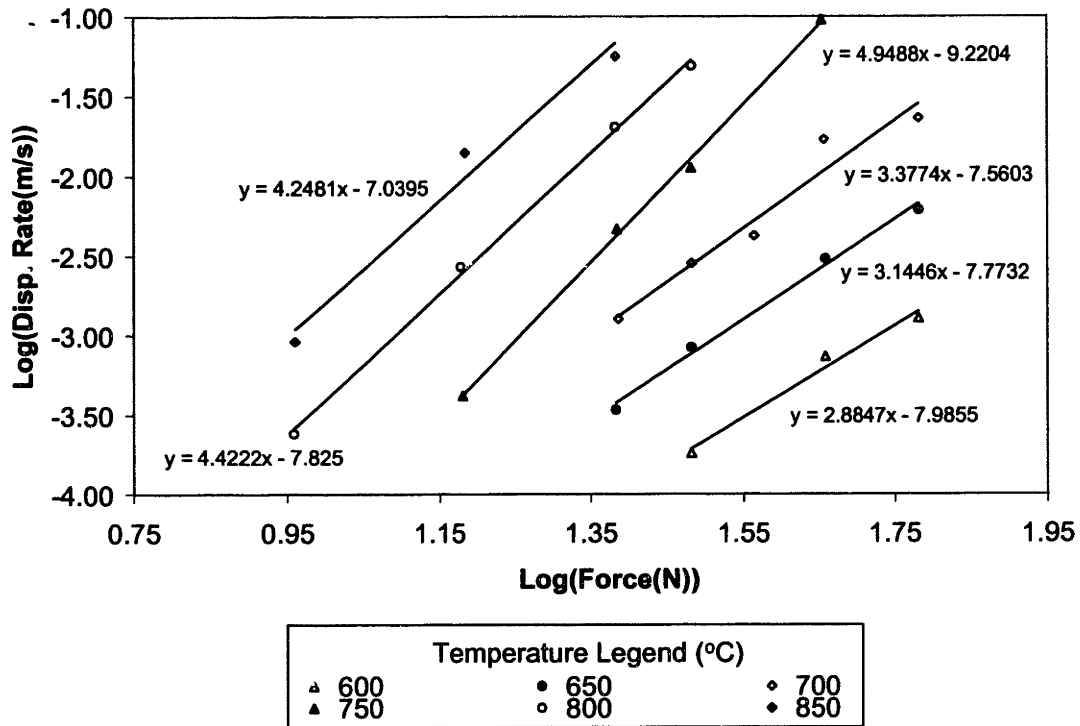


Figure 4.2.2: Plot to determine the creep exponent  $n$ .

2. The next step is to determine the value of  $Q/R$ . The approach again is graphical. First the strain rate of the steady-state portion of the test must be calculated from the raw data. Using equation 2.4.5 the strain is calculate for each raw data point. The strain rate is found in the same manner as the displacement rate, by calculating it at differential intervals ( $\Delta \dot{\epsilon} / \Delta t$ ) throughout the data set. From the plot of the strain rate versus time, shown in Figure 4.2.3, the steady-state strain rate can be determined. For this particular plot, the strain rate is approximately  $2.75 \times 10^{-15} \text{ s}^{-1}$ . The entire set of strain rate versus time plots is included in APPENDIX A.10.

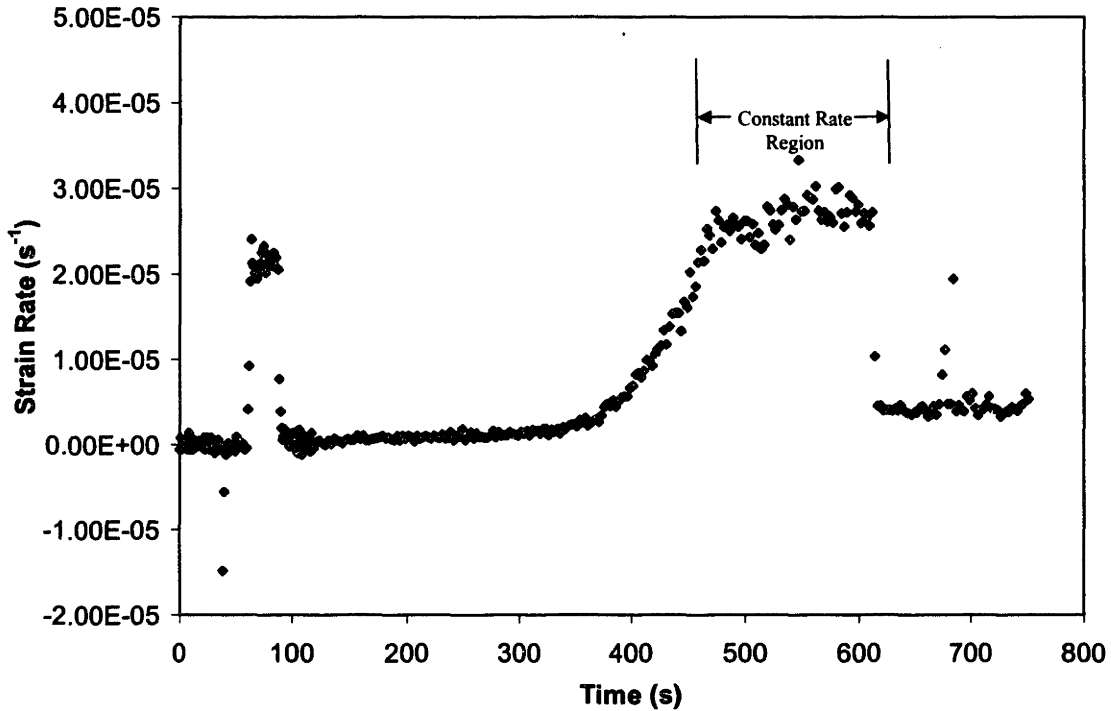


Figure 4.2.3: Strain Rate versus Time Plot at 750°C and 30N.

Now that strain rate is known, recall that the power law relationship,

$$\dot{\epsilon} = A\sigma^n \exp\left(-\frac{Q}{RT}\right) \quad (2.2.4)$$

If the natural logarithm of both sides is taken then the resulting relationship is,

$$\ln(\dot{\epsilon}) = -\frac{Q}{R} \cdot \frac{1}{T} + n \cdot \ln(\sigma) + \ln(A) \quad (4.2.4)$$

Therefore, for a given value of stress, a plot of  $\ln(\dot{\epsilon})$  versus  $1/T$ , where  $T$  is in degrees Kelvin, will have a slope of  $-Q/R$ . This plot, for the data collected during the silicon creep tests, is shown in Figure 4.2.4. The slope values of  $Q/R$  range from 23,300 to 40,400 K, but as was observed for the creep exponent  $n$ , over the majority of the stress range, the values for  $Q/R$  vary only slightly and can be approximated to be 25,000 K. Since,  $R$  is equal to 8.314 J/K·mol,  $Q$  can

be calculated to be 208 kJ/mol. This compares favorably to the Q of 232 kJ/mol and the  $264 \pm 38$  kJ/mol found by Alexander and Haasen<sup>11</sup>, and Taylor and Barrett<sup>13</sup> respectively. As previously noted, Q is often found to have a weak temperature dependence. The high-end temperatures tested for this thesis are at the lower end of the temperature ranges tested by Alexander and Haasen, and Taylor and Barrett. Therefore, a better comparison may be to calculate the Q at the high temperature end of the 24 N constant force line. The resulting Q is 224 kJ/mol, which agrees more closely with the results of Alexander and Haasen, and Taylor and Barrett.

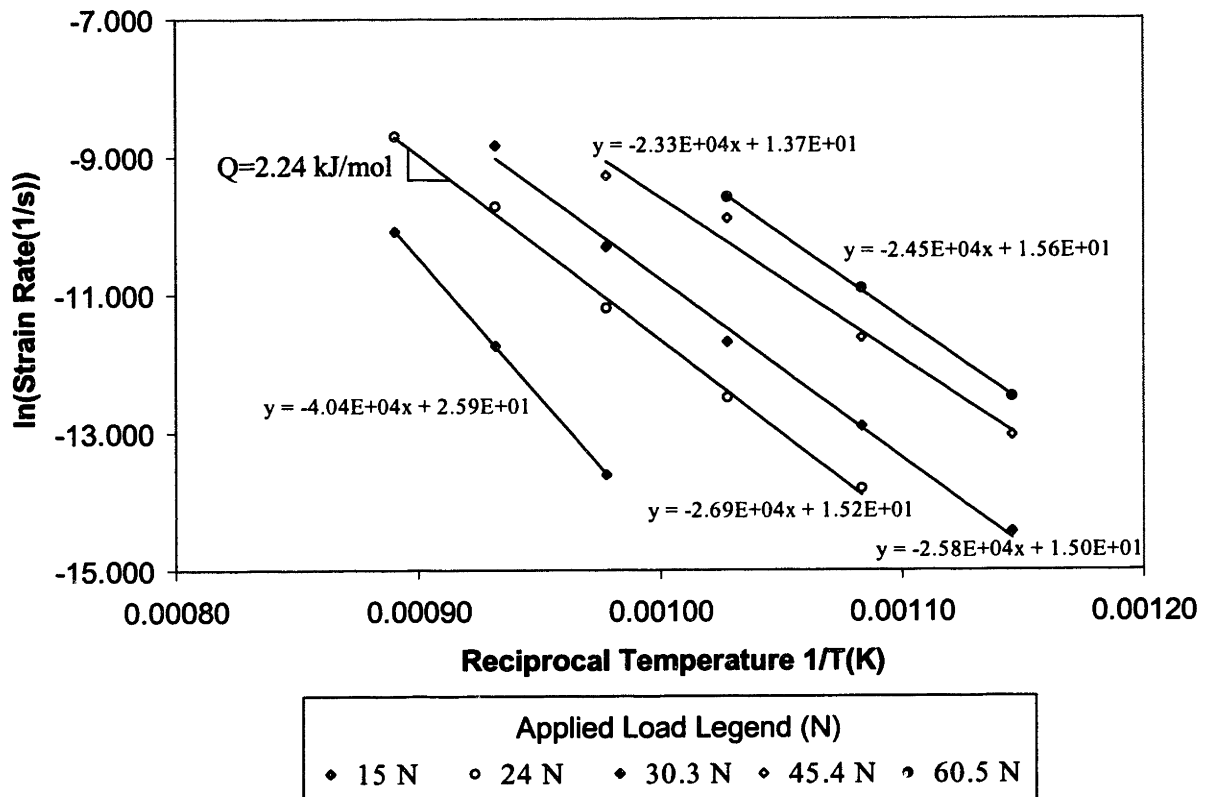


Figure 4.2.4: Plot to determine the creep ratio Q/R.

3. The final step in the process is to back-calculate the proportionality constant A. Knowing the strain rate, stress, temperature, creep exponent and Q/R, the proportionality constant can be calculated directly from equation 2.2.4. Unfortunately, the actual stress is not known. It

therefore needs to be estimated by using an approximate method such as beam-bending theory. If this method is incorporated, such that the stress is equal to that described in equation 2.4.3, then, based on the silicon test data, the proportionality constant is  $3.4 \times 10^{-18}$ , when stress is given in Pa. Based on these preliminary results, the stage II creep behavior over the majority of the test conditions can be described by the power law relationship,

$$\dot{\epsilon} = (3.4 \cdot 10^{-18}) \sigma^3 \exp\left(-\frac{25000}{T}\right) \quad (4.2.5)$$

where T is in degrees K and  $\sigma$  is in Pa.

#### 4.2.2 FINITE ELEMENT ANALYSIS CORRELATION

To determine a more accurate value for the proportionality constant A, a finite element model is developed using ANSYS<sup>TM</sup> 5.4a. Using the model, more realistic stress values can be determined to calculate A. To reduce analysis time, a symmetry boundary is used to allow modeling of only half of the test setup. The structure of the specimen and 4-point bend rollers are generated from 2D PLANE42 elements, with thickness added. Contact between the test fixture and the specimen is simulated with contact elements at the upper roller and with a coupled node on the lower roller. Modeling details are included in APPENDIX A.11. A plot of the elements is shown in Figure 4.2.5.

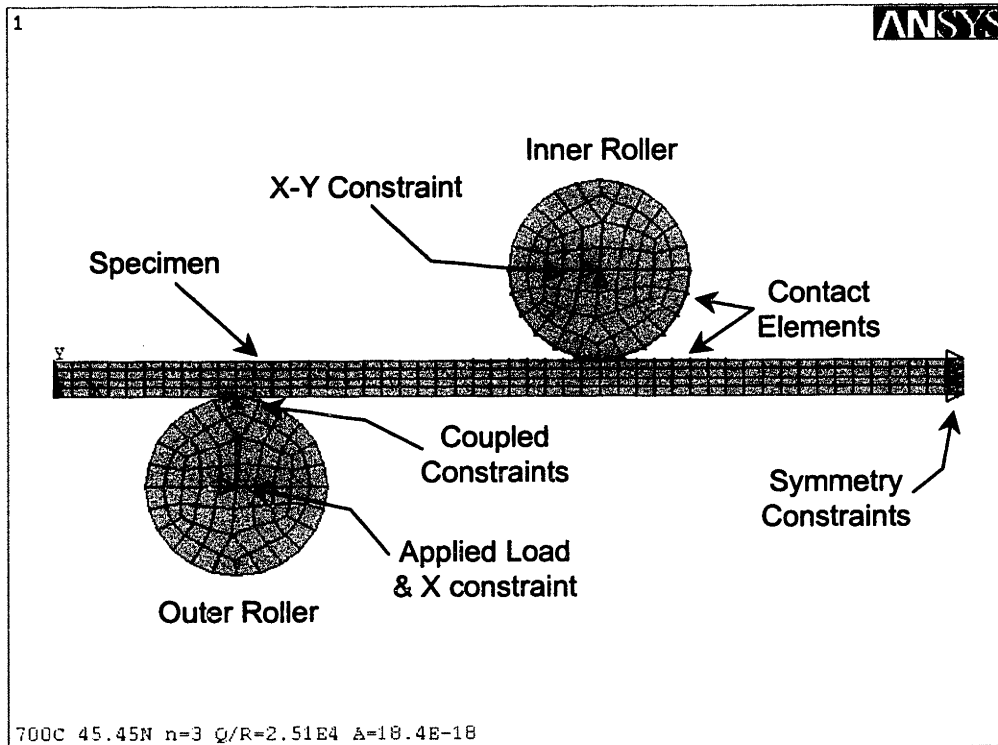


Figure 4.2.5: Fintite element model.

To determine the proportionality constant, the model is run using the logic described below.

1. For a given temperature and stress combination a "guess" for the power law proportionality constant is chosen and input to the model.
2. The model is run in batch mode. A sample batch file is shown in APPENDIX A.12.
3. The creep rate of the model is compared to the steady-state creep rate from the silicon tests.
  - If the creep rates match, then the proportionality constant is recorded and a new temperature and stress combination is run.
  - If the creep rates do not match, then the proportionality constant is adjusted and the process repeats.

The finite element analysis yielded an average proportionality constant of  $A = 1.6E-18 \text{ m}^6/\text{N}^3\text{s}$ .



### 4.2.3 FINITE ELEMENT ANALYSIS REALITY CHECK

To check the model for accuracy, the results are compared to the interval test that was performed at 700°C (described in section 4.1). If the model is accurately describing the behavior of the silicon, then the radius of curvature in the constant moment portion of the specimen should be equal to that of each test specimen from the interval test. The first step is to measure the profile of the test specimens. This was done using a Mitutoyo Contracer™ CR-41 profile tracer. Next, the model had to be run at the same points as in the interval test. But, since the specimen profiles are measured after unload and cool down, the ANSYS™ model must be altered to include an unloading and cool down step, previously not required. The results of each of the 4 specimen measurements, corresponding to the 4 points described in Figure 4.1.3, along with one profile from the ANSYS™ model are shown in Figure 4.2.6.

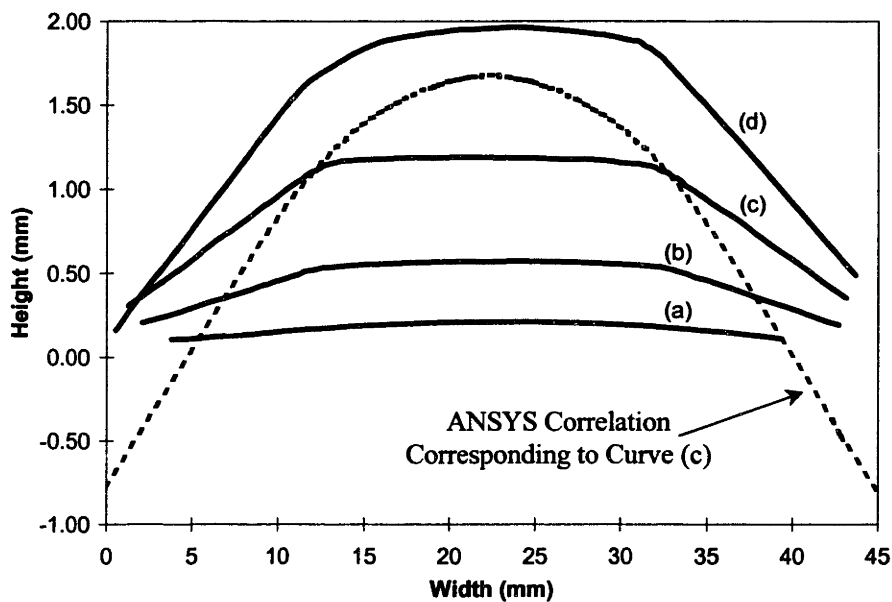


Figure 4.2.6: 700°C interval test specimen profiles.

There is poor correlation between the profiles of the interrupted test and the output from the ANSYS™ model. It appears that there is localized plastic deformation on the test specimens in the area of the inner loading points. For this reason, the results from the ANSYS™ analysis are not representative of the material behavior. In addition, it is likely that the previously derived values for  $A$ ,  $n$  and  $Q/R$  in the power law creep equation are not representative of general

silicon creep, but instead are a combined effect of creep and a geometry specific plastic deformation.

Despite the poor model correlation, it is believed that the calculated value for the activation energy,  $Q$ , is still valid. Recall from Figure 4.2.4 that  $Q$  was found from the slope of the constant stress lines plotting on a  $\ln(\text{strain rate})$  versus reciprocal temperature plot. The strain rates used to generate this figure were calculated using the Sato et. al.<sup>16</sup> beam bending equations. Due to the plastic hinge deformation, these equations are not valid, therefore the strain rates calculated are not valid. However, the calculated strain rates are proportional to the actual measured vertical deflection rates of the specimens. Knowing that the majority of the deflection was due to hinging at the inner load points, and assuming small deflections, it can be argued that the deflection rate is proportional to the angular rate of change at the hinge point. This angular rate in turn must be proportional to the characteristic rate of strain within the hinge that is governed by the activation energy,  $Q$ . Working the same logic backwards, it follows that the original calculated strain rate is proportional to the actual strain rate within the hinge. Therefore, substituting the new strain rate into Figure 4.2.4 would result in a vertical shift of the constant stress lines, but the slope, and thus  $Q$ , would remain unchanged.

### 4.3 PLASTIC HINGE INVESTIGATION

Looking at the shapes of the specimen samples in Figure 4.2.6, it is clear that much of the deformation is localized at the contact points. The cause of this creeping "plastic hinge" must be investigated so that useful data may be extracted from the creep tests.

#### 4.3.1 DISLOCATION PILE-UP

The first step in the investigation is to look at the load-deflection curves generated by Chen<sup>23</sup>. Each of the curves is characterized by an initial sharp rise and then sudden fall after peaking at some maximum load value. Figure 4.3.1 shows a silicon load deflection curve at 800°C with a piston speed of 2 $\mu\text{m/s}$ . Materials that exhibit these load-deflection characteristics will plastically collapse under dead loading far more suddenly and catastrophically than materials that have a gradual decline after the peak load value is reached<sup>24</sup>. Typically, to avoid failure by

plastic collapse, a designer will assign an appropriately high "load factor" to ensure that the material load will never approach the peak of the load-deflection curve.

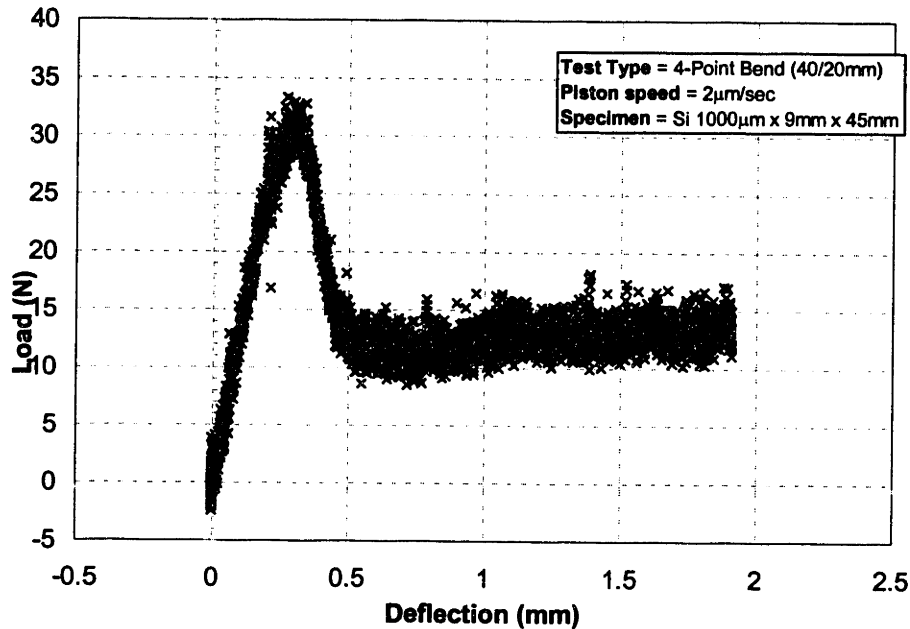
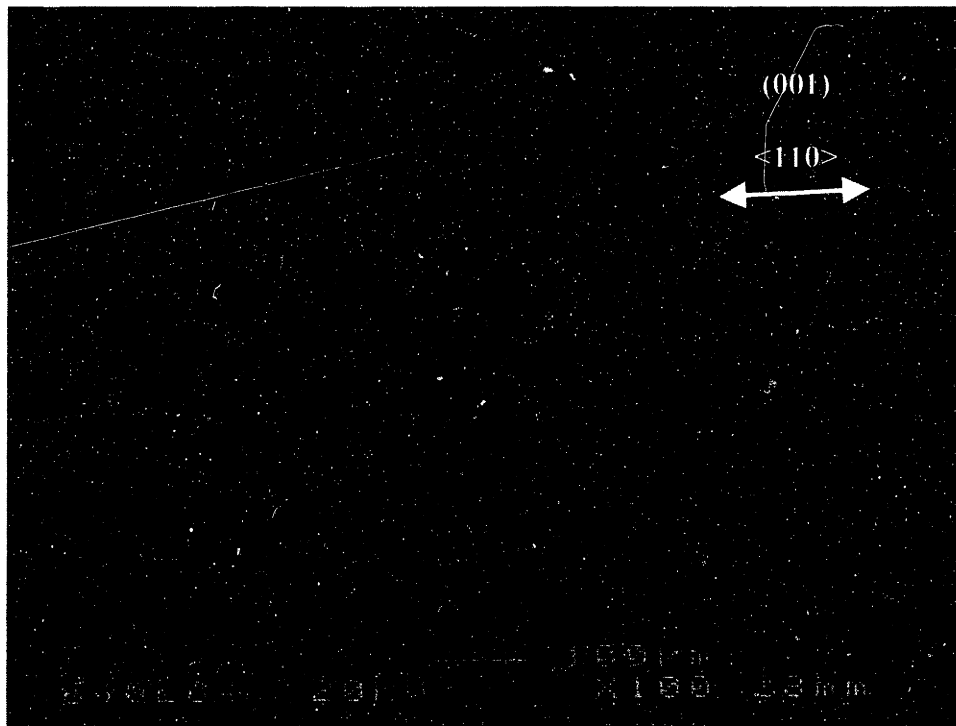


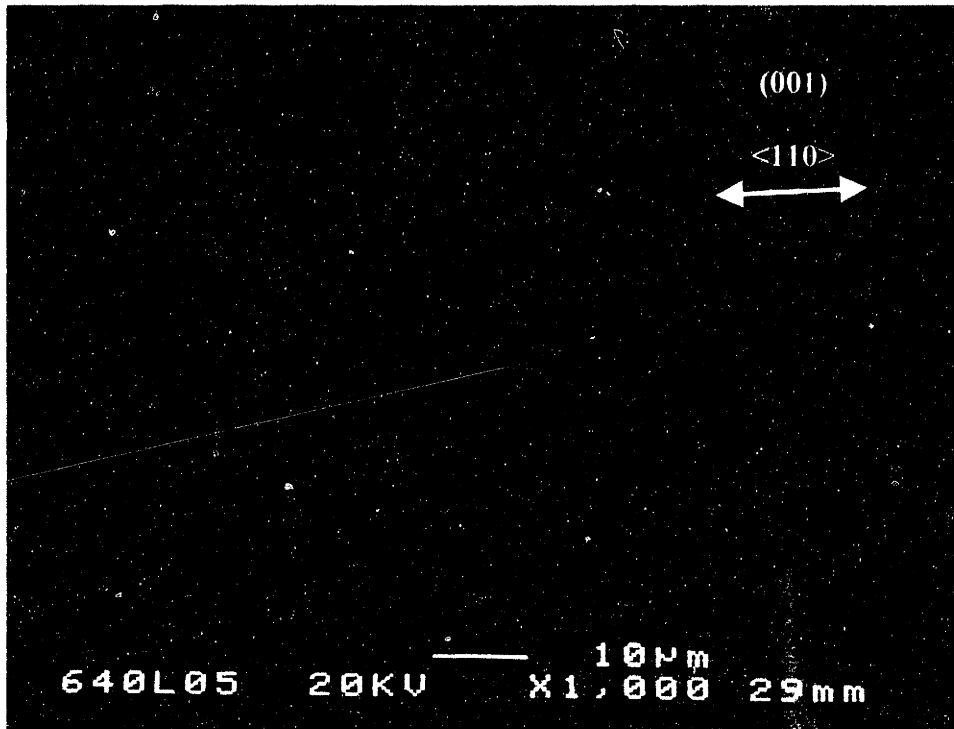
Figure 4.3.1: Silicon load vs. deflection curve at 800°C.

Material that has undergone plastic collapse will display certain telltale signs in its microscopy. In particular, dislocation "pile-ups" will be evident in the location of the plastic collapse. Hull and Bacon<sup>25</sup> describe the dislocation pile-up mechanism as follows:

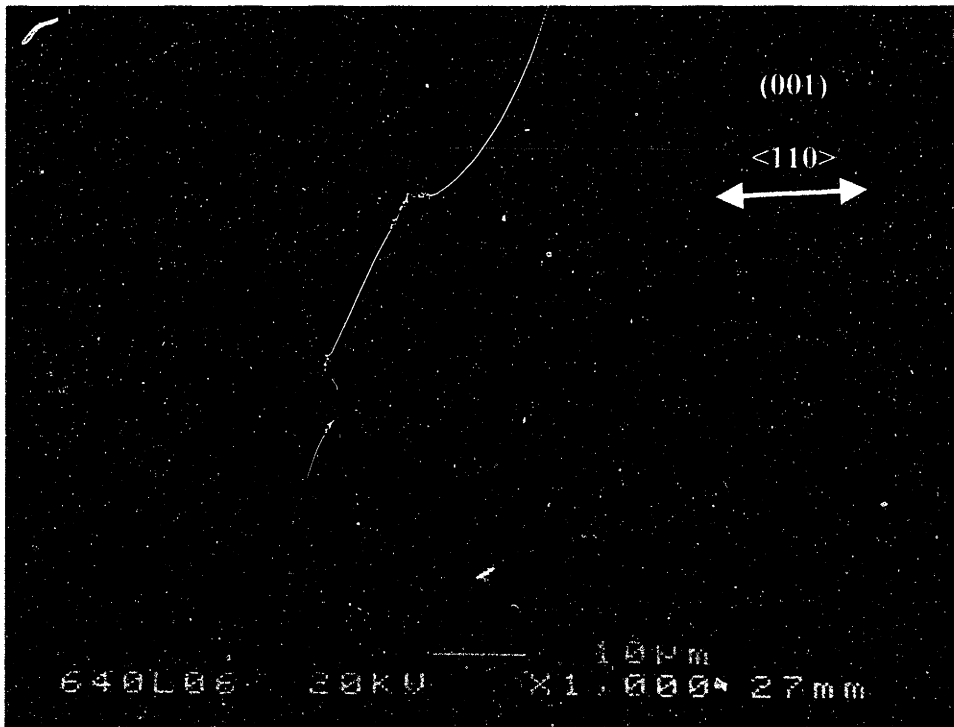
1. A dislocation source produces dislocations on a particular slip plane until the leading dislocation contacts a boundary. In the case of the single-crystal silicon, the edge of the specimen is the most prominent boundary.
2. The lead dislocation is blocked by the boundary. As the source continues to emit, the subsequent dislocations pile-up behind the leader. The dislocations can not combine since they are all of the same sign.
3. The local stress in the area of the lead dislocation increases as the pile-up continues.

To verify that this phenomenon occurred in the creep testing, a sectioned specimen was prepared from a representative silicon sample. The specimen tested at 700°C and pictured in Figure 4.2.6 (c) was used for the analysis. The specimen's top surface, where the inner load-point rollers contacted, was viewed through a scanning electron microscope (SEM) prior to sectioning. Figure 4.3.2 shows various magnifications of the load-point surface. Photo (a) shows a 100X view of the top surface of the specimen where it contacted the inner load-point roller. Slip lines perpendicular to the  $\langle 110 \rangle$  direction are visible and have a high density in this region confirming the presence of extensive plastic deformation. Photo (B) is a 1000X view of the same location. Additional slip lines are visible at this magnification. For comparison, photo (c) was taken at 1000X on the top surface of the specimen midway between the inner and outer load points. No slip lines are present in this view, supporting the observation that most of the deformation was localized to the inner contact points.





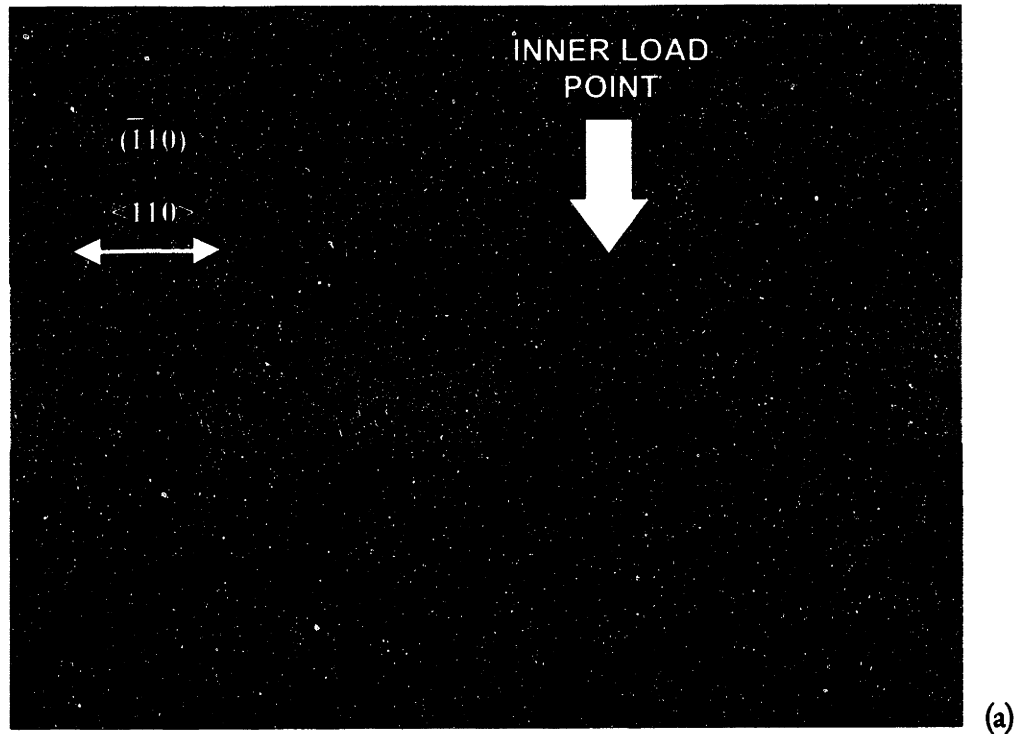
b)

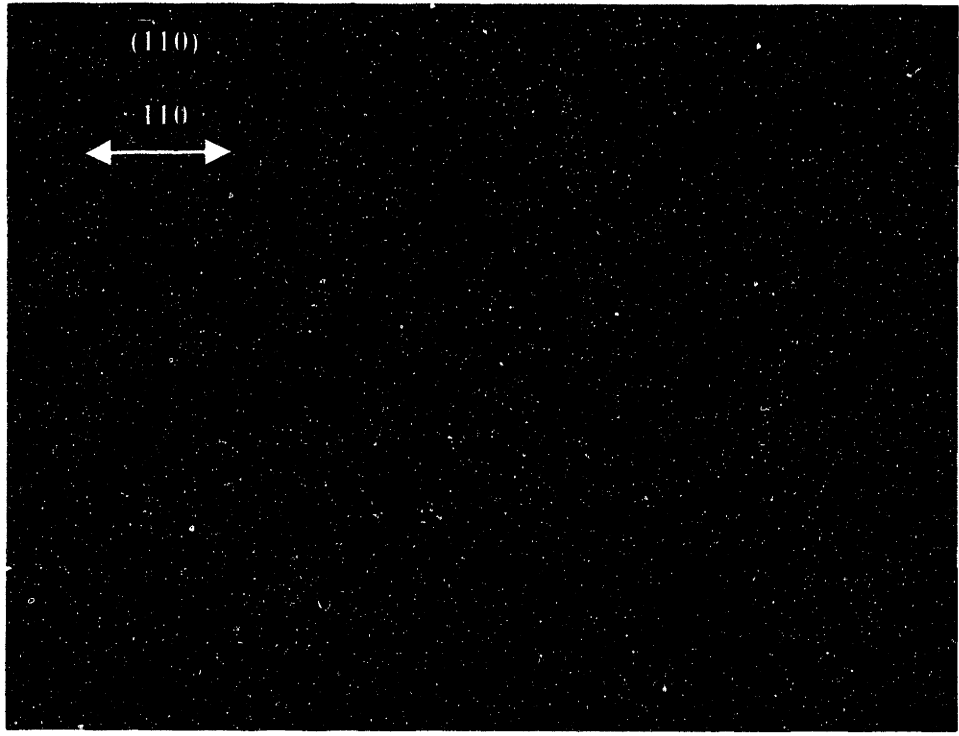


(c)

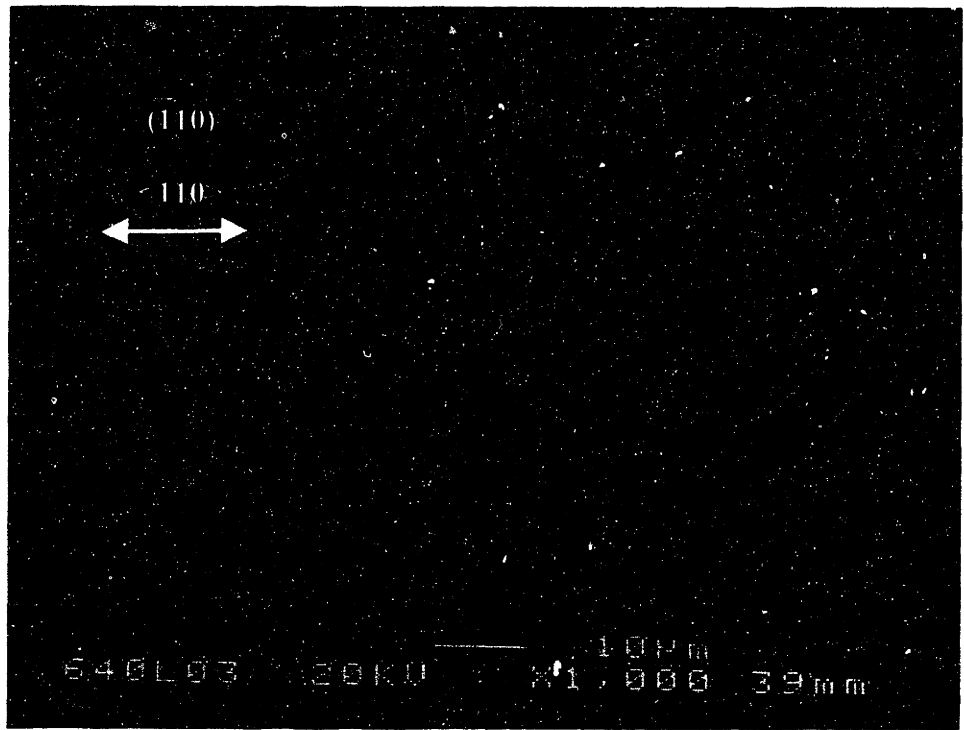
Figure 4.3.2: Silicon specimen inner load-point surface (SEM image). (a) 100X, (b) 1000X, (c) 1000X away from load-point.

A cross-section of this specimen was taken at one of the inner load points. The specimen was mounted on its side in epoxy and then ground down so as to expose the  $(\bar{1}10)$  plane of the silicon. The ground specimen was then polished progressively, finishing with sub-micron alumina grit. Finally the specimen was etched with a solution of (97%  $\text{HNO}_3$ , 3% HF (55%)) for 60 seconds to expose the dislocation and slip planes. Figure 4.3.3 shows several magnified views of the load point. The active slip planes, which have accumulated dislocations, appear as dark lines. The slip corresponds to the  $\langle 111 \rangle$  direction as is expected for a diamond cubic structure. The density of active slip lines is far greater at the load point than anywhere else in the specimen. The pictures confirm the theory that the specimens underwent dislocation pile-up process resulting in localized plastic collapse.





(b)



(c)

Figure 4.3.3: Magnified views of the specimen cross-section.  
(a) 20X, (b) 100X, (c) SEM image near top, 1000X. Photos are not to scale.

### 4.3.2 SOURCES OF STRESS

To complete the plastic collapse theory, the presence of sufficiently high stresses to cause the collapse phenomenon must be explained. First the maximum creep test stresses (based on applied load and assuming no creep relaxation) will be compared to the yield strength calculated for various temperatures by Chen<sup>23</sup>. A plot of the comparison is shown in Figure 4.3.4. The yield curve derived by Chen is shown in APPENDIX A.13. Although several of the points do fall above the yield stress curve, the majority of them do not. Therefore, the stress due to bending is not sufficiently high to cause plastic collapse in every case.

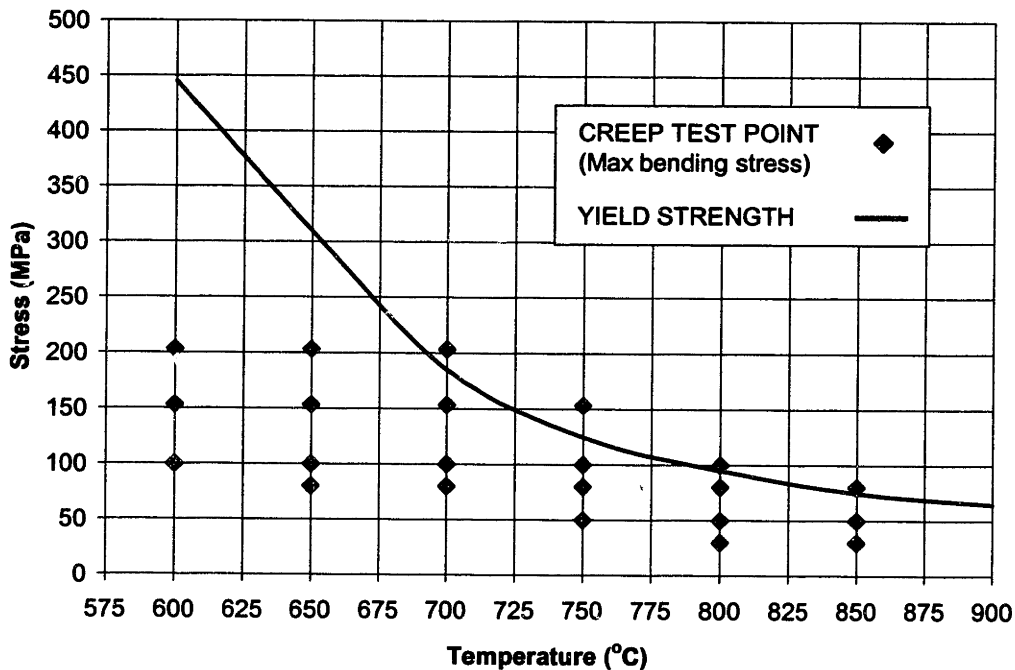


Figure 4.3.4: Creep test stresses versus yield strength.

Given that the load-point rollers are 5 mm cylinders, it is likely that a significant "Hertzian"<sup>26</sup> contact stress arises at the load-point. Although this stress is localized at the roller, if combined with the bending stress it were to exceed the yield strength of the material, local yielding would ensue, which combined with the stress softening behavior of the silicon, would result in collapse of the specimen.

Shigley and Mischke<sup>26</sup> describe the calculation of contact stresses between two cylinders as shown in Figure 4.3.5. The cylinders can be any length,  $l$ . The half-width,  $b$ , of the contact



surface area, is calculated from the equation,

$$b = \sqrt{\frac{2F(1-\nu_1^2)/E_1 + (1-\nu_2^2)/E_2}{\pi\ell(1/d_1 + 1/d_2)}} \quad (4.3.1)$$

where, F is the load-point force (which is equal to half of the 4-point bend fixture applied force),  $\nu$  is the Poisson's ratio and E is the Young's modulus. Since the silicon specimen is a flat plate and not a cylinder, the cylinder diameter, in Equation 4.3.1 is set to infinity. The maximum pressure at the contact surface is given by,

$$P_{\max} = \frac{2F}{\pi b\ell} \quad (4.3.2)$$

The stresses at the surface can then be calculated as,

$$\sigma_x = -2\nu p_{\max} \quad (4.3.3)$$

$$\sigma_y = \sigma_z = -p_{\max} \quad (4.3.4)$$

Now if the maximum bending stress is added to the contact stress, the maximum local stress at the contact surface can be calculated. These calculations were performed in MathCAD and are included in APPENDIX A.14. It should be noted that this calculation over-estimates the magnitude of the contact stresses since it under estimates the compliance of the bend specimen. However, it should provide an upper bound on the local stress magnitudes.

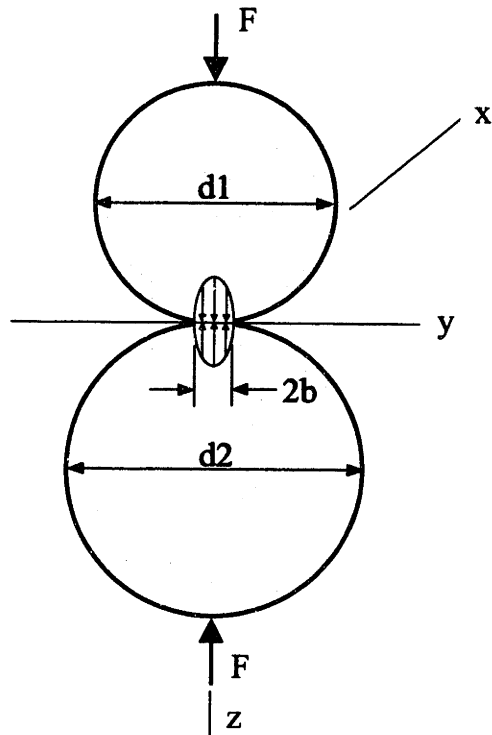


Figure 4.3.5: Contact stresses between two cylinders.

Consistent with Figure 4.3.4, the total stress (contact plus bending) is plotted versus the yield strength in Figure 4.3.6. It appears that at almost every test point, the stress on the surface of the specimen is close to or exceeding the yield strength of the material. The implication is that under ideal testing conditions (i.e. no surface imperfections, impurities, or other potential stress concentrations), the normal testing loads may be causing plastic collapse of the specimens.

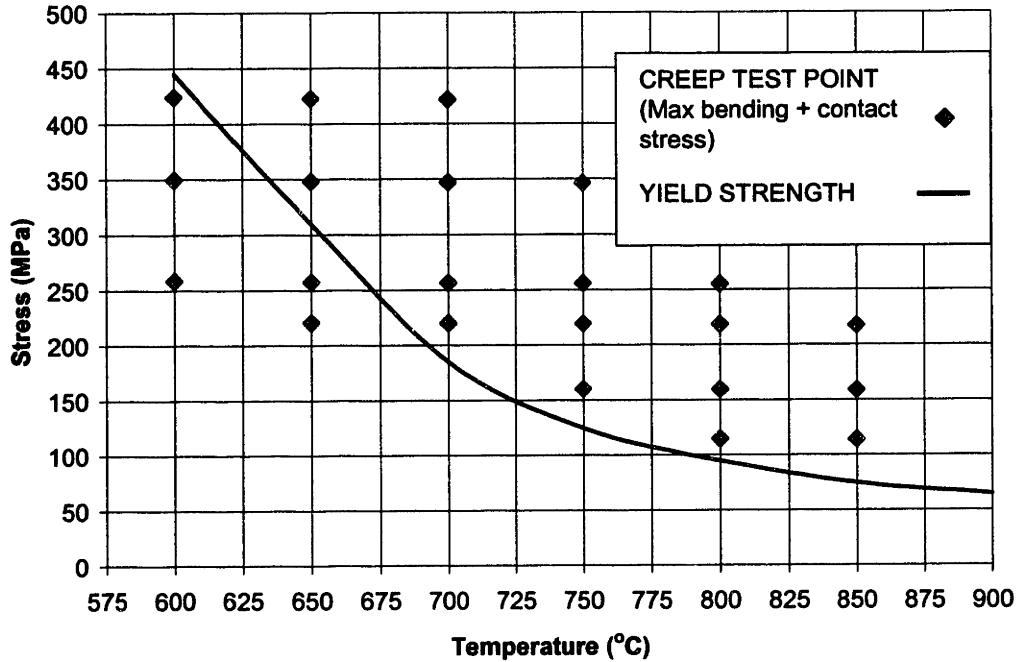


Figure 4.3.6: Contact + maximum bending stress versus yield strength.

If the contact stress is the driving force behind the plastic collapse, then evidence of this phenomenon should be present on the yield strength specimens tested by Chen<sup>23</sup>. Therefore, profiles were taken of three specimens tested by Chen at 700°C. The specimens were loaded at rates of 2µm/s, 5µm/s and 10µm/s and are shown in Figure 4.3.7. The 2 specimens which were loaded more quickly (5µm/s and 10µm/s) do not show any signs of hinging, but the part loaded at 2µm/s exhibits the same plastic collapse characteristics as the creep specimens. Figure 4.3.8 shows the top surface at the inner load-point of the yield test specimen that was loaded at a rate of 5µm/s. Compared to the creep specimen in Figure 4.3.2, there are relatively few active slip planes showing. Clearly, the collapse mechanisms which are present in the creep specimens are not active in this yield test specimen.

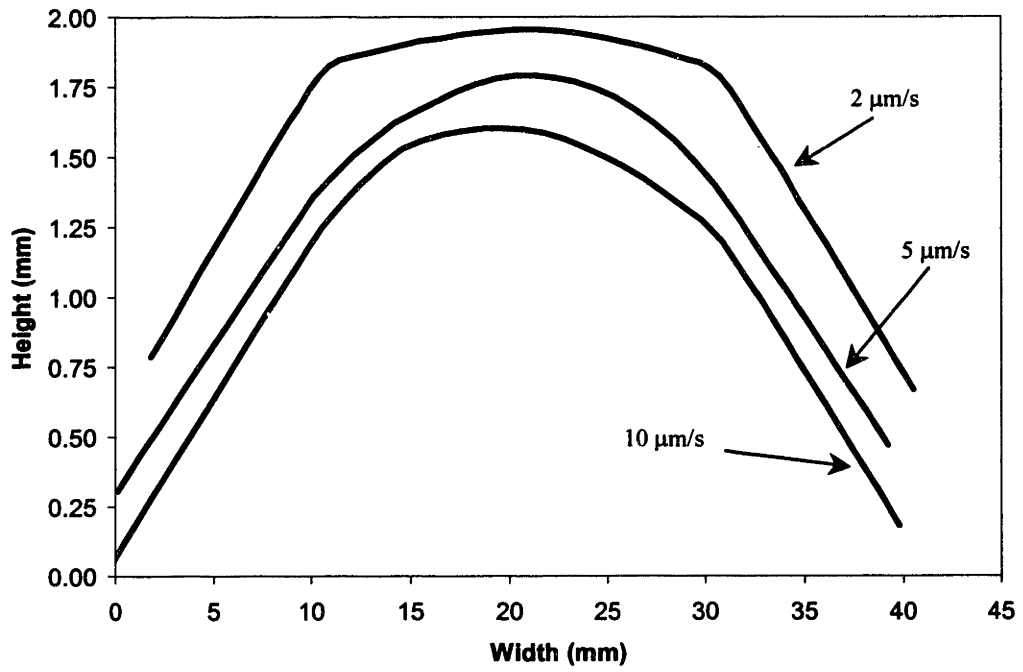
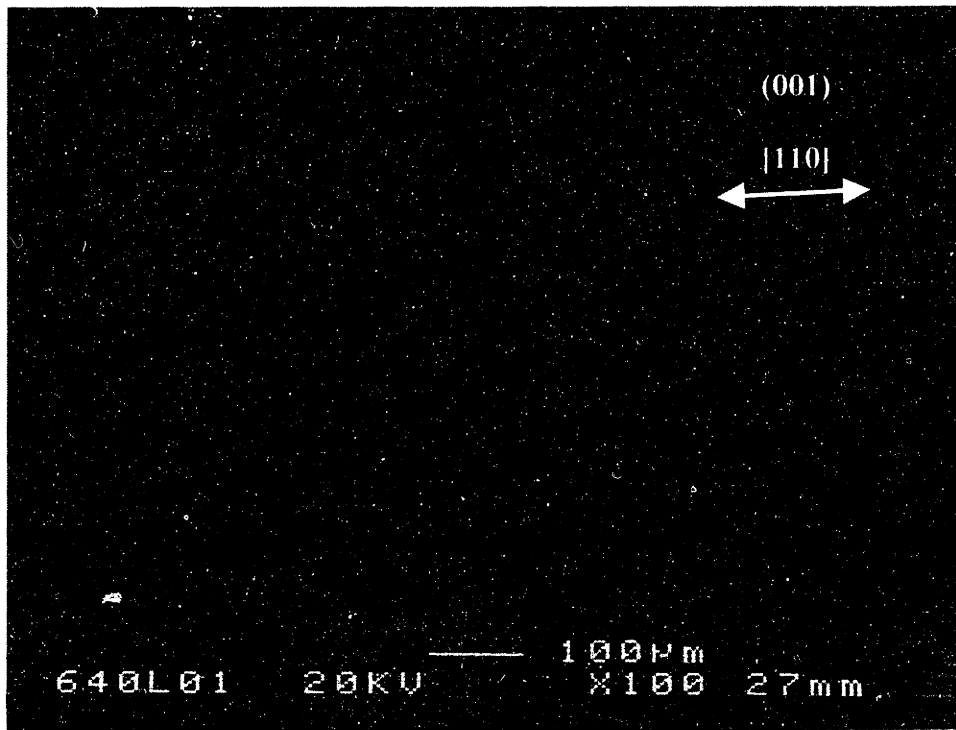


Figure 4.3.7: 700°C yield test specimen profiles.



(a)

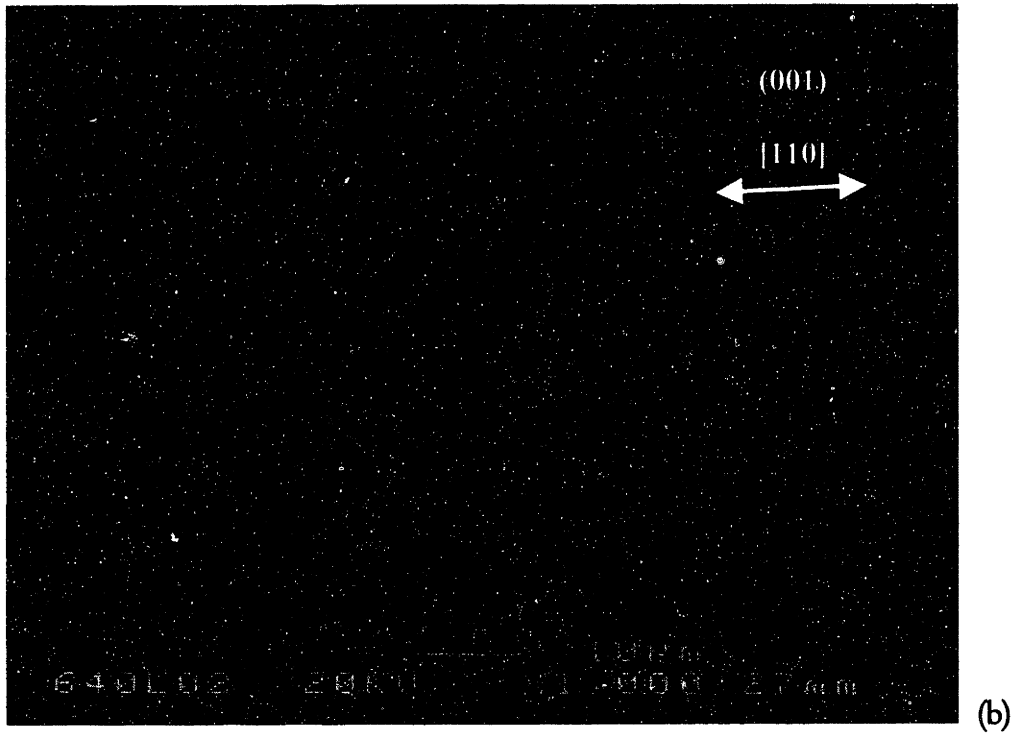


Figure 4.3.8: Yield test specimens inner load-point surface (SEM images). (a) 100X, (b) 1000X.

## CHAPTER 5 DISCUSSION

### 5.1 IMPLICATIONS FOR THE MICROENGINE PROJECT

The findings of this thesis have far-reaching implications for the design of the demonstration micro-engine. The operating environment in the turbine of this engine will be pushing the limits of the load bearing capability of the single-crystal silicon structure. The turbine temperatures of the demonstration engine, as determined by Ye, and presented to the Army Research Office in April of 1999<sup>27</sup>, are shown in Figure 5.1.1. The maximum stress location is the turbine blade root fillet. A tradeoff study of fillet size versus stress was presented and is shown in Figure 5.1.2. Based on these figures the root fillet will operate just under 700°C with a stress of 125 MPa.

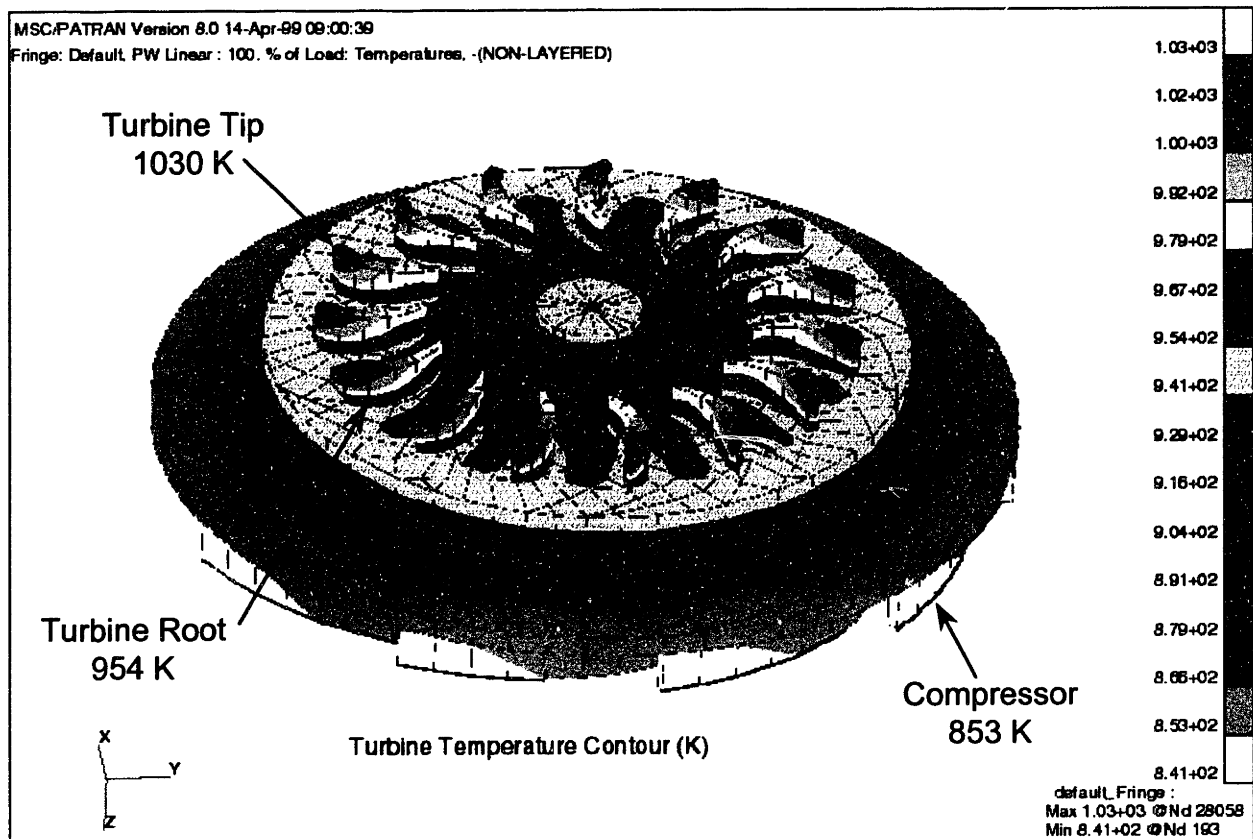


Figure 5.1.1: Turbine temperatures (K)

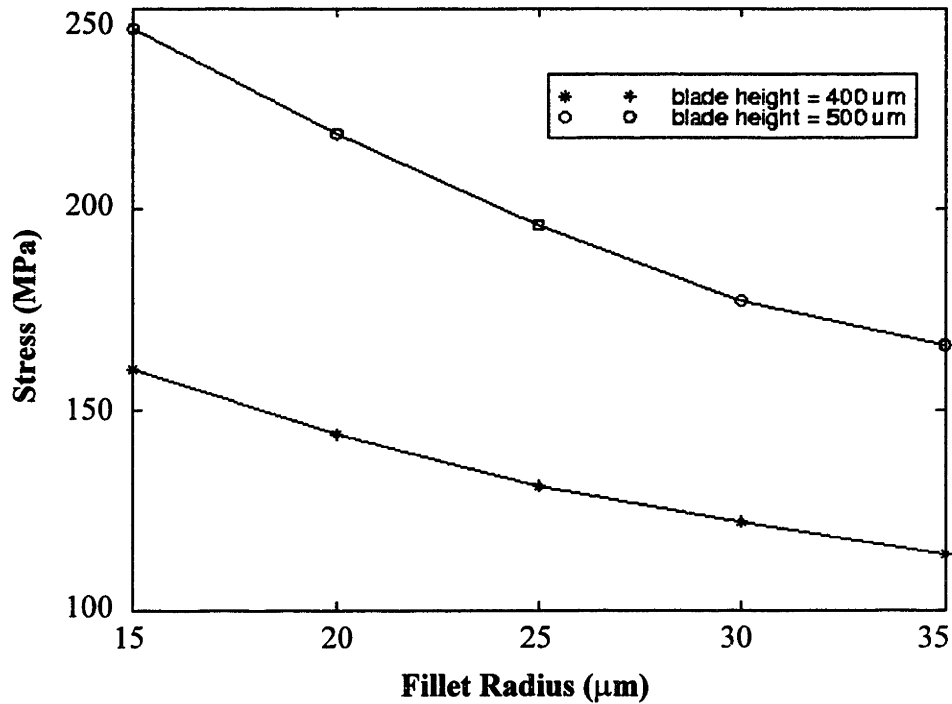


Figure 5.1.2: Fillet radius tradeoff study.

The evidence of plastic collapse in the creep testing, combined with the steep downward slope of the load-deflection curve (Figure 4.3.1), are critical factors in the design of the turbine. The designers must be sure to maintain sufficient margin between the working load and the maximum load that the structure can withstand. If the stress in the root fillet were to exceed the yield strength of the material, even just transiently, due to the nature of the material, a catastrophic plastic collapse could result and the blades would "fold over". From the work of Chen<sup>23</sup> on yield strength, at 700°C the yield strength of single-crystal silicon is approximately 180 MPa. Therefore the root fillet stress is 70% of the yield stress at this temperature, giving a nominal factor of safety of 1.43.

Ideally, the creep tests performed for this thesis would have yielded a constitutive equation, such as the power law model, for use in designing the demonstration engine. However, to extract the necessary data from the tests assumptions must be made regarding the nature of the deformation and stress state. In particular, the stress and strain are assumed to follow classical beam bending theory as described by Hollenberg et al.<sup>15</sup> and Sato et al.<sup>16</sup>. Unfortunately, the

observation of plastic collapse suggests that phenomenologically this model would not be valid. Therefore it will not be used for the demonstration engine design.

However, from the data, it is possible to draw some guidelines for design. One frequently used method for describing creep is the Larson-Miller parameter. This method combines time and temperature effects into one parameter that can be plotted versus stress. The Larson-Miller parameter is defined as,

$$P = T(\log(t) + C) \quad (5.1.1)$$

where  $C$  is a constant,  $T$  is temperature in degrees K and  $t$  is the time in hours to reach a critical strain. Historically  $C$  was set at a constant value, typically 20, but today it is more common for  $C$  to be optimized for the particular set of data. To optimize  $C$  from the test data,  $\log(t)$  is plotted versus  $1/T$ . Constant stress lines are drawn and the point at which they intersect the  $\log(t)$  axis is the value of  $C$ . For the creep test data presented in this thesis, this plot is shown in Figure 5.1.3. Due to limited data, several of the constant stress lines stray, but the majority of the lines converge around  $C = 11.5$ .

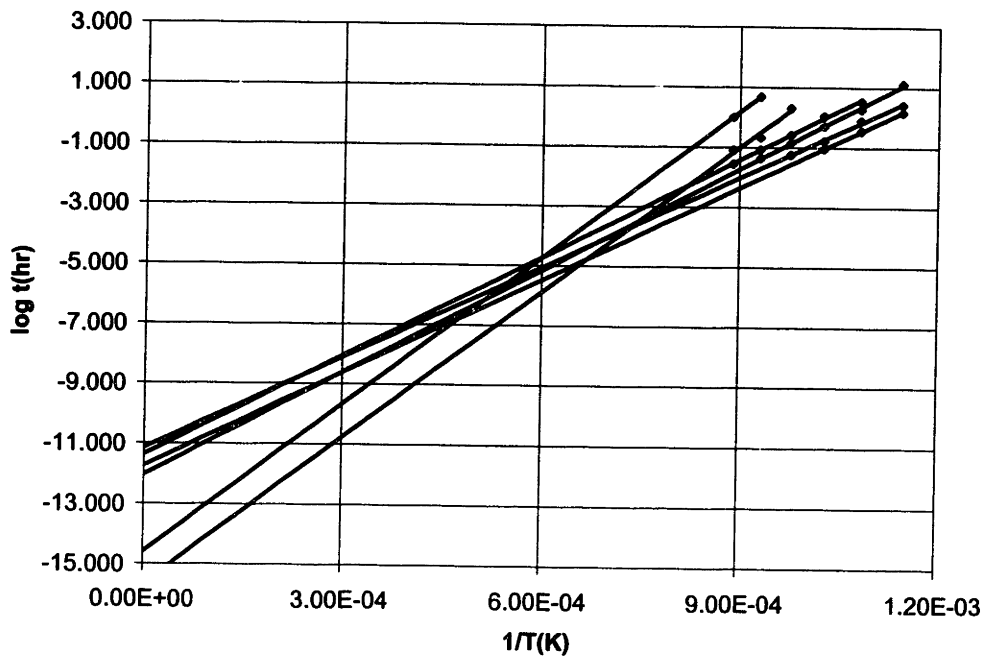


Figure 5.1.3: Plot to determine Larson-Miller Parameter  $C$ .



Next, Larson-Miller parameters are calculated for each data point based on the temperature and time to reach a critical strain. For this case the critical strain will be defined as 0.5%, which corresponds to the strain level at which a 15  $\mu\text{m}$  bearing gap on a 3 mm radius disk would be closed. This parameter is then plotted versus stress to develop the design envelope. Given the uncertainty regarding the actual stress values in the creep testing, two stress calculations are considered for each test point to generate an upper and lower bound to the curve. The lower curve assumes that the stress comes entirely from bending and stress relaxation is present with a power law creep exponent of  $n=3$ . This curve will be extremely conservative since it is known (from the plastic collapse evidence) that actual stresses far exceeded these levels. The upper bound will be generated assuming the stress felt by the specimen is a combination of bending stresses with no creep relaxation, and contact stresses due to the load point roller. This curve is aggressive but possibly realistic. Figure 5.1.4 is the design curve that was developed. The data for this plot is included in APPENDIX A.15.

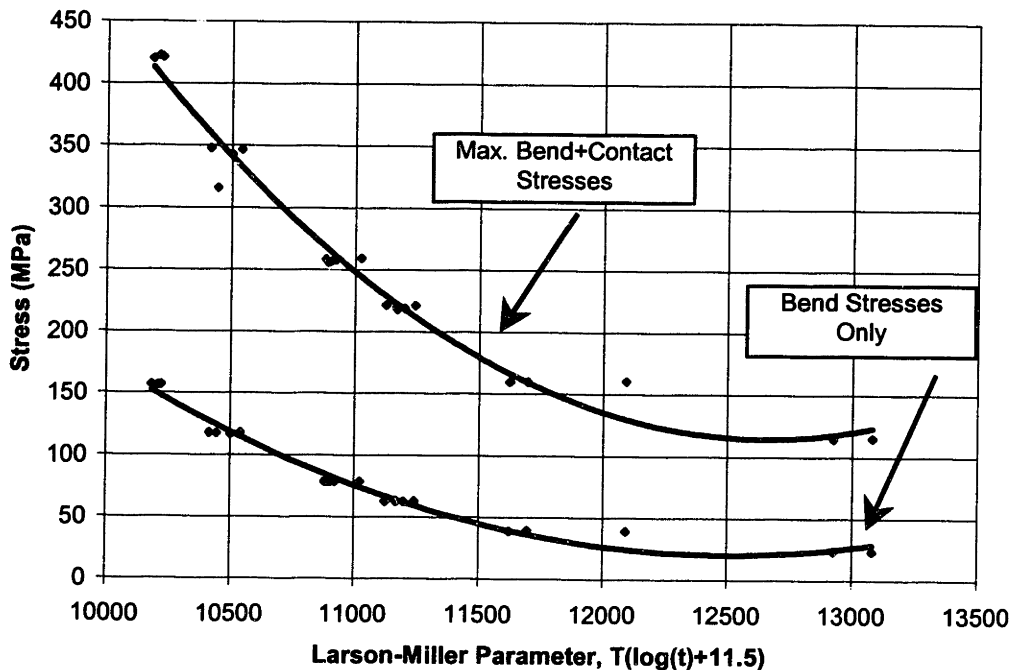


Figure 5.1.4: Larson-Miller Parameter design curve.

A Larson-Miller design curve is usually only applicable within the limits of the test

condition, therefore no extrapolation is allowed. However, if sufficient information is known about the material behavior under conditions beyond those used to create the curve, the extrapolations could be justified. In the case of silicon, it is well documented that following the steady state creep regime (stage II) which was the focus of this thesis, is an extended period of slowed growth<sup>13</sup>. Therefore, extrapolation of time "t", is justified in this case, since the strain rate will be no greater than that which was tested. However, extrapolation of temperature is not justified. The time and temperature ranges tested are listed in APPENDIX A.15. Based on the Larson-Miller upper bound and assuming a turbine root radius maximum stress of 125 MPa and an operating temperature of 690°C, the engine should operate for nearly 15 hours prior to reaching 0.5% strain. The lower bound, however, would predict that the engine will reach the 0.5% strain point in only 12 minutes.

## 5.2 IMPROVED CREEP TEST SUGGESTIONS

To accurately characterize the creep behavior of silicon additional creep tests must be performed. These tests must be effectively designed such that the associated stresses can be accurately calculated. Several methods are proposed which can be pursued as a continuation of the work performed in this thesis.

### 5.2.1 MODIFIED 4-POINT BEND TEST

One such method is a modified 4-point bend test. Based on the localized presence of active slip bands at the inner load point, it was concluded that in the initial creep tests the local contact stress, combined with the applied bending stress, exceeded the yield strength of silicon, resulting in plastic collapse. It can therefore be deduced that sufficiently reducing the stress at the load point will eliminate this problem. A specimen geometry similar to that shown in Figure 5.2.1 could achieve this desired result. By thickening the specimen at the load points, the bending stress could be minimized such that the yield strength would not be exceeded.

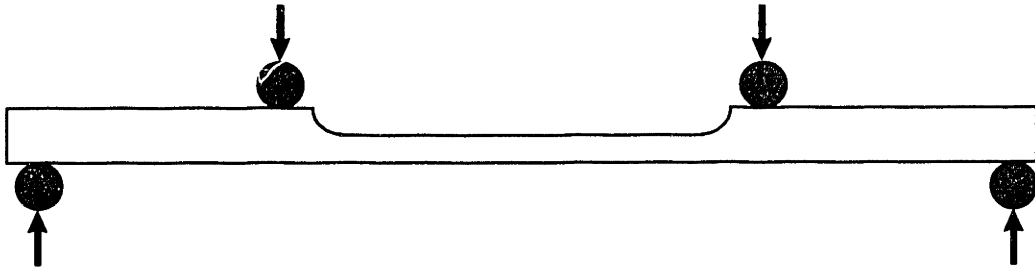


Figure 5.2.1: Modified 4-point bend test method.

Testing by this method could proceed in a similar manner as that outlined in Section 4.2 of this report. However modification of the power law constitutive equations presented by Sato et. al.<sup>16</sup> may be necessary. These equations were developed assuming a beam of constant cross-section. The additional material added at the load points could result in an underestimated creep rate if not accounted for. Once the creep parameters  $Q$  and  $n$ , from equation 2.2.4, have been determined, the coefficient "A" can be backed out if the stress level is known. However, given the potential stress multiplier in the radius of the specimen, it is more appropriate to correlate the results to a finite element model by varying "A" in the creep equation input. Recall that this was attempted for the creep data presented in this thesis, but the stress concentration effect at the load point could not be duplicated.

A specimen of this type would permit the variation of the fillet radius and surface condition to explore their influences on the onset of creep deformation. Functionally, this geometry is closely related to the conditions at the blade roots in the demonstration engine, which is the location at which creep is of greatest concern. Also, tests at different orientations could be performed to confirm the assumptions made regarding the relative directional strengths.

In conclusion it should be noted that the 1 mm silicon specimens tested for this thesis may not be thick enough to accurately fabricate the desired specimen geometry. Therefore, it might be necessary to use significantly thicker specimens which would have to be custom fabricated resulting in higher testing costs.

### 5.2.2 COMPRESSION TEST

Another potential creep testing method is the compression test. There has been significant use of the compression test for creep characterization, but to date there is no published standard specifically addressing creep<sup>28</sup>.

A typical compression creep test involves a test fixture similar to that shown in Figure 5.2.2. The specimen is loaded between two plates, through which the load is applied. One of the primary concerns with compression testing is the uncertainty of the end conditions. Debschutz<sup>29</sup> et. al. reported that the amount of end friction present can dramatically effect the distributed stress levels and can result in "barreling" of the specimen. In addition, they found that increasing the height to base ratio of the specimen could reduce the impact of friction. Unfortunately, this leads to the other downfall of compression tests, which is the potential for buckling. To further minimize the frictional effects, high temperature lubrications (such as MoSi<sub>2</sub> or BN) should be used on the load surfaces.

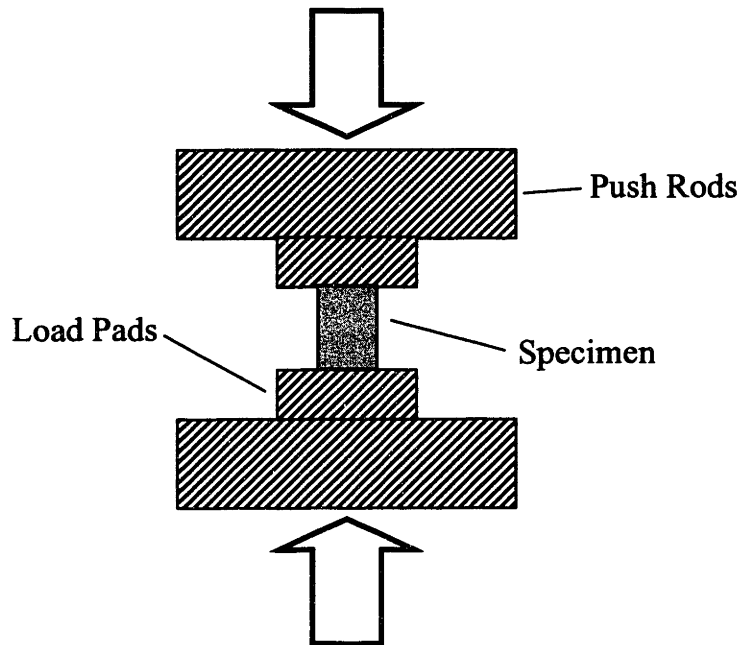


Figure 5.2.2: Typical compression fixture.

For testing in support of the micro-engine, it may be practical to test a specimen fabricated

from a fused stack of single-crystal silicon wafers. Testing a single 1 mm thick wafer would require at best a 1x1 mm specimen, however a height to base ratio of 1.5 to 3 is preferred<sup>28</sup>. At that scale errors in specimen dimensions and deformation measurements would be magnified. Again, another option is to use monolithic specimens which could be obtained for an additional cost to the program.

The most critical aspect of the compression test is accurate measurement of the specimen deformation. Several of the more commonly used techniques are:

1. Measurement of the loading ram displacements<sup>30,31</sup>. This method is only valid where specimen strains are large in comparison to thermal strains<sup>28</sup>.
2. Feeler gauges which extend into the furnace and measure the upper and lower surfaces on the specimen<sup>29,32</sup>. Accuracy of these feeler gauges can be better than  $\pm 1\mu\text{m}$ <sup>28</sup>.
3. Long range microscope<sup>33,34</sup>. Typically, measurements using this method are performed by attaching small silicon carbide fibers to the load plates. This provides a sharp viewing point for the microscope. Accuracy of this methodology can run as high as  $\pm 4\mu\text{m}$ .

### 5.3 MODELING

An advantage to the compression method is that the specimens can be easily tested at different crystal orientations. If creep is assumed to result from slip along crystallographic slip planes, then the corresponding slip rate on the active slip system can be determined from experimental testing. This could be performed on each valid slip system, resulting in a complete crystallographic creep definition. Becker et. al.<sup>35</sup> performed a similar analysis on single-crystal aluminum. They characterized the slip rate using a power law relationship of the form,

$$\dot{\gamma}^{\alpha} = \dot{a} \text{sign}(\tau^{\alpha}) \left| \frac{\tau^{\alpha}}{q(\gamma)} \right|^{1/m} \quad (5.3.1)$$

where,  $\dot{\gamma}$  is the slip rate on the slip system,  $\dot{a}$  is a reference slip rate characteristic of the

experimental strain rate,  $\tau$  is the resolved shear stress on the slip system,  $q(\gamma)$  is the shear system strength or hardness,  $m$  is the rate sensitivity exponent, and  $\alpha$  denotes the slip system. The complete creep definition resulting from this analysis could be used in a finite element model to predict the plastic hinge effect seen in the initial silicon creep testing described in this work.

#### 5.4 IMPACT ON THE MICRO-ENGINE DESIGN

The future creep testing of silicon should not just focus on obtaining unidirectional creep properties, but instead, should take into consideration the variation of strength properties with crystal orientation. The engine structures are subjected to three dimensional stress states, therefore the material anisotropy must be properly accounted for.

Knowing that the silicon material strength is orientation dependent, it follows that on the bladed rotors of the demonstration engine, there will be quantifiable strength differences from one blade to the next. Each blade will have a slightly different crystallographic orientation and will therefore vary in strength capability. To counter the orientation effects, it may be worthwhile to generate some balanced asymmetry into the design of the rotor that reduces the stress levels in the "weaker" blades. Such a design might include variations in the root radius, blade thickness and blade height.

## CHAPTER 6 CONCLUSIONS

### 6.1 SUMMARY

The purpose of this thesis research was to develop a constitutive equation defining the creep behavior of single-crystal silicon. The data was to be used by the MIT micro-engine design team for optimizing the structural design of the all-silicon demonstration micro-engine. The specimens for the creep tests were prepared from 1 mm thick (100) single-crystal silicon wafers. Each specimen was cut into a rectangular shape with the length oriented in the  $\langle 110 \rangle$  direction.

The creep tests were performed in 4-point bending using a hydraulically actuated constant load controller. Based on the operating environment of the demonstration engine, the test envelope was defined to include temperatures of 600-850°C and loads ranging from 9-45 N. The test data was reduced using Hollenberg et. al.<sup>15</sup> beam-bending techniques, as modified by Sato et. al.<sup>16</sup> These methods assume a power-law relationship of the steady-state "stage II" creep data. Using these techniques, a creep exponent of  $n=3$ , and an average activation energy of  $Q=208$  kJ/mol, were found for the silicon tested in this thesis. To obtain the final power-law creep parameter,  $A$ , a finite element model was created to simulate the test conditions. However, due to localized deformation at the 4-point bend inner load contact points of the tested specimens, correlation between the model and the actual parts could not be obtained.

To better understand the observed localized plastic deformation at the inner load points, the microstructure of the tested specimens was studied. In particular, two surfaces of the specimens were inspected: the top "loading" surface, and the lengthwise cross-section. High concentrations of slip bands were visible on the top surface of the tested specimens at the inner load points. Away from the load point, there were very few. A lengthwise cross-section revealed dense dislocation pileups directly beneath the inner load points. These observations confirm that normal beam-bending creep did not occur on these specimens, thus invalidating the assumptions

made using the power-law model. Instead, stress concentrations, due to loading, resulted in a localized plastic collapse of the specimens beneath the inner load points.

## 6.2 CONCLUSIONS

- Single-crystal creep deformation in the range of 600-850°C and 30-200 MPa (as calculated assuming a creep exponent of 3) is dominated by localized deformation in the form of creeping plastic hinges.
- The collected creep data is not conducive to reduction in the form of the power law continuum model, due to the observation of localized loading point deformation.
- For single-crystal silicon specimens cut from a (100) wafer with the  $\langle 110 \rangle$  direction oriented parallel to the lengthwise direction, under a bending moment, the  $\langle 111 \rangle$  slip planes were the principal mechanisms for the localized plastic deformation.
- An engineering approach, using a Larson-Miller parameter indicates a useful life of the current micro-engine design in the range of 12 minutes to 15 hours. However, the 12 minutes estimate is considered to be very conservative while the 15 hour estimate could be accurate.

## 6.3 FUTURE WORK

To properly define the micro-engine geometry, accurate information regarding the creep behavior of single-crystal silicon is required. The creep testing performed in support of this thesis resulted in localized specimen deformation, thus rendering the results inconclusive. Therefore, additional creep testing is necessary.

Two methods have been identified for future testing: a modified 4-point bend specimen thickened under the loading points, and a standard compression test. Each method effectively reduces localized stress concentrations, therefore avoiding the uncertainties with the local loading encountered using a standard 4-point bend test. The strength of single-crystal silicon varies based on orientation, therefore it would be useful to perform the additional tests at



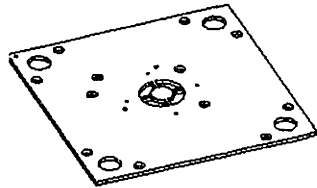
different orientations, so that a complete definition of the creep behavior could be generated.

The creep tests performed for this thesis did not yield a constitutive equation for use in design, but critical information about the behavior of silicon was uncovered. The observations of plastic collapse combined with the load-deflection data collected by Chen<sup>23</sup>, highlight the importance of maintaining significant margin between peak stresses and the yield limit for the micro-engine design. If the yield limit is exceeded, even transiently, sudden collapse could result. A robust design should incorporate damage tolerant lifing techniques, typically reserved for use in the presence of cracks. Essentially, stresses surrounding the peak stress location should be sufficiently low to halt an advancing plastic collapse. In addition, the effect of orientation should be considered for the final design. An optimized design may include altering key stress drivers, such as blade root radius, thickness and height, on less favorably oriented blades.

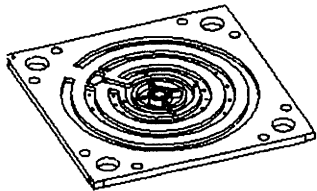
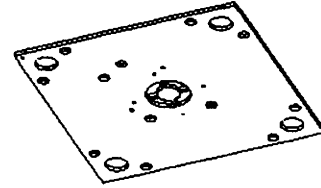
# APPENDIX

APPENDIX A.1	Micro-engine silicon wafer configuration.....	75
APPENDIX A.2	Loading System Specifications.....	76
APPENDIX A.3	Furnace and Controller Specifications .....	77
APPENDIX A.4	Sensing System Specifications.....	78
APPENDIX A.5	Labview™ Data Collection Program Details .....	80
APPENDIX A.6	Detailed Silicon Creep Testing Procedure.....	81
APPENDIX A.7	Silicon Creep Test Raw Data - Disp. (mm) vs. Time (s).....	87
APPENDIX A.8	Incremental Creep Test Data - Disp. (mm) vs. Time (s).....	98
APPENDIX A.9	Displacement Rate (mm/s) vs. Time (s) Plots .....	100
APPENDIX A.10	Strain Rate (1/s) vs. Time (s) Plots .....	111
APPENDIX A.11	ANSYS 5.4a Modeling Details: Finding the Proportionality Constant.....	122
APPENDIX A.12	ANSYS 5.4a Batch File: Finding the Proportionality Constant .....	125
APPENDIX A.13	MIT Single-Crystal Silicon Yield Test Results .....	130
APPENDIX A.14	MathCAD Contact Stress Calculations .....	131
APPENDIX A.15	LARSON-MILLER PARAMETER DATA .....	134

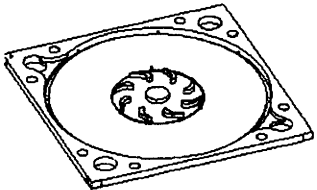
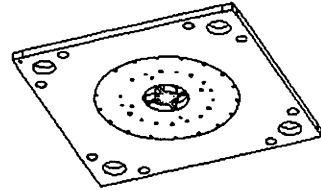
## EXPLODED ENGINE STACK



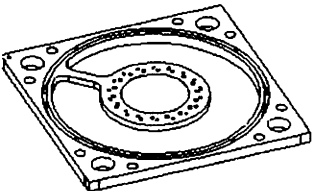
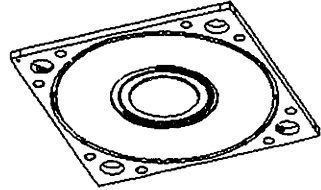
**FORWARD  
CAP PLATE  
(1)**



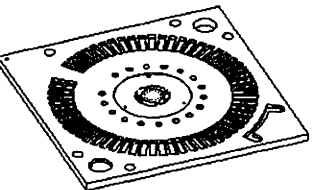
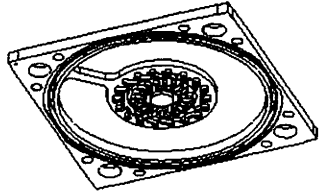
**FORWARD  
THRUST BRNG  
(2)**



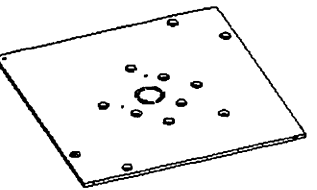
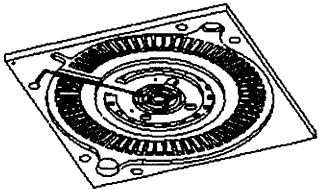
**COMPRESSOR  
(3)**



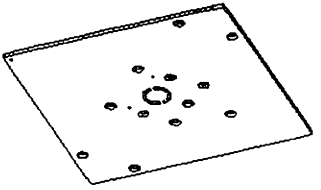
**TURBINE  
(4)**



**AFT  
THRUST BRNG  
(5)**



**AFT  
CAP PLATE  
(6)**



## APPENDIX A.2 Loading System Specifications

### PUSHRODS:

Material	Alumina
Dimensions	Upper: solid 25 mm diameter Lower: hollow 45 mm outside diameter, 30 mm inside diameter
Load Capacity	1 kN at 1500°C

### TEST FIXTURE:

Type	4-point, fully articulating
Material	Silicon Carbide
Dimensions	40 mm lower span, 20 mm upper span

## APPENDIX A.3 Furnace and Controller Specifications

### FURNACE:

Type	Single zone, split cylindrical
Dimensions	Height: 520 mm Diameter: 360 mm
Heating elements	6 Kanthal Super 33 (Molybdenum disilicide)
Temperature range	800 to 1500°C
Power requirements	3.6 kW
Thermocouples	2 Type B
Cooling water minimum flow rates	1 l/min for furnace 1 l/min for loadstring
Cooling water maximum pressure	6 bar
Cooling water maximum inlet temperature	30°C

### FURNACE CONTROLLER:

Type	Eurotherm 902P
Dimensions	Height: 625 mm Width: 550 mm Depth: 500 mm
Overtemperature protection	Eurotherm 92
Power supply	240 V, 50 Hz single-phase fused at 25A

## APPENDIX A.4 Sensing System Specifications

### DEFLECTION MEASUREMENT SYSTEM:

Type	LVDT operated by probe in lower compression rod
Range	$\pm 1$ mm

### 8500 CONTROL SYSTEM:

Processors	Motorola 68000, 68340, and Texas Instruments TMS320C31
Computer interface	GPIB 24-pin standard (IEEE-488)
Position Accuracy	$\pm 0.5\%$ of transducer full travel
Load/Strain transducer sensitivity range	0.6 mV/V to 60 mV/V
Position transducer sensitivity range	0.85 mV/V to 5.5 mV/V for full-scale
Resolution	1 part in 48,000 of $\pm 100\%$ of range in use (16 bits with 35% overrange)
Balance (load/strain)	$\pm 25\%$ of transducer full-scale
Proportional gain	Independently settable for each conditioner from -100 dB to 100 dB with a resolution of 0.01 dB.
Integral gain	Independently settable for each conditioner from 0 to 10 sec <sup>-1</sup> with a resolution of 0.01% of setting.
Derivative gain	Independently settable for each conditioner from 0 to 5 ms with a resolution of 0.01% of setting
Lag gain	Independently settable for each conditioner from 0 to 500 ms with a resolution of 0.01% of setting
Control loop update rate	5000 Hz

Servo valve update rate	5000 Hz
Analog compression update rate	5000 Hz
Waveform generator update rate	5000 Hz
Maximum cyclic frequency	500 Hz
Feedback update rate	5000 Hz
Analog peak/mean detectors rate	5000 Hz
Analog event detectors rate	1000 Hz
Digital input event detectors rate	1000 Hz
Cycle counter event detector rate	1000 Hz
Segment counter event detector rate	1000 Hz
Loop error event detector rate	1000 Hz
Continuous data logging rate (max.)	5000 Vectors/sec
Burst data logging rate (max.)	5000 Vectors/sec
GPIB command processing rate (min.)	125 commands/sec
Computer to model 8500 transfer rate (max.)	700,000 bytes/sec
Model 8500 to computer transfer rate (max.)	300,000 bytes/sec





## APPENDIX A.6 Detailed Silicon Creep Testing Procedure

### 1. PREPARING THE WORKPLACE FOR TESTING

- 1.1. Clean all SiC and Alumina ceramic surfaces with methanol to remove oils, residues, and particles.
- 1.2. Make sure the transducer tube-rod-probe assembly is seated properly on the LVDT pushpin.
- 1.3. Make sure the LVDT and Load Cell are reading properly and are calibrated (flashing "SET-UP" lights indicate they need to be calibrated). Follow "Auto Calibration" procedure for Load cell calibration.
  - 1.3.1. For LVDT Calibration, use the following "Manual Procedure":
    - Press "set-up". Verify the LVDT is depressed so that it is at an appropriate ZERO point (use hydraulics).
    - Select "Calibrate", "Manual", "Coarse Balance", "Go".
    - Relay on. It will span the range. When it is settled and is reading 1mm. Press "Go" again.
    - Relay off. Fine balance --> Zero point --> "Go". Will stop blinking when finished.
- 1.4. Check that the channels are properly assigned on the Instron control panel. "A" for displacement. "X" for Load. "B" for position. "A" and "B" should be set to output "TRACK" values, while Load should output "FILTERED" values.
- 1.5. Check that the cables are connected from mechanical controller to circuit board properly. "A" goes to left receptacle, "B" to center, and "X" to right port.
- 1.6. Check that the AD converter is grounded (thin wire connected to wall outlet screw).

- 1.7. Load up “Kuo-Shen Data Acquisition” found in “41-219/KuoShen/labview”. Ensure that the units and gain values are correct: *Load (N) gain=10 N/V, Position(mm) gain=0.5 mm/V, LVDT(mm) gain= 0.2 mm/V, Freq=5Hz*. Run data collection and ensure that it is recording accurate values.
- 1.8. Plug in the power cable for the Temp controller
- 1.9. Make sure BOTH water valves are turned on and are flowing. The master water valve is on the wall by the Hydraulic pump, and the unit valve is on the floor between the MTS810 and the Instron 1332 Mech test units.

## 2. SETTING THE TEMPERATURE CONTROLLER

- 2.1. Make sure the master power toggle switch on back of controller is ON.
- 2.2. Hit the left green button to power ON the controller. Red lights will light up. Ignore these until you are ready to test. Do not press the right green button at this time.
- 2.3. Program in the desired temperature program. Follow directions supplied. Put the program on hold.

***DO NOT HEAT /COOL THE FURNACE AT A RATE FASTER THAN 12C PER MINUTE!***

## 3. PREPARING THE CONTROLLER

- 3.1. Output Conversion
  - 3.1.1. Under OUTPUT, set
    - Position to .5 mm/V,
    - Displacement to .2 mm/V,
    - Load to 10 N/V.

These should be the same values set previously in Labview.

- 3.2. Gain Control

### 3.2.1. Under load SETUP,

- Hit “loop”, “prop” and type in the appropriate gain level. For 1000 $\mu$ m Si, use a value between 26-30.

### 3.3. Load Protection

3.3.1. Set LOAD PROTECT to 10N and turn on.

3.3.2. Set the load MAX LIMIT to 100N.

3.3.3. Set the load MIN LIMIT to -100N.

## 4. LOADING THE 4-POINT BEND FIXTURE

4.1. BE VERY CAREFUL AND GENTLE WHEN HANDING AND ASSEMBLING THE SiC FIXTURE!! IT IS VERY FRAGILE AND COSTS SEVERAL THOUSANDS OF DOLLARS \$\$\$\$ TO REPLACE!!!

4.2. Do not touch the SiC with metal components.

4.3. Load the specimen in the fixture and complete assembly. Follow the instructions in section 3.3.1 of INSTRON Ceramic Testing System Operator Manual

4.4. Carefully align the fixture so that the specimen is centered with respect to 1cm wide groove (so it can bend unrestricted). Make sure the 4 points of contact are centered relative to each other.

4.5. Raise the LVDT to be in contact with the underside of the specimen, and bring it to read  $\sim 0.95$ mm

## 5. SUPPRESS READOUTS AND OFFSET OUTPUTS TO ZERO.

5.1. Using the actuator buttons ( $\Delta$  and  $\Delta\Delta$ ) move the 4-point bend fixture upward until just before it contacts the upper pushrod. This is the position zero point.

5.1.1. For position,

- hit SETUP and “suppress”,
- hit the middle button which corresponds to the suppression value

(shown in mm for position and displacement, and N for load),

- type in the current value for position displayed in the upper display,
- and hit the on/off button to turn suppression on.
- the displayed value for position should now read near zero with a “Δ” shown before the units (signifying suppressed mode).
- hit OUTPUTS, POS’N,
- hit the 2<sup>nd</sup> button from the right which corresponds to the output offset (in mm for position and displacement and in N for load).
- Type in the same value as you put in for suppression and hit enter. Hit RETURN.
- The value on the computer Labview display should now read near zero as well.

Repeat the process for load as well (displacement can be done too, if desired).

- 5.2. Move actuator down to leave at least a 4mm gap between the upper pushrod and the 4-point bend fixture.
- 5.3. Slowly close the furnace door-halves and make sure it is centered with respect to the upper pushrod. Latch the two latches in the front and the two in the back.

## 6. BEGINNING THE TEST SEQUENCE

- 6.1. Press the right green button on the temp controller. The red lights should go out and your temp program should begin running.
- 6.2. Once at temperature, press hold ( > | | ) to maintain the desired temperature. Wait 15 minutes before proceeding with the test.
- 6.3. Ensure that LOAD PROTECT is on. With your eyes on the real-time load in the upper display window of the Instron 8500+, slowly raise the actuator by

tapping the “slow” up button (  $\Delta$  ). As soon as the fixture contacts the upper actuator (determined by a quick shift in the load display) STOP.

6.4. Turn off LOAD PROTECT. Go into load control by hitting LOAD, then IMMED. The load should hold close to the initial load. If the load fluctuates sharply, return to position control by hitting, POSITION, IMMED. Then turn LOAD PROTECT back on. This fluctuation is usually a result of an improperly set gain. Check the gain value. If it is up near 26 where it should be, then try reducing it by a point or two and repeating the above process.

6.5. Set the load WAVEFORM to:

LOADshape	$\Delta$ load	1.00
ramps S-RAMP	N	N/sec

where  $\Delta$ load is the desired creep load minus the current applied load (shown in the upper display window).

6.6. Begin waveform by pressing “start”. Once the load reaches the programmed level, load control will keep it there until additional input is received.

6.7. The test should be run until either the material fails or the fixture bottoms out (signified by a dramatic reduction in the displacement rate).

## 7. COMPLETING THE TEST

7.1. Hit POSITION then IMMED.

7.2. Turn load control on (the specimen will unload to 10N)

7.3. Move the actuator down several cm with the  $\nabla\nabla$  button. The actuator and hydraulics may now be turned off.

7.4. Press “Stop and Record” on DAQ and save file to detailed filename:

“Si1000x9-800C-Y-2-A” stands for silicon specimen 1000um thick by 9mm wide tested at 800C for YIELD with piston speed = 2um/sec, 1st (A) test of this kind.

7.5. Wait until the temperature is under 400C before opening the furnace to avoid

thermally shocking the SiC fixture and the heating elements.

- 7.6. You may use indirect fan flow to expedite cooling.
- 7.7. Once you have opened the furnace, turn hydraulics and actuator back on. Slowly lower the piston down to lowest position so you have clearance to safely remove SiC fixture. Turn off hydraulics. Rotate the LVDT thumbwheel all the way right to retract the transducer probe safely away.
- 7.8. Once furnace has **completely and safely** cooled, carefully remove the SiC fixture from the lower pushrod wearing insulated gloves.
- 7.9. Remove tested specimen and appropriately serialize and store.

## **8. CLEANING UP THE WORKPLACE**

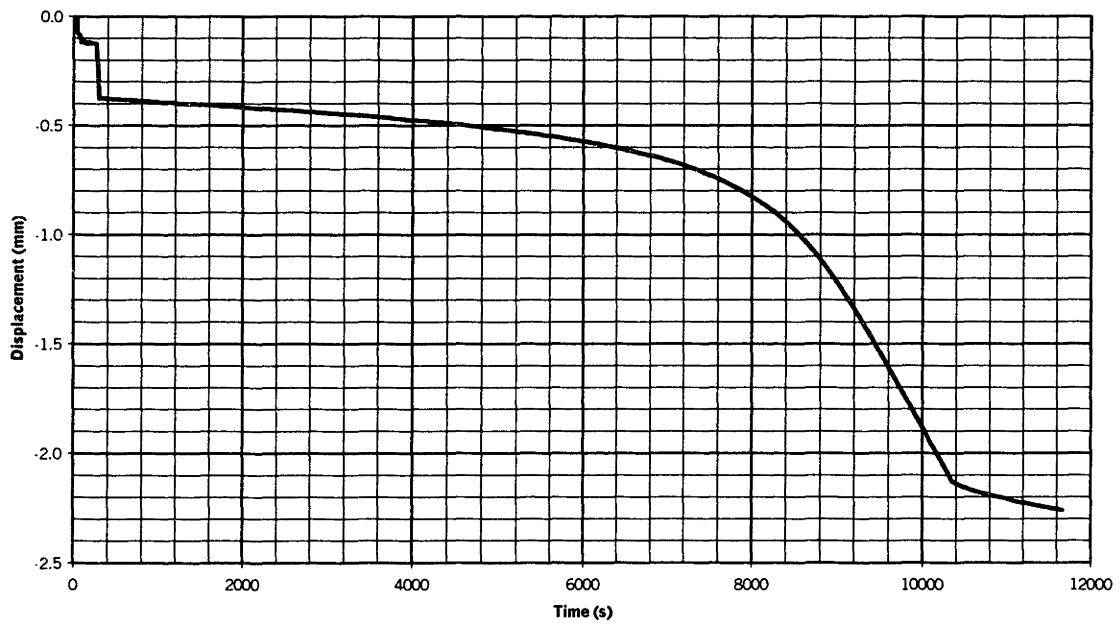
- 8.1. Shut off temp controller power and unplug.
- 8.2. Turn off unit water valve.
- 8.3. Gently wipe down ceramic fixtures with methanol and paper towel.

# APPENDIX A.7 Silicon Creep Test Raw Data - Disp. (mm) vs. Time (s)

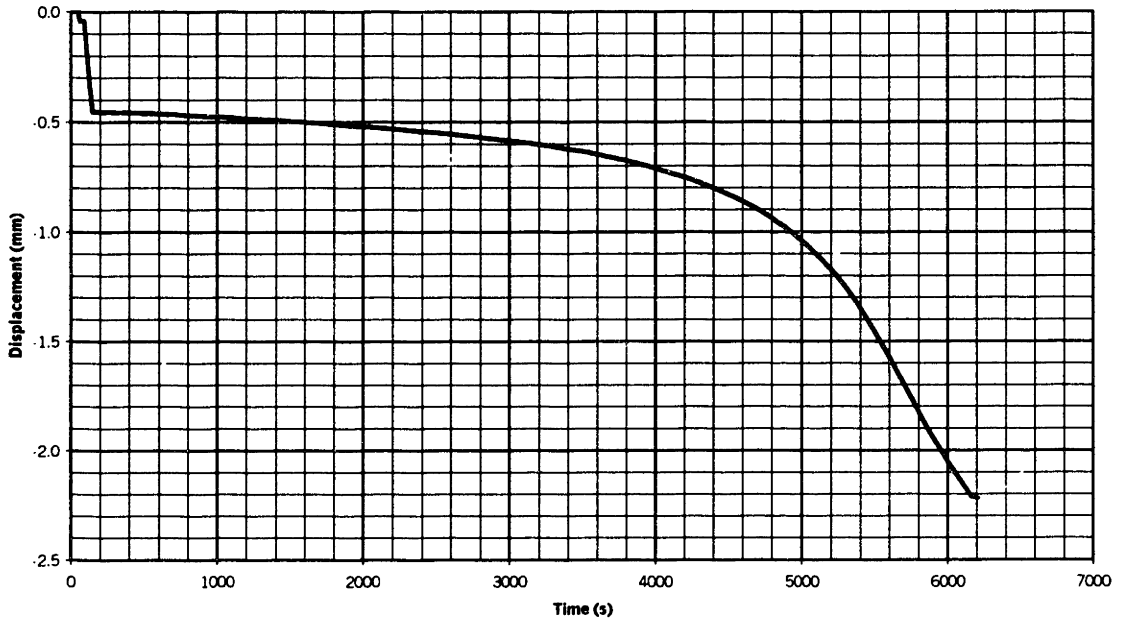
Displacement vs. Time  
Si 1000 $\mu$ m, 9x45+mm, 600°C 30.3N



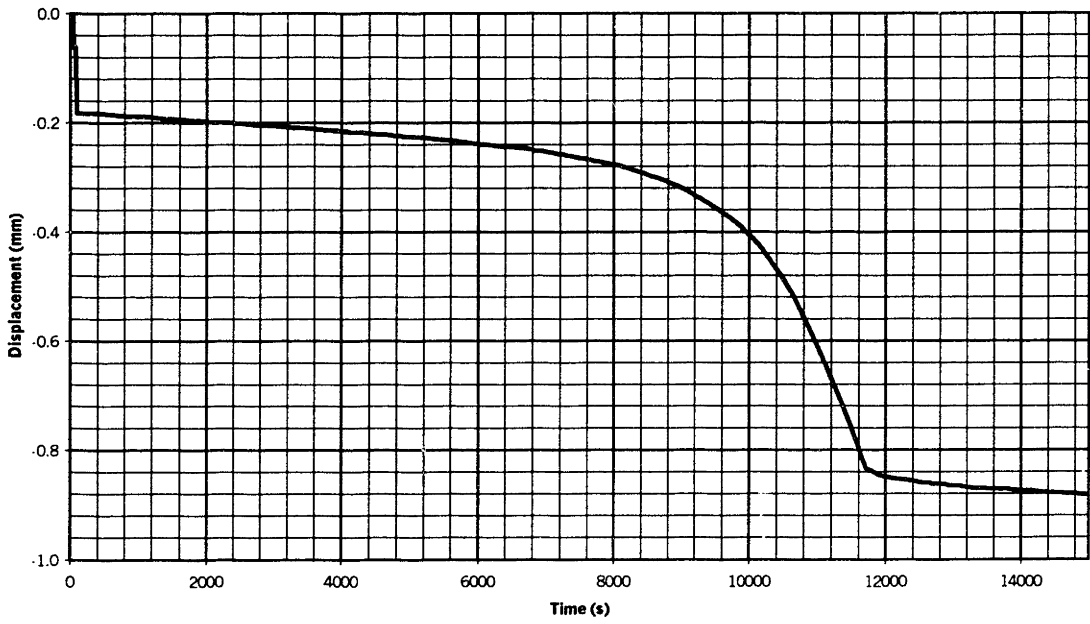
Displacement vs. Time  
Si 1000 $\mu$ m, 9x45+mm, 600°C 45.5N



**Displacement vs. Time**  
**Si 1000 $\mu$ m, 9x45+mm, 600 $^{\circ}$ C 60.4N**

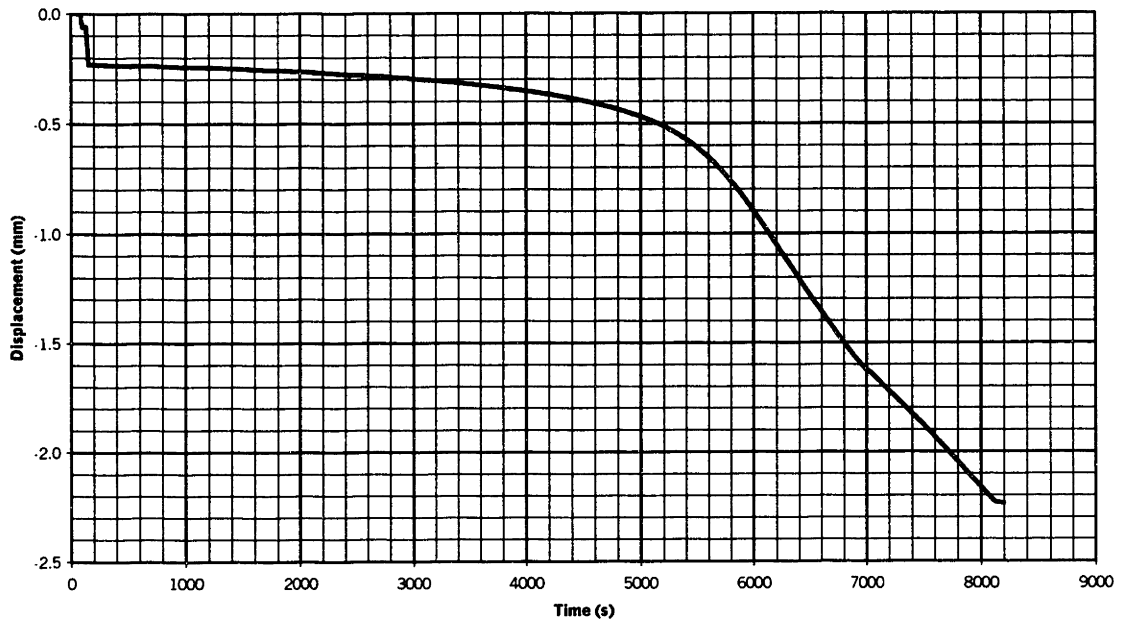


**Displacement vs. Time**  
**Si 1000 $\mu$ m, 9x45+mm, 650 $^{\circ}$ C 24.2N**

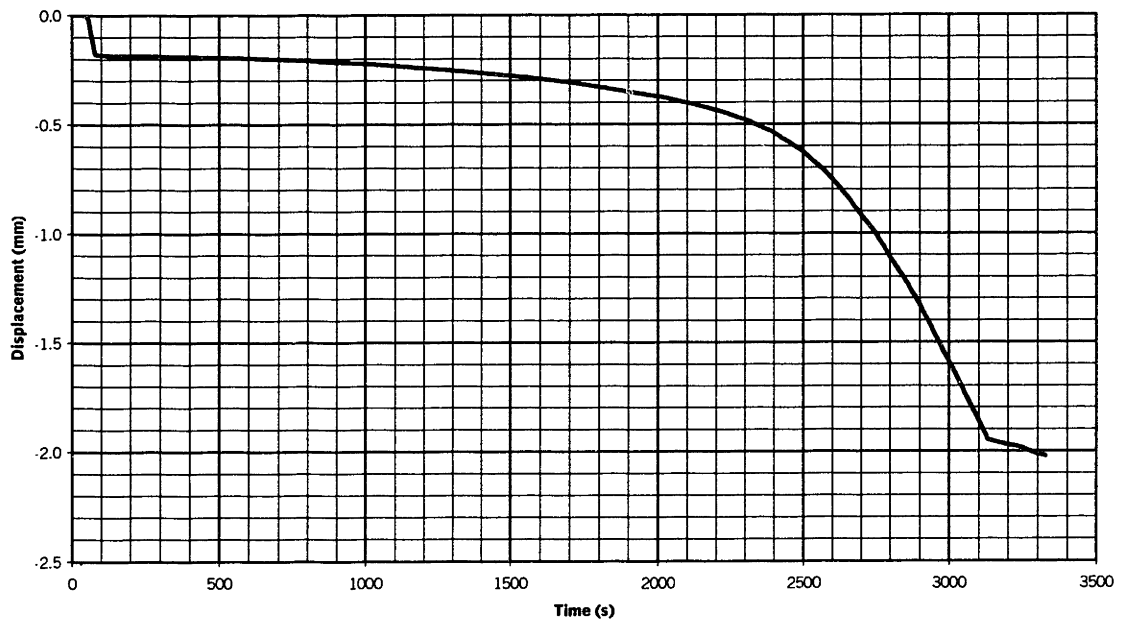




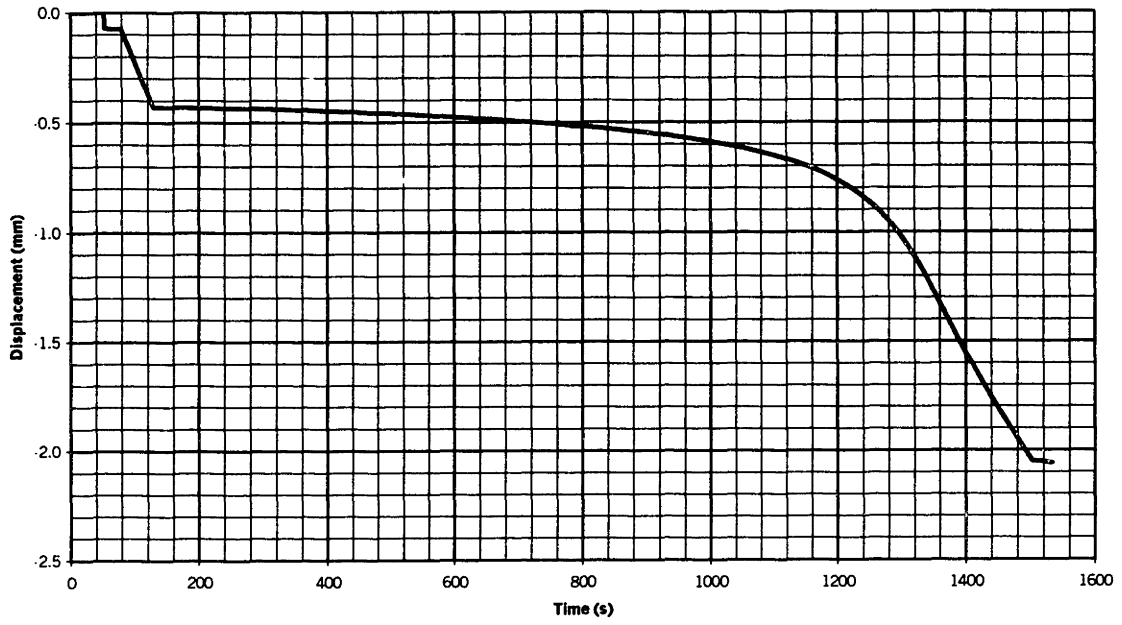
**Displacement vs. Time**  
**Si 1000 $\mu$ m, 9x45+mm, 650 $^{\circ}$ C 30.3N**



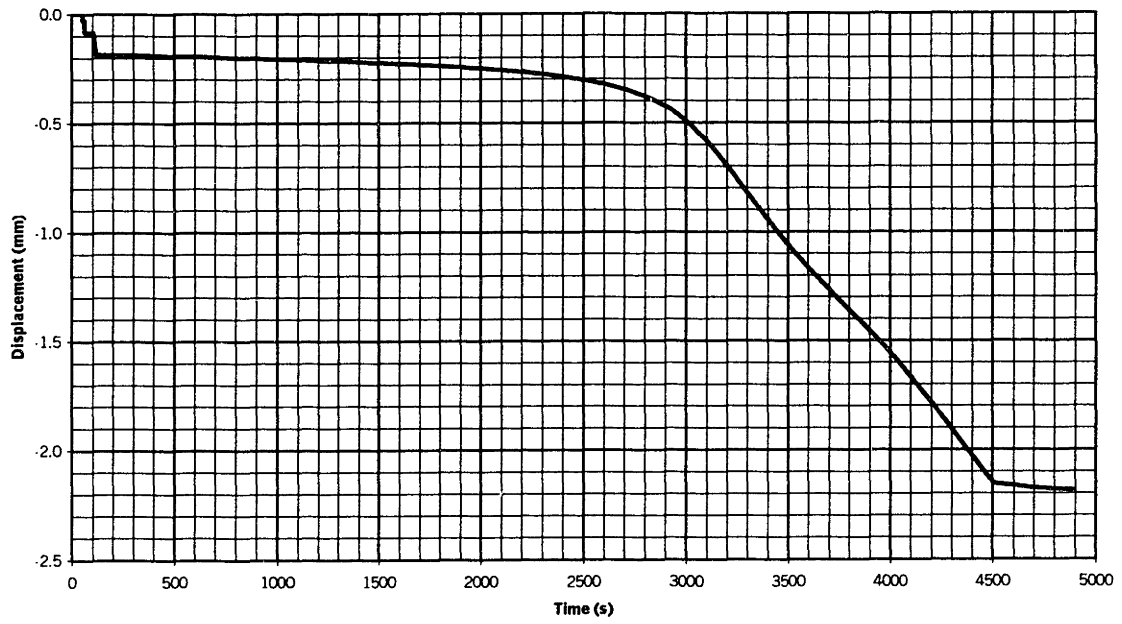
**Displacement vs. Time**  
**Si 1000 $\mu$ m, 9x45+mm, 650 $^{\circ}$ C 45.5N**



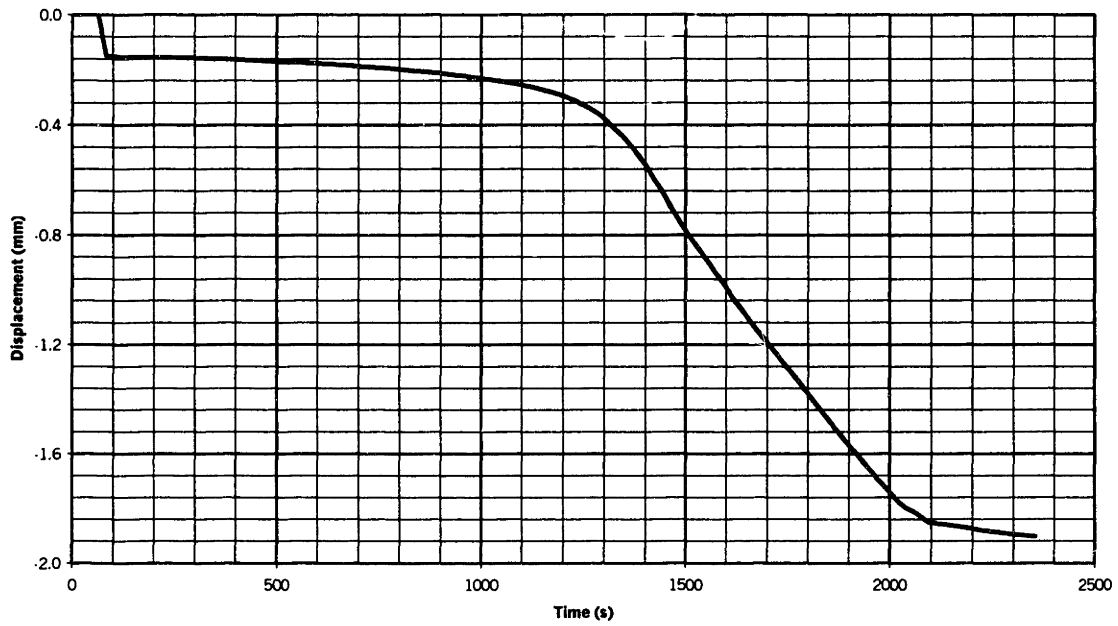
**Displacement vs. Time**  
**Si 1000 $\mu$ m, 9x45+mm, 650°C 60.6N**



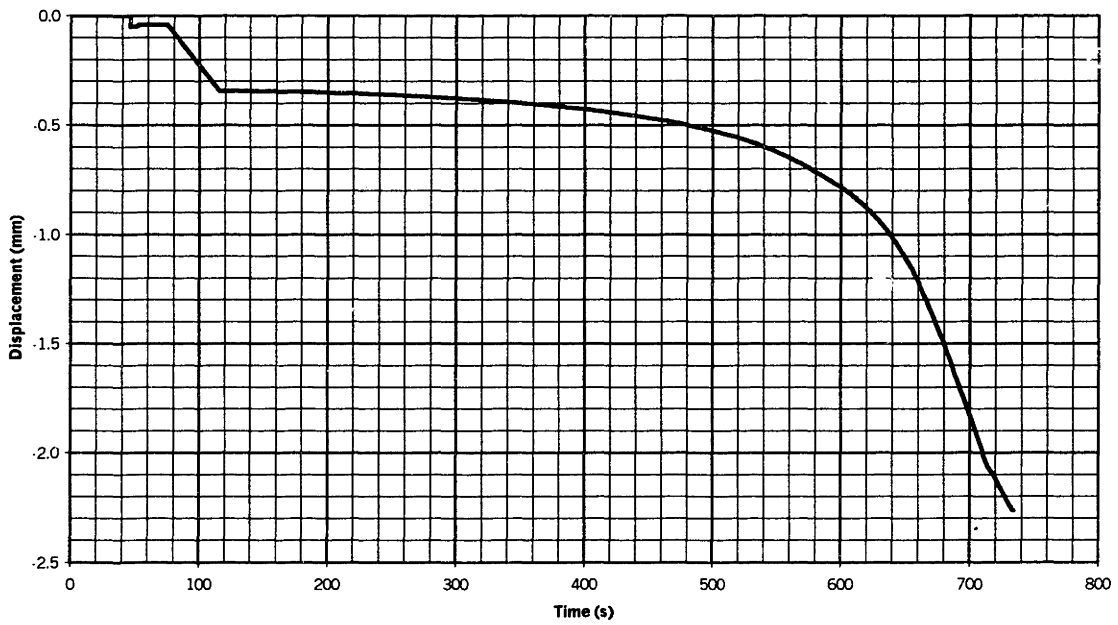
**Displacement vs. Time**  
**Si 1000 $\mu$ m, 9x45+mm, 700°C 24.3N**



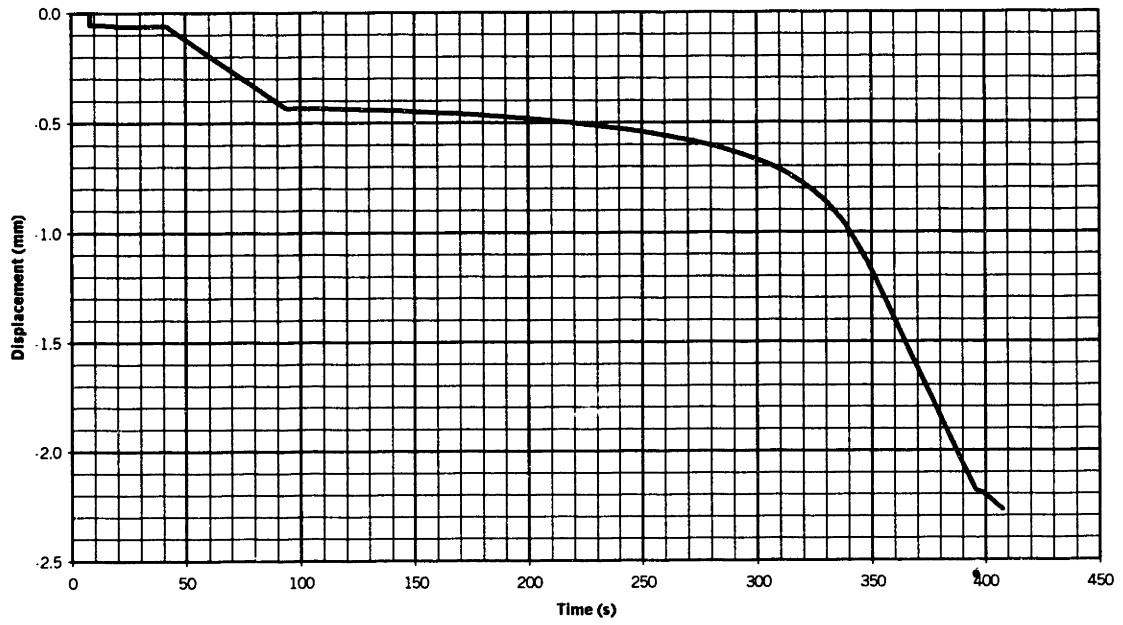
Displacement vs. Time  
Si 1000 $\mu$ m, 9x45+mm, 700 $^{\circ}$ C 30.3N



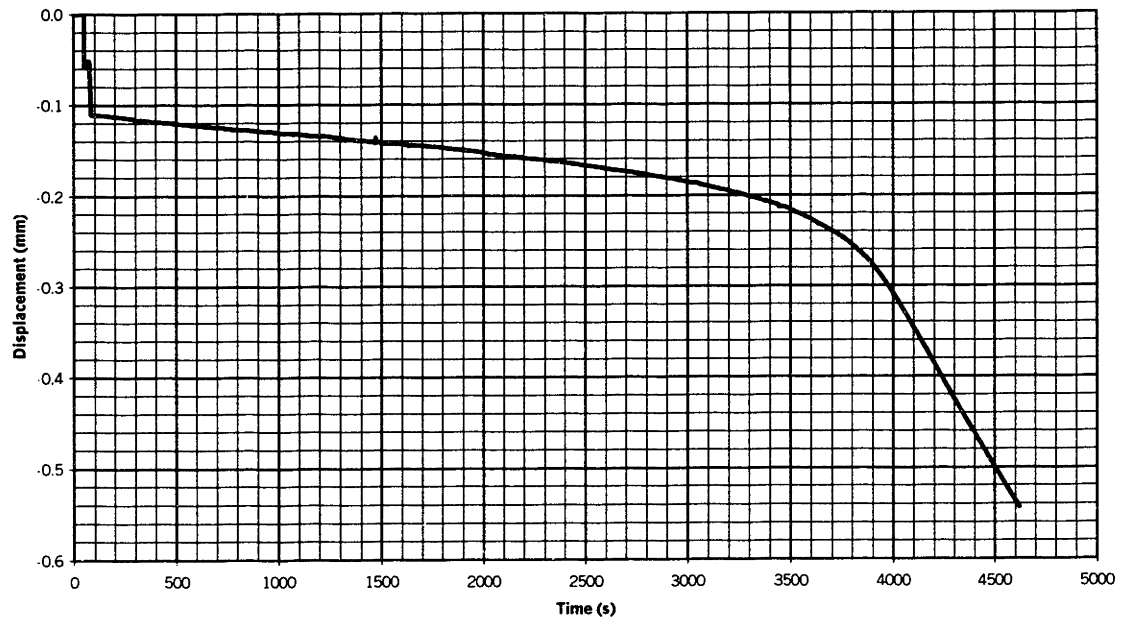
Displacement vs. Time  
Si 1000 $\mu$ m, 9x45+mm, 700 $^{\circ}$ C 45.5N



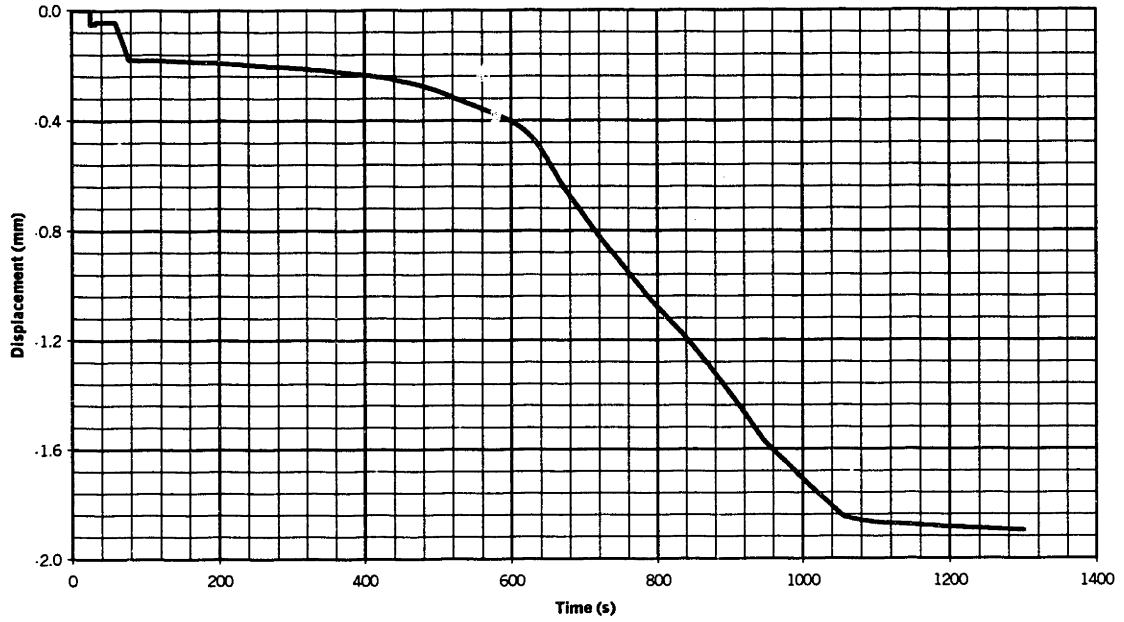
**Displacement vs. Time**  
**Si 1000 $\mu$ m, 9x45+mm, 700°C 60.6N**



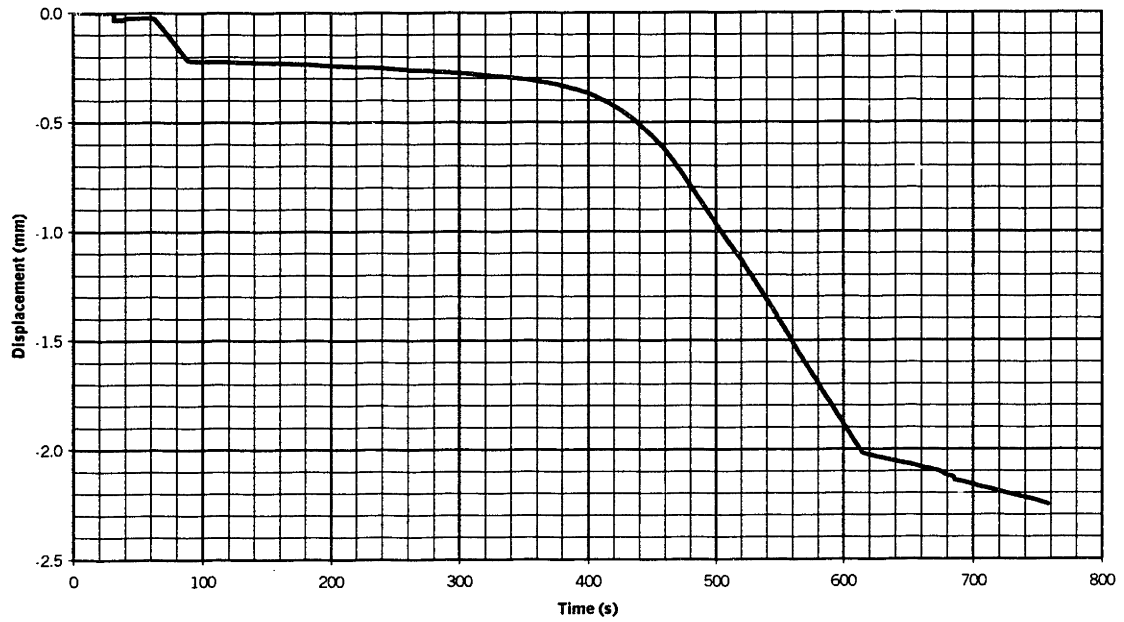
**Displacement vs. Time**  
**Si 1000 $\mu$ m, 9x45+mm, 750°C 15.2N**



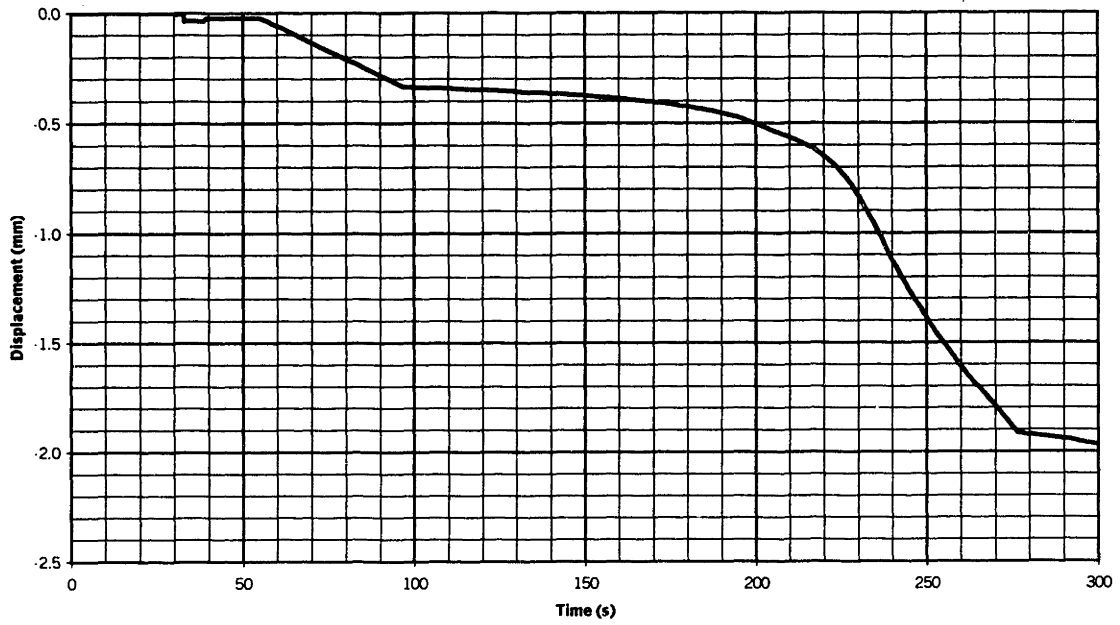
Displacement vs. Time  
Si 1000 $\mu$ m, 9x45+mm, 750°C 24.2N



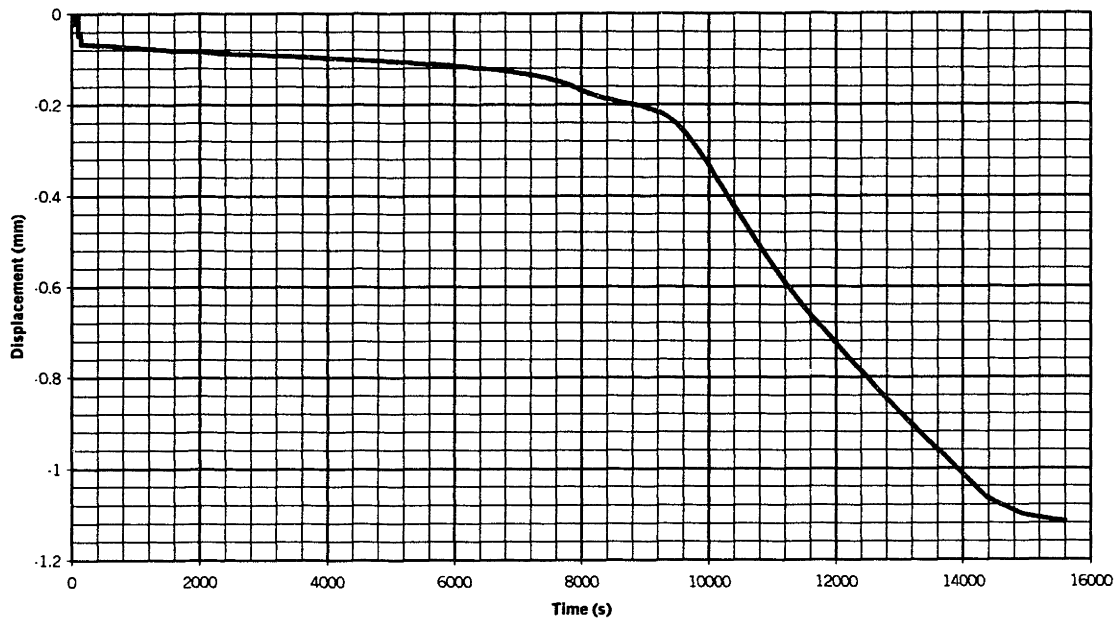
Displacement vs. Time  
Si 1000 $\mu$ m, 9x45+mm, 750°C 30.3N



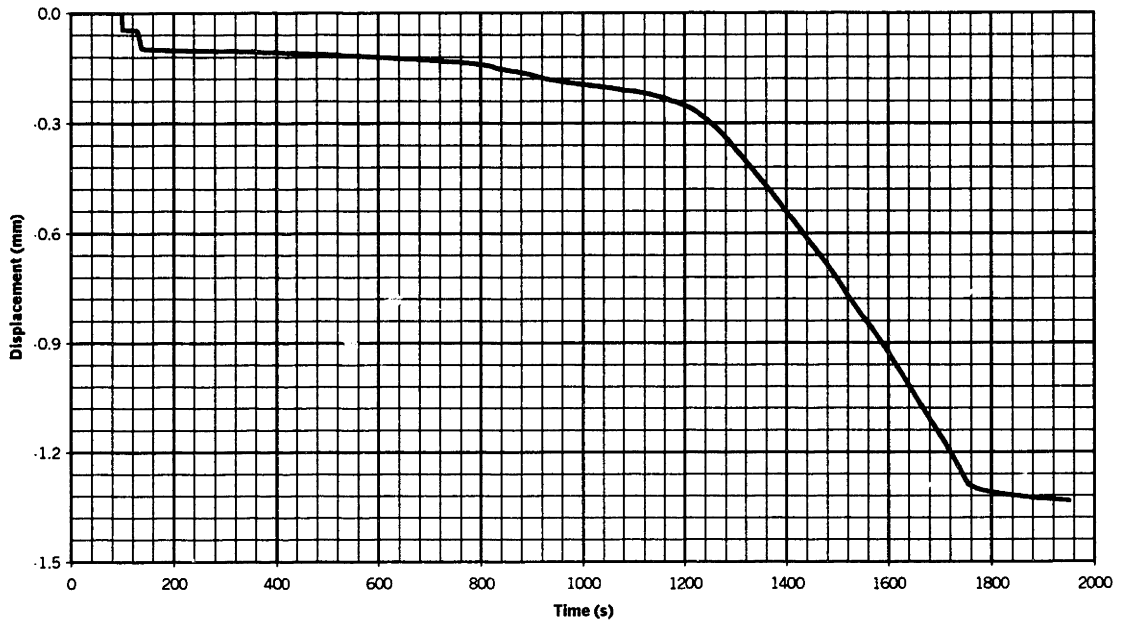
**Displacement vs. Time**  
**Si 1000 $\mu$ m, 9x45+mm, 750°C 45.0N**



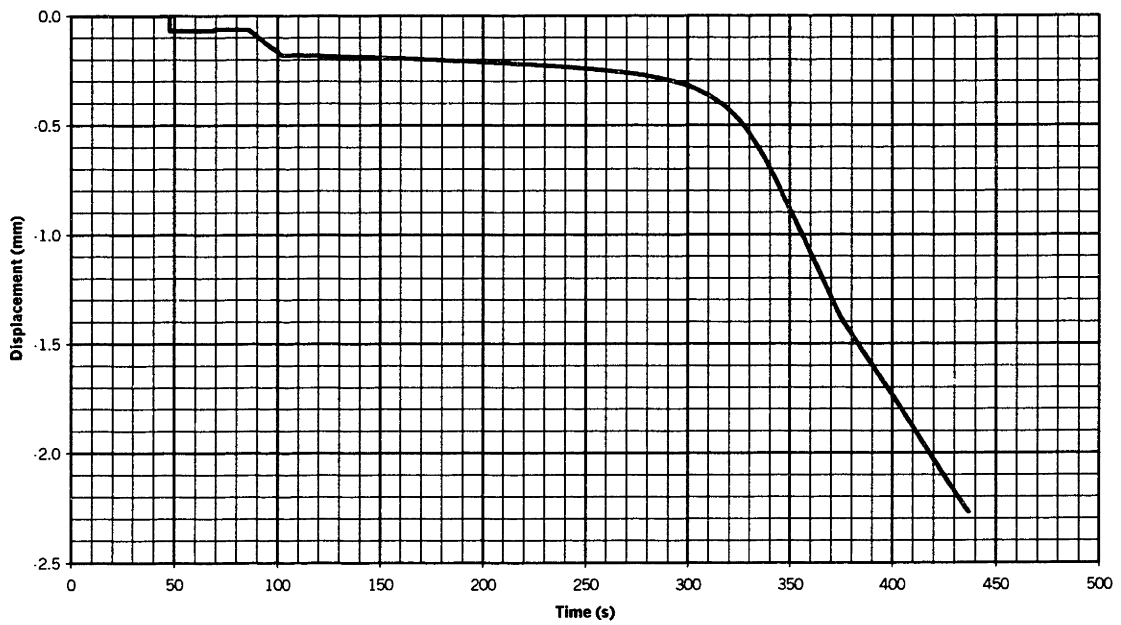
**Displacement vs. Time**  
**Si 1000 $\mu$ m, 9x45+mm, 800°C 9.09N**



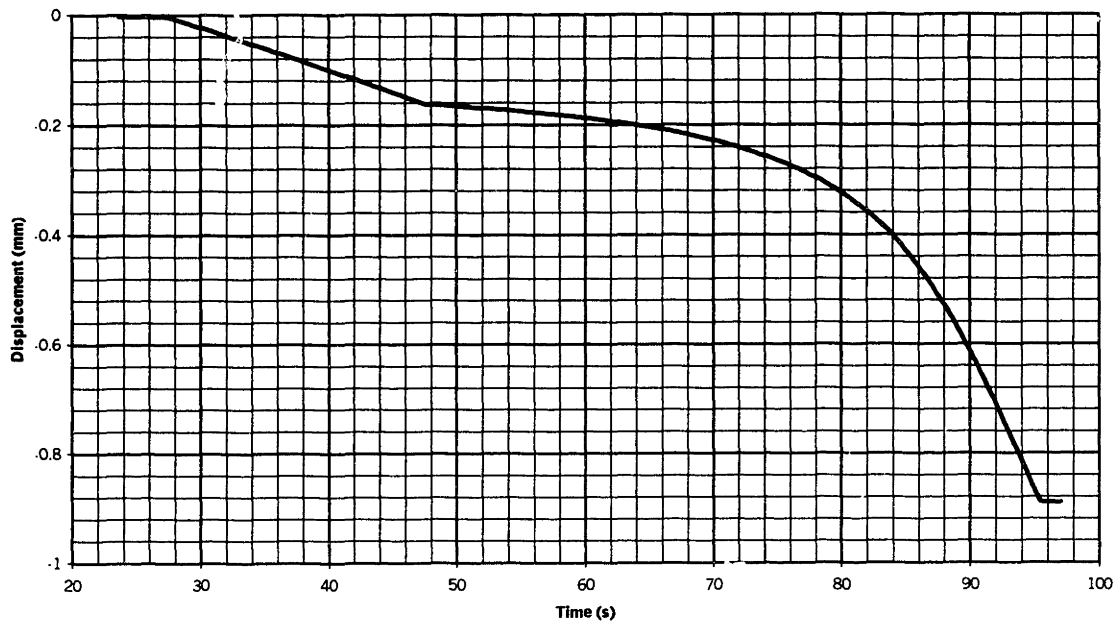
**Displacement vs. Time**  
**Si 1000 $\mu$ m, 9x45+mm, 800 $^{\circ}$ C 15.1N**



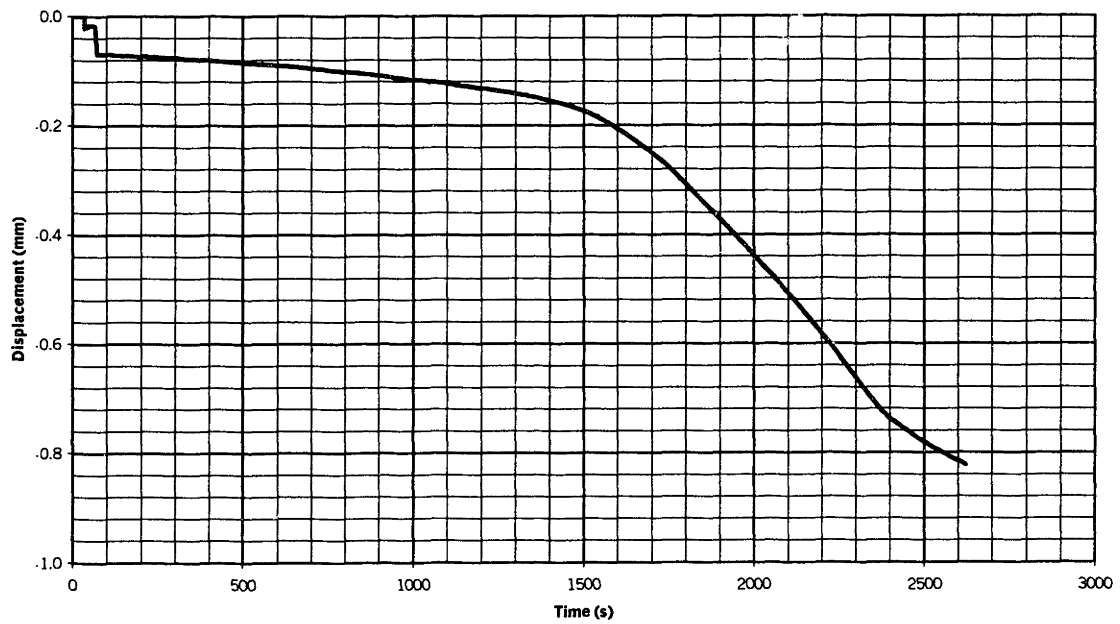
**Displacement vs. Time**  
**Si 1000 $\mu$ m, 9x45+mm, 800 $^{\circ}$ C 24.1N**



**Displacement vs. Time**  
**Si 1000 $\mu$ m, 9x45+mm, 800 $^{\circ}$ C 30.0N**

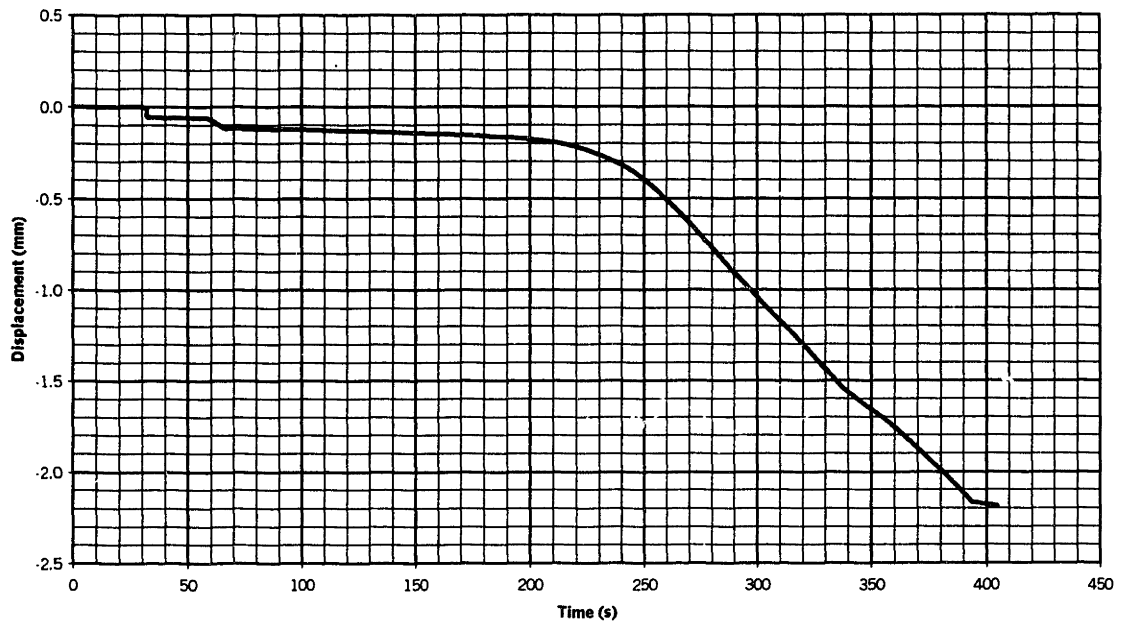


**Displacement vs. Time**  
**Si 1000 $\mu$ m, 9x45+mm, 850 $^{\circ}$ C 9.1N**

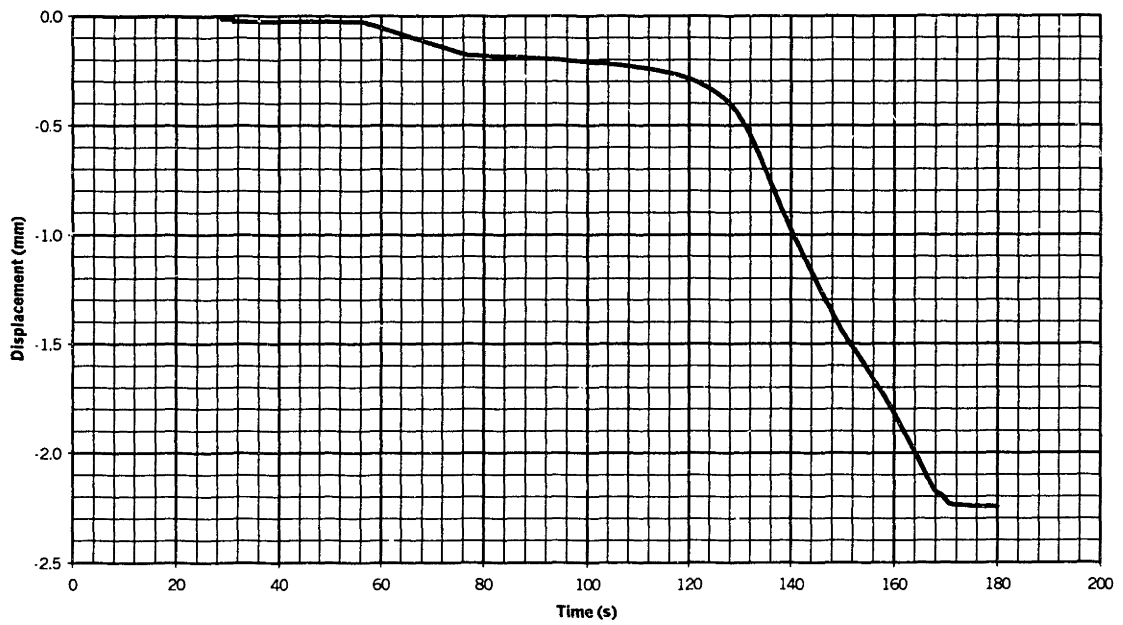




**Displacement vs. Time**  
**Si 1000 $\mu$ m, 9x45+mm, 850 $^{\circ}$ C 15.2N**

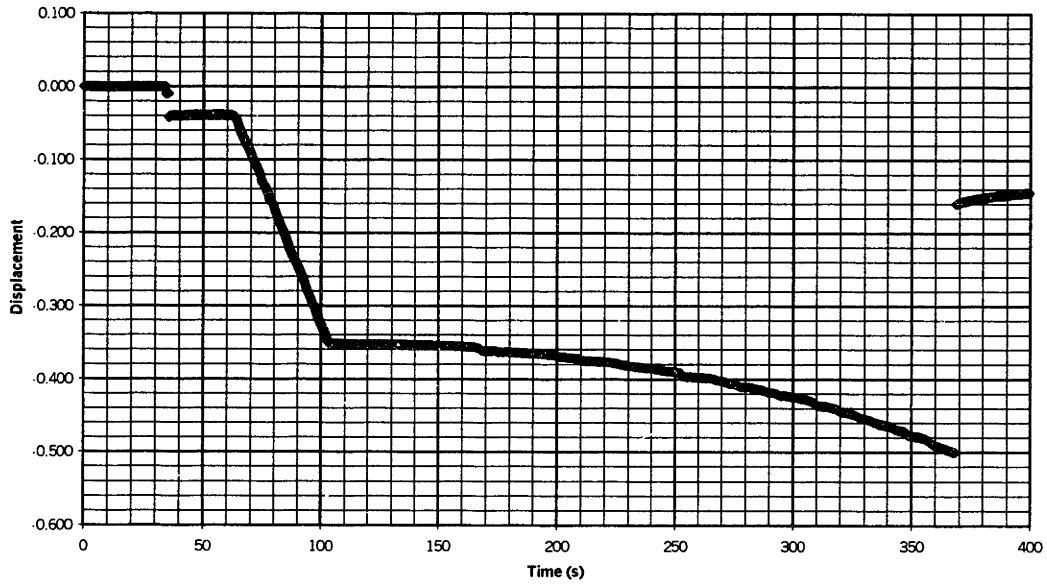


**Displacement vs. Time**  
**Si 1000 $\mu$ m, 9x45+mm, 850 $^{\circ}$ C 24.3N**

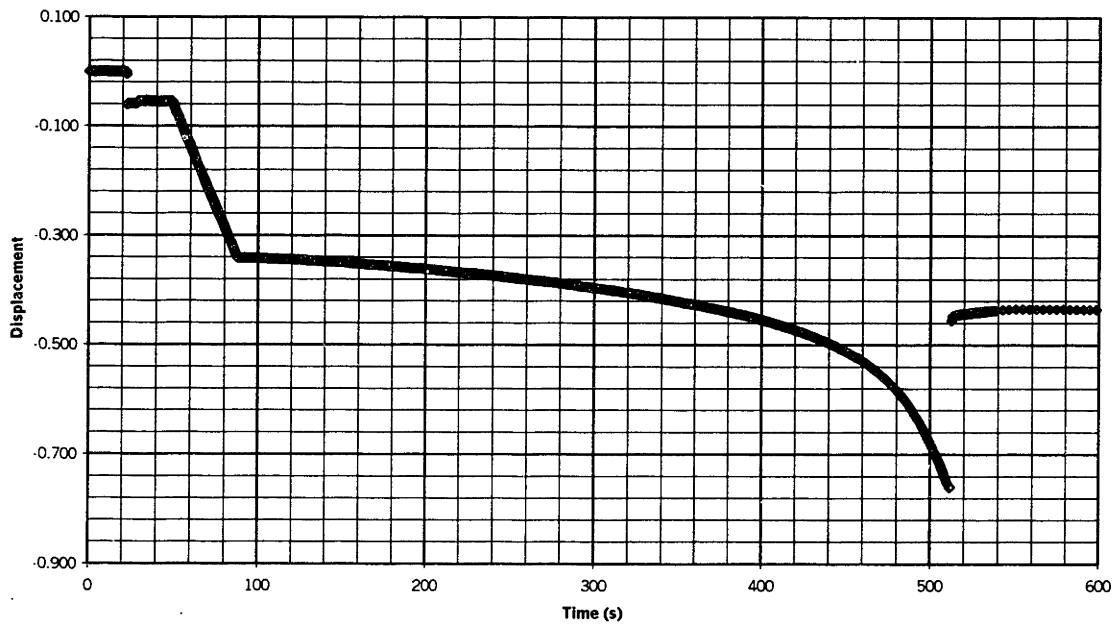


# APPENDIX A.8 Incremental Creep Test Data - Disp. (mm) vs. Time (s)

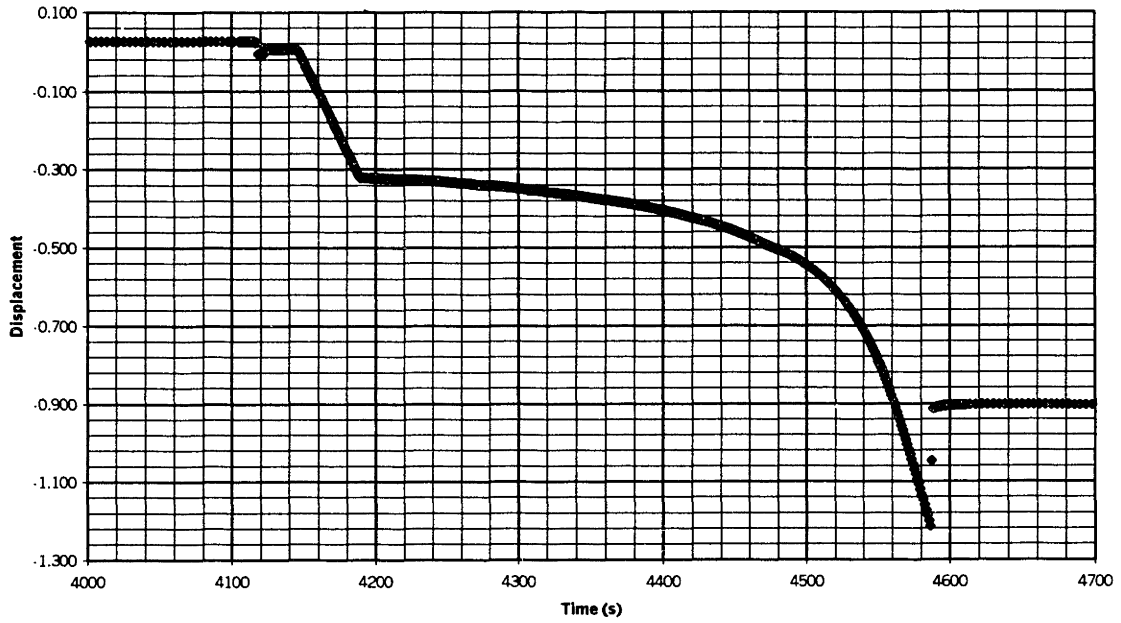
Displacement vs. Time  
Si 1000 $\mu$ m, 9x45+mm, 700°C 45.5N  
STEP1



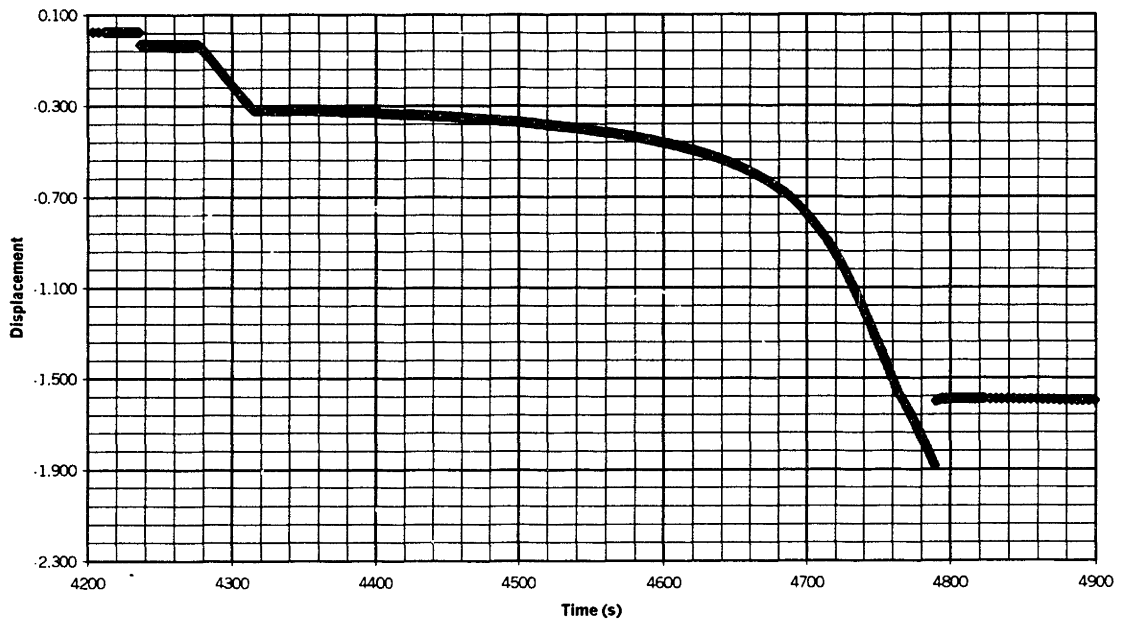
Displacement vs. Time  
Si 1000 $\mu$ m, 9x45+mm, 700°C 45.5N  
STEP2



Displacement vs. Time  
Si 1000 $\mu$ m, 9x45+mm, 700°C 45.5N  
STEP3

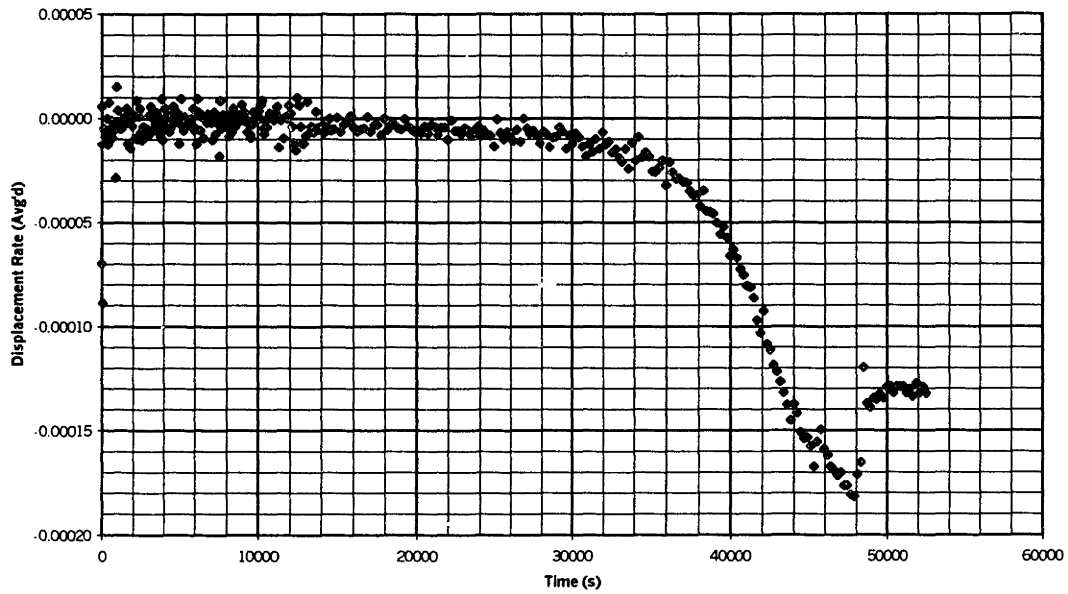


Displacement vs. Time  
Si 1000 $\mu$ m, 9x45+mm, 700°C 45.5N  
STEP4

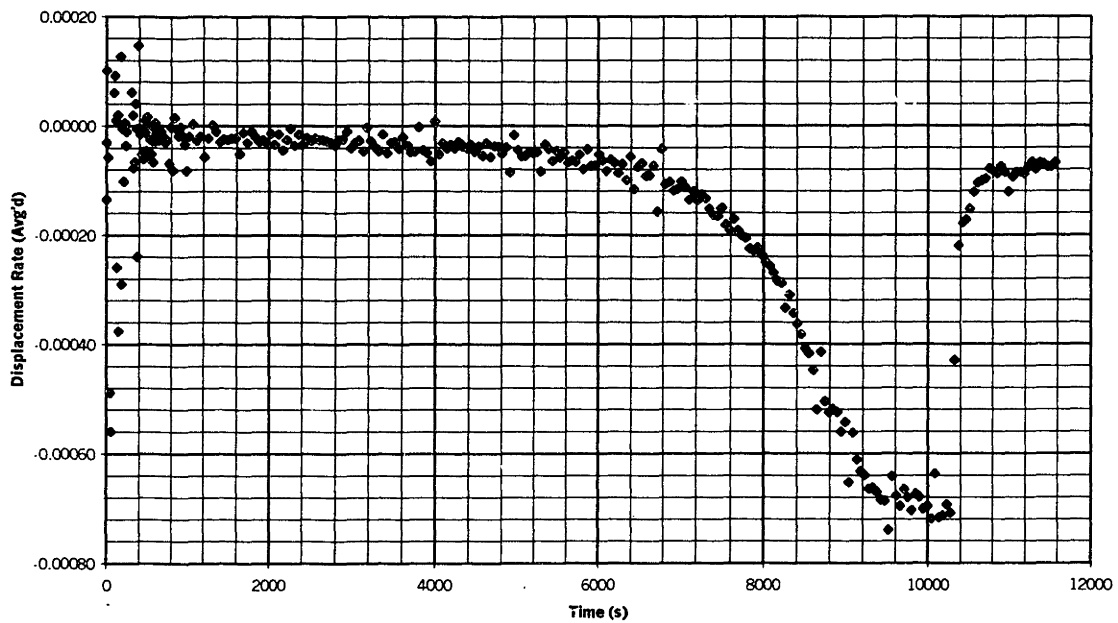


# APPENDIX A.9 Displacement Rate (mm/s) vs. Time (s) Plots

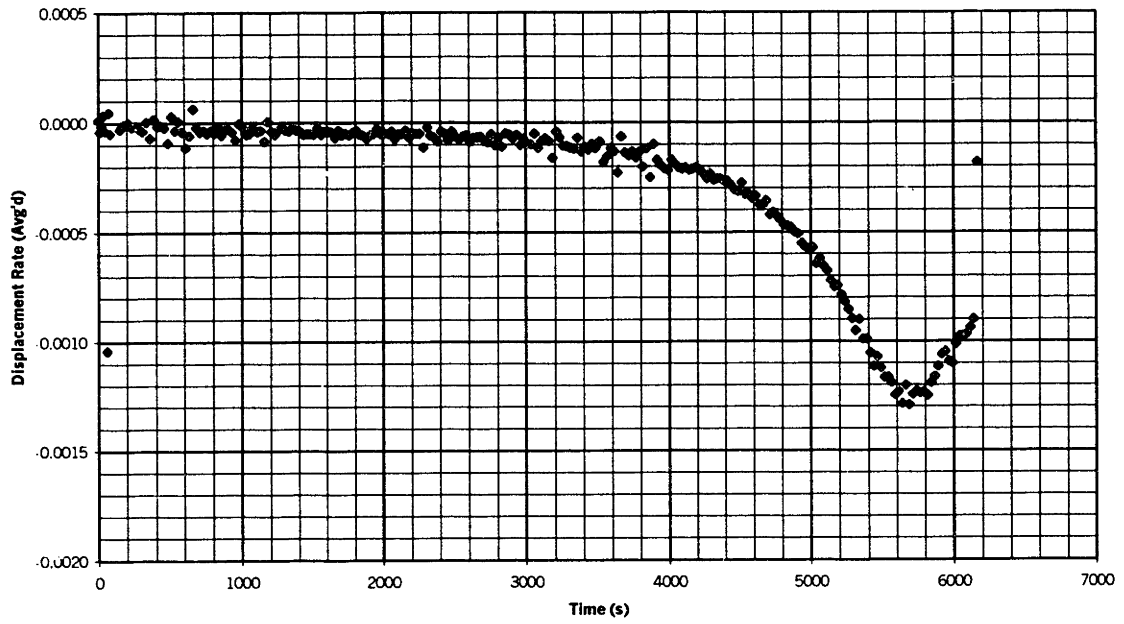
Displacement Rate vs. Time  
Si 1000 $\mu$ m, 9x45+mm, 600°C 30.3N



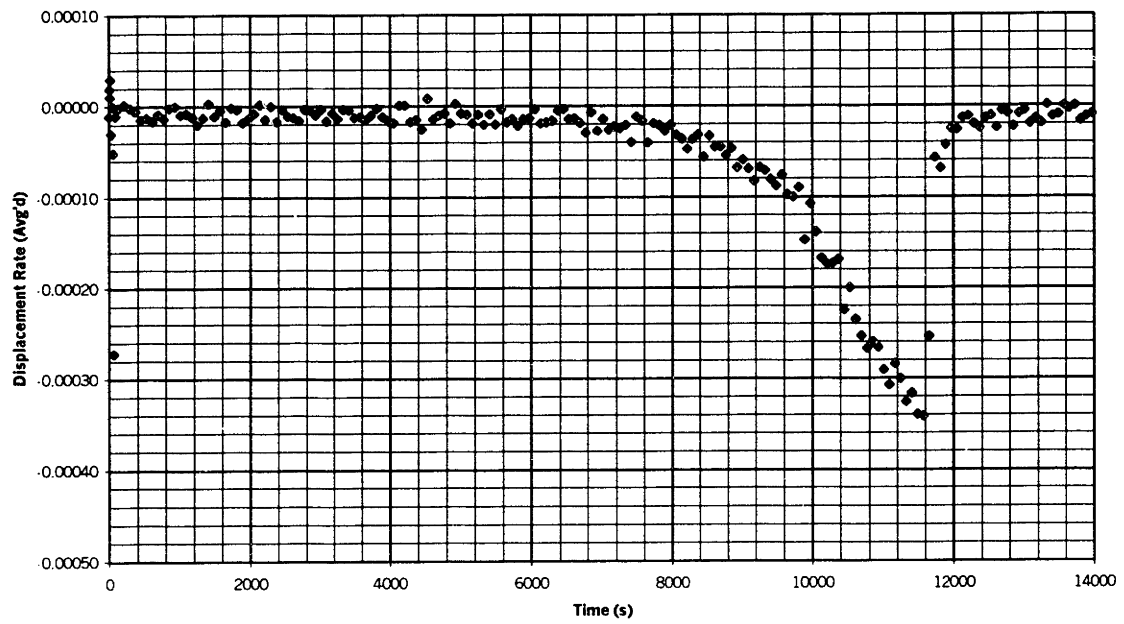
Displacement Rate vs. Time  
Si 1000 $\mu$ m, 9x45+mm, 600°C 45.5N



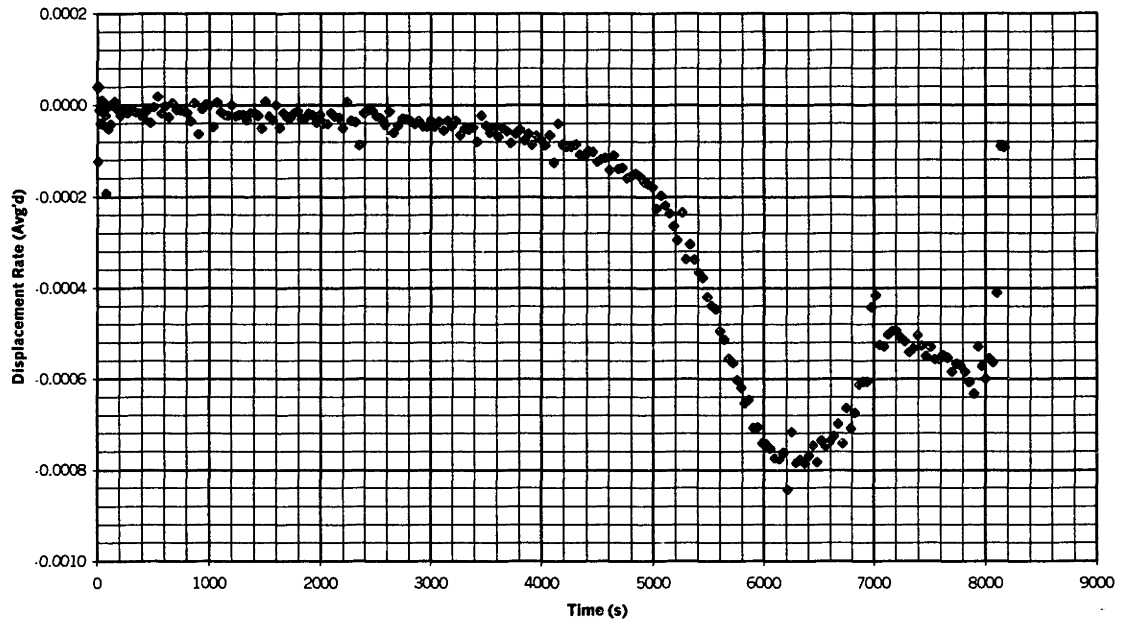
Displacement Rate vs. Time  
Si 1000 $\mu\text{m}$ , 9x45+mm, 600°C 60.4N



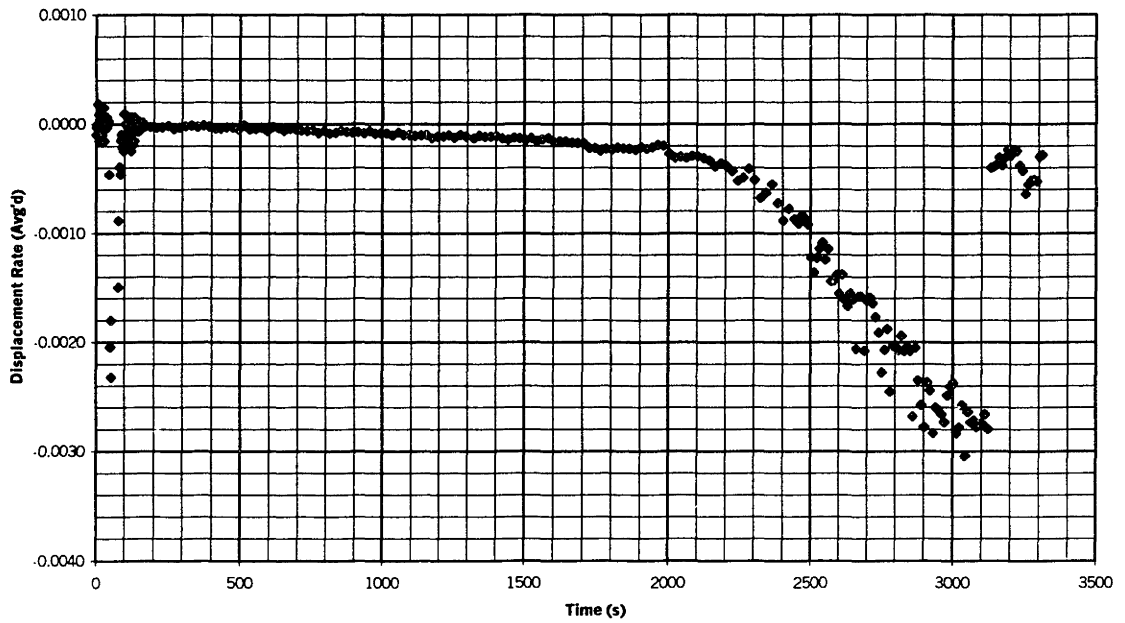
Displacement Rate vs. Time  
Si 1000 $\mu\text{m}$ , 9x45+mm, 650°C 24.2N



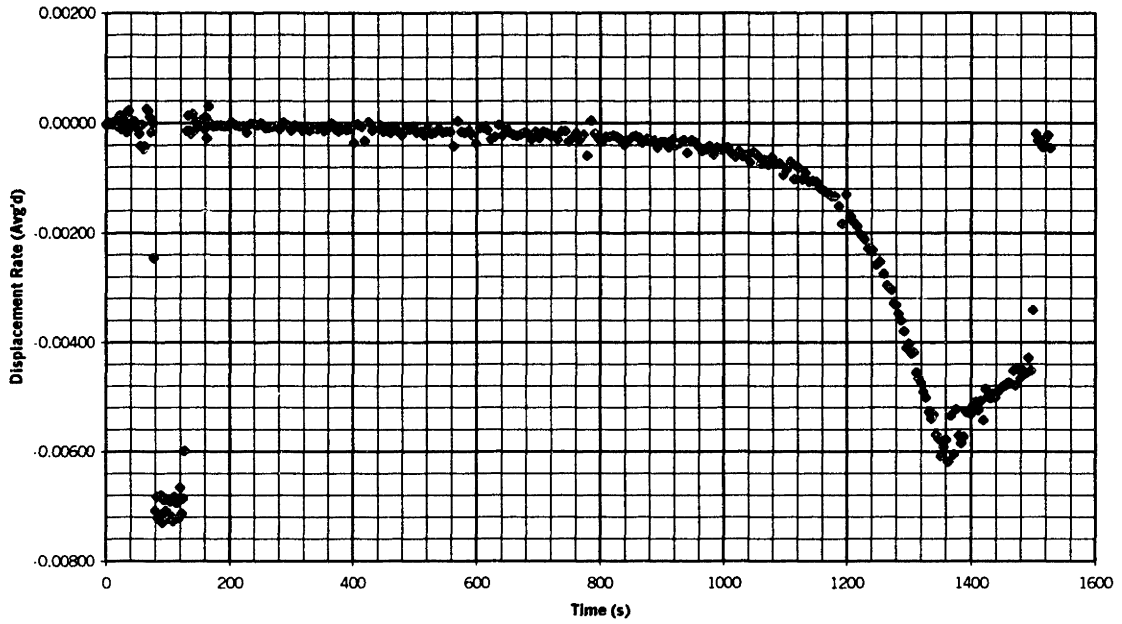
Displacement Rate vs. Time  
Si 1000 $\mu$ m, 9x45+mm, 650 $^{\circ}$ C 30.3N



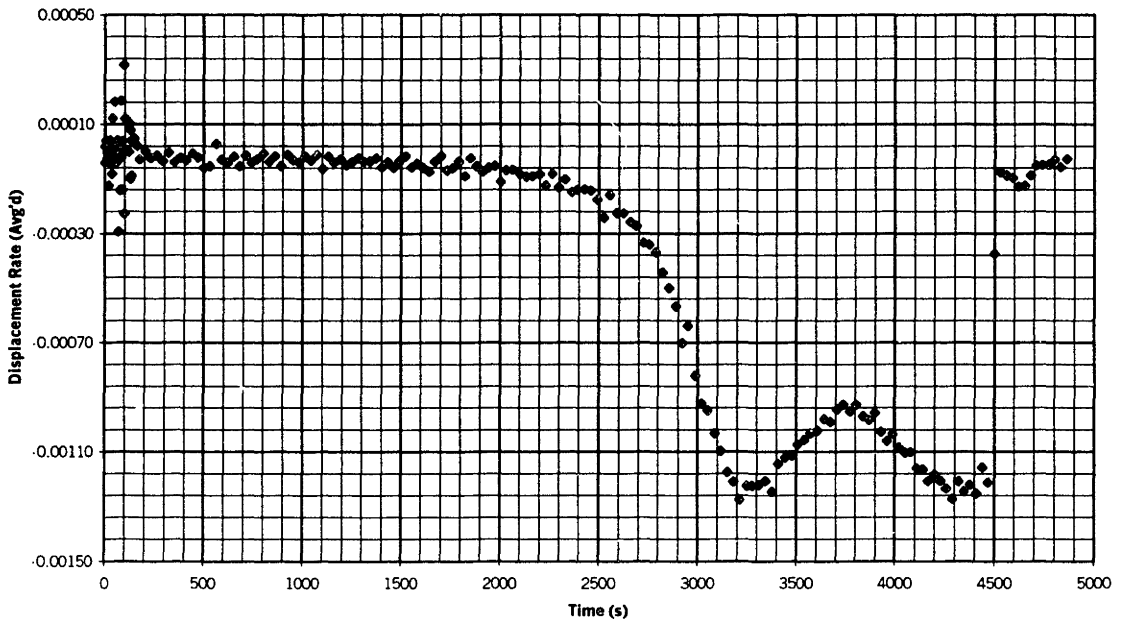
Displacement Rate vs. Time  
Si 1000 $\mu$ m, 9x45+mm, 650 $^{\circ}$ C 45.5N



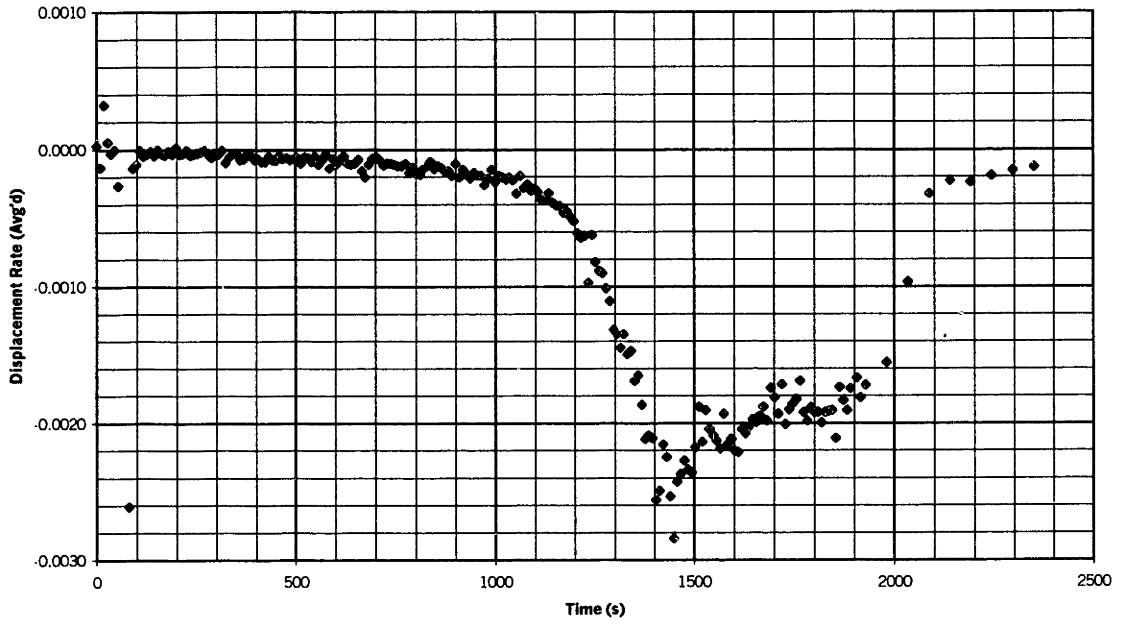
Displacement Rate vs. Time  
Si 1000 $\mu$ m, 9x45+mm, 650°C 60.6N



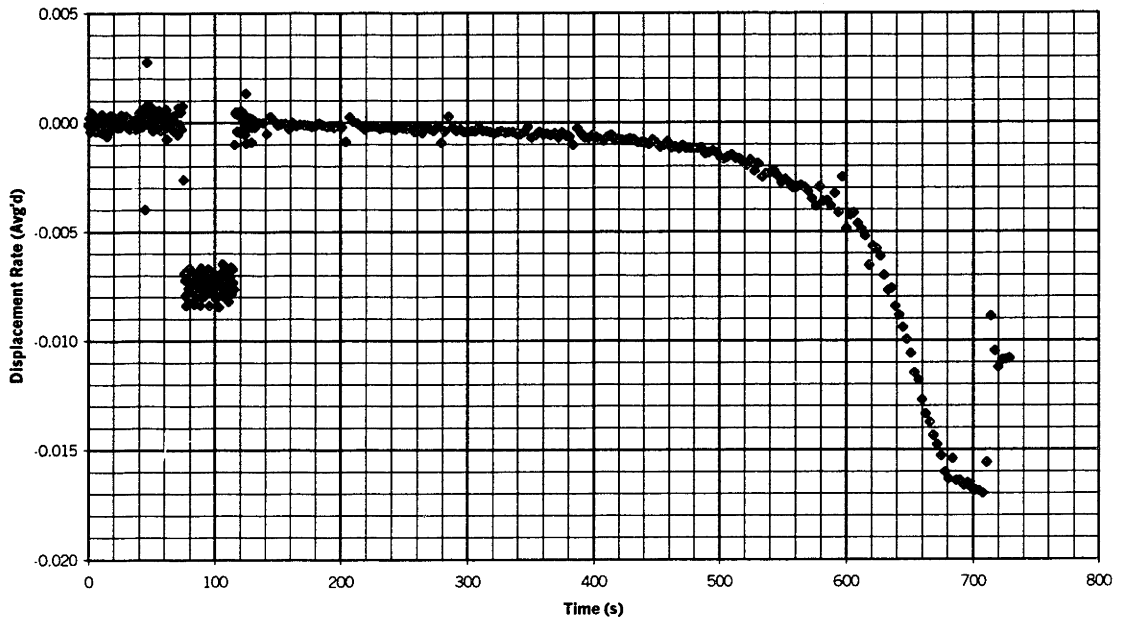
Displacement Rate vs. Time  
Si 1000 $\mu$ m, 9x45+mm, 700°C 24.3N



Displacement Rate vs. Time  
Si 1000 $\mu\text{m}$ , 9x45+mm, 700°C 30.3N

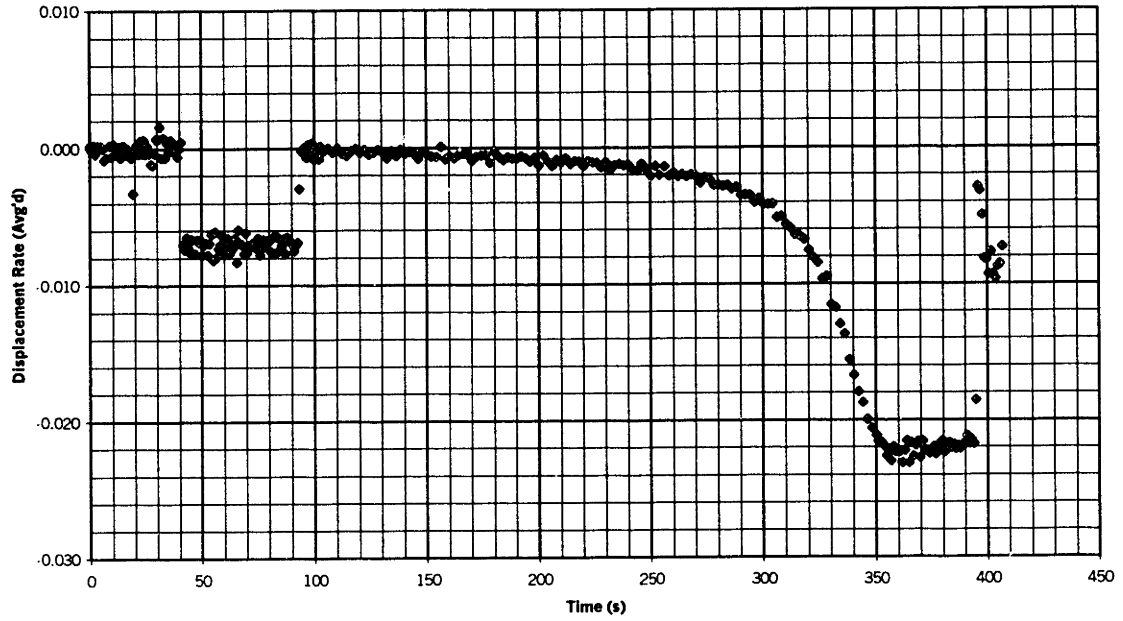


Displacement Rate vs. Time  
Si 1000 $\mu\text{m}$ , 9x45+mm, 700°C 45.5N

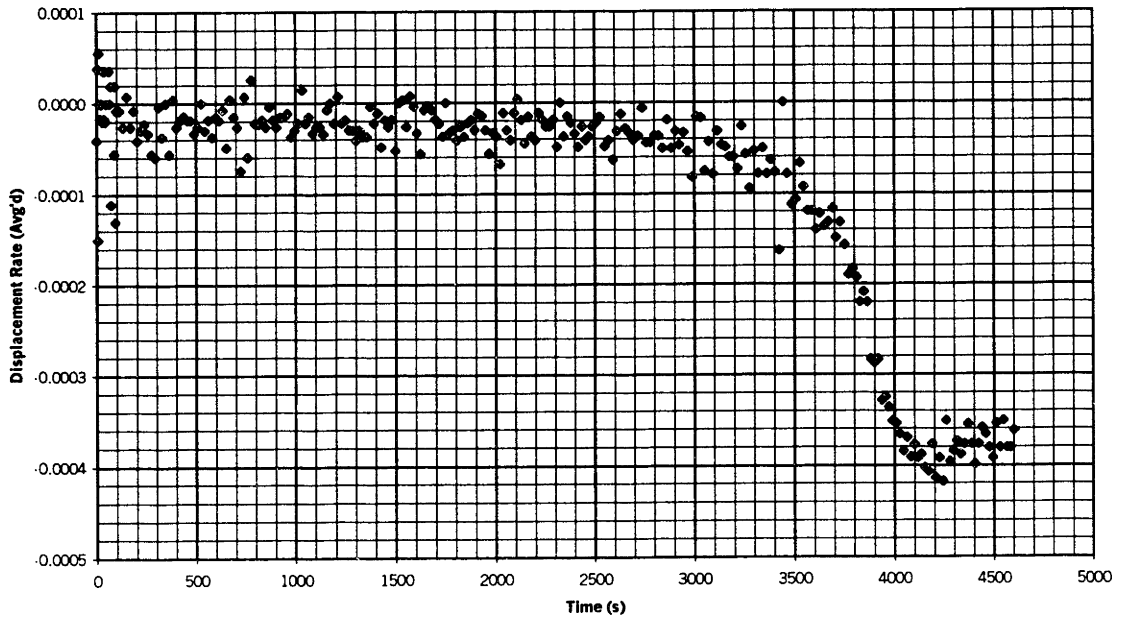




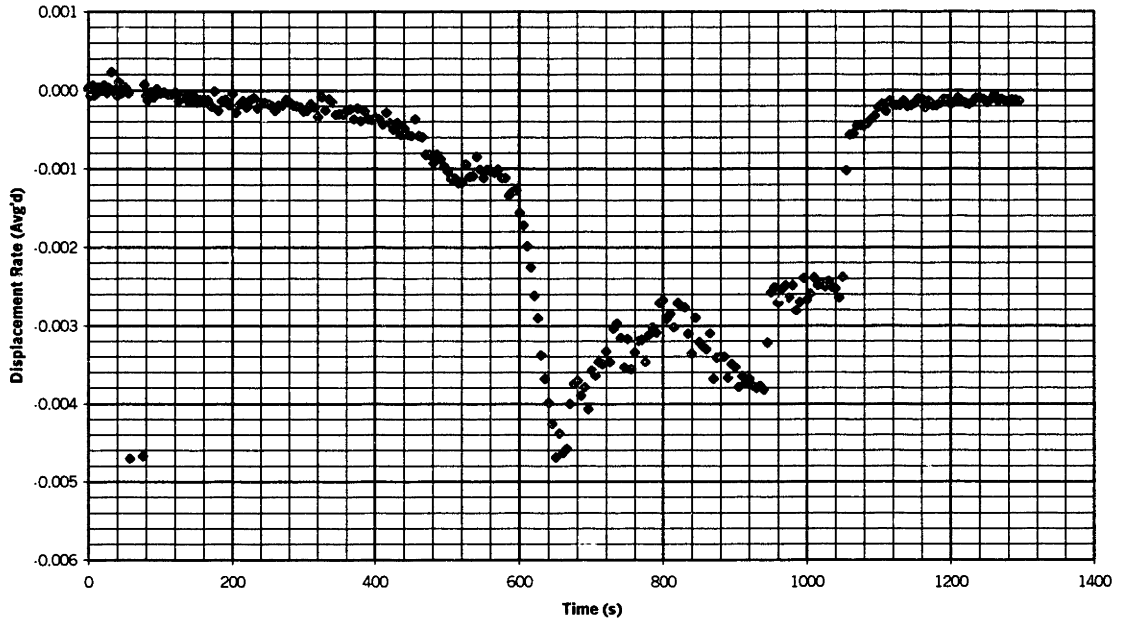
Displacement Rate vs. Time  
Si 1000 $\mu$ m, 9x45+mm, 700°C 60.6N



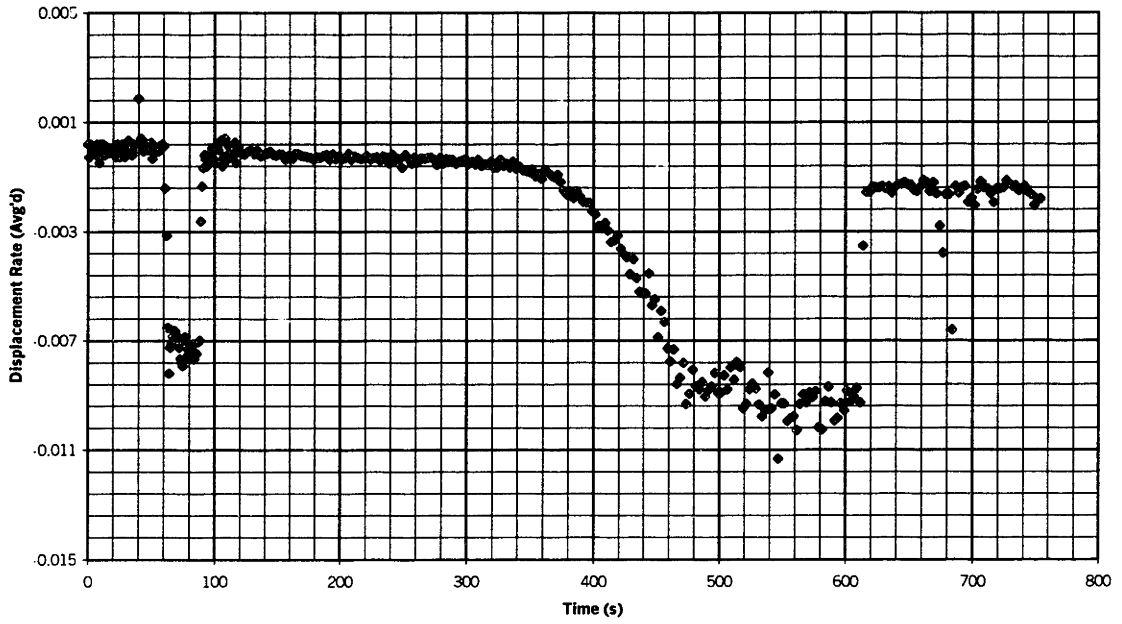
Displacement Rate vs. Time  
Si 1000 $\mu$ m, 9x45+mm, 750°C 15.2N



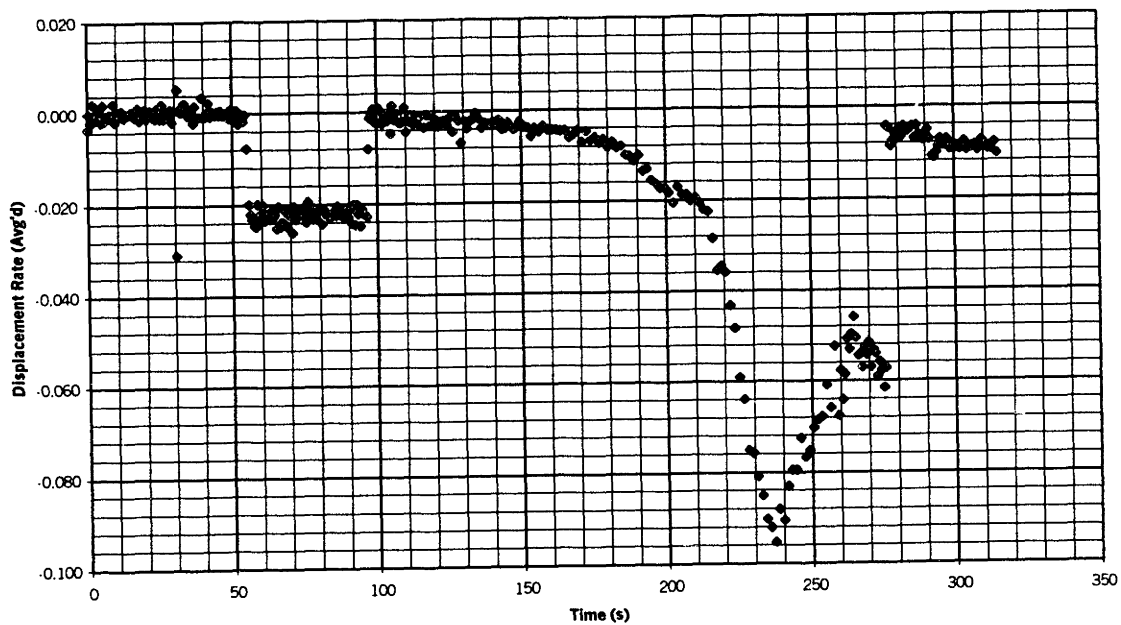
Displacement Rate vs. Time  
Si 1000 $\mu$ m, 9x45+mm, 750 $^{\circ}$ C 24.2N



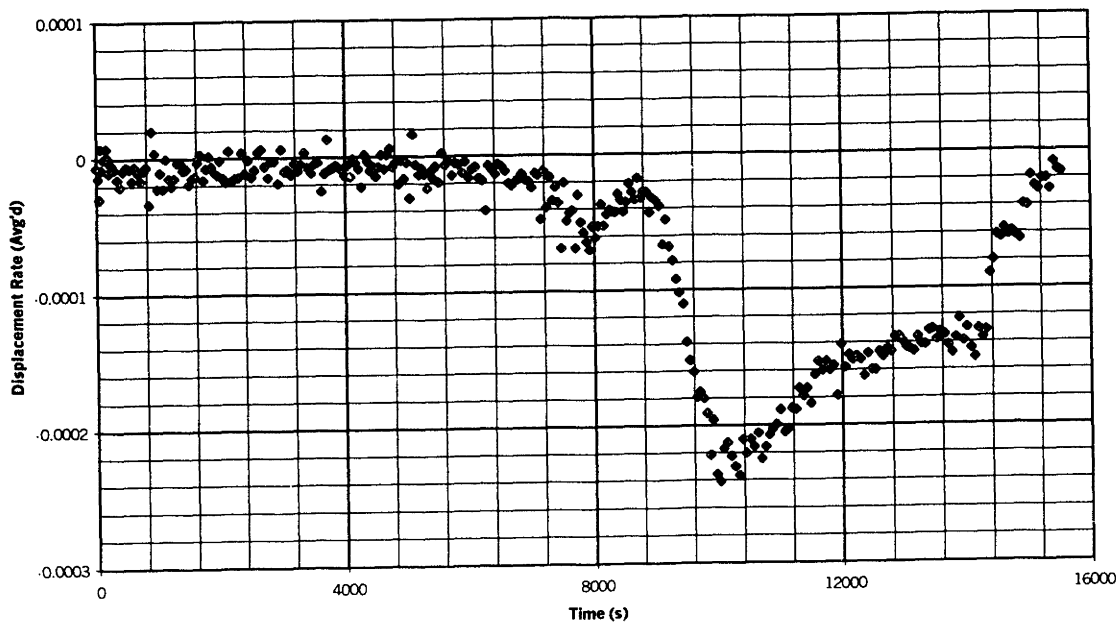
Displacement Rate vs. Time  
Si 1000 $\mu$ m, 9x45+mm, 750 $^{\circ}$ C 30.3N



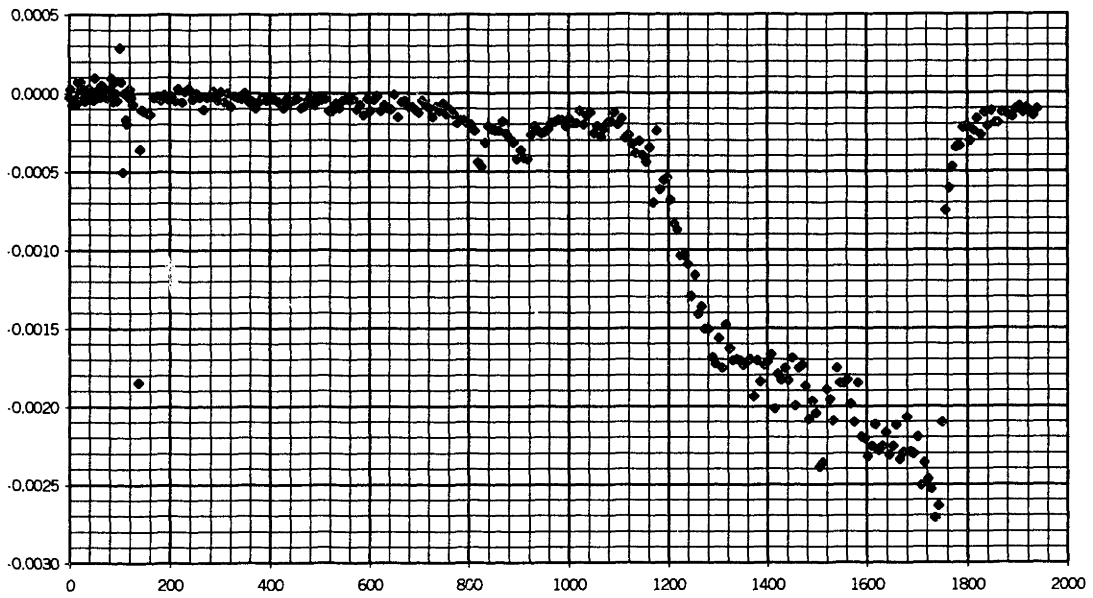
Displacement Rate vs. Time  
Si 1000 $\mu\text{m}$ , 9x45+mm, 750°C 45.0N



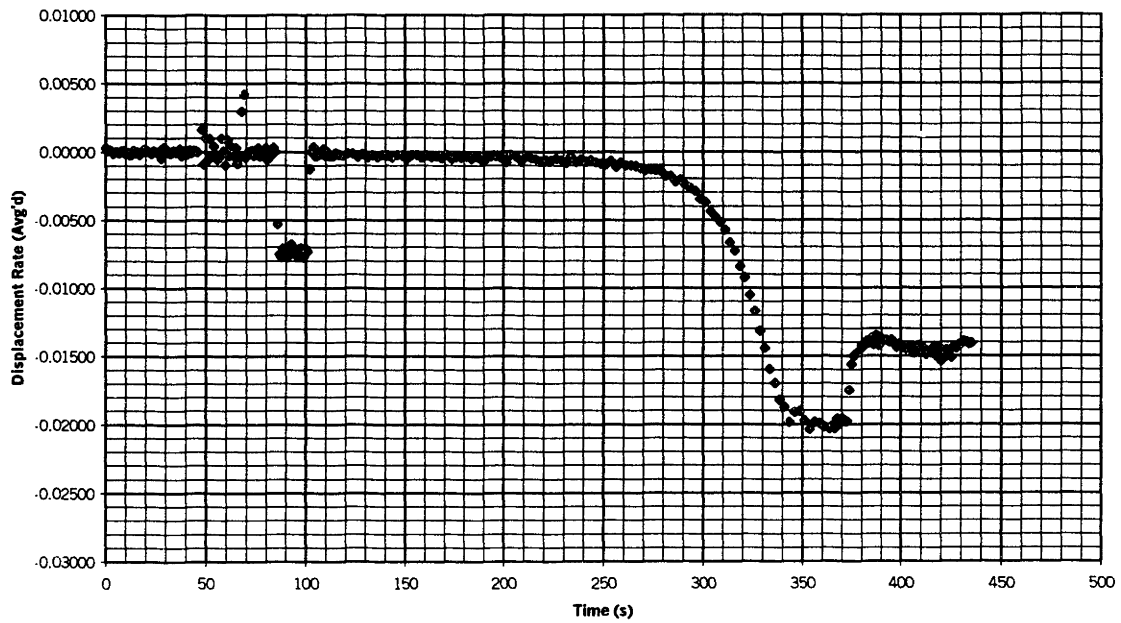
Displacement Rate vs. Time  
Si 1000 $\mu\text{m}$ , 9x45+mm, 800°C 9.09N



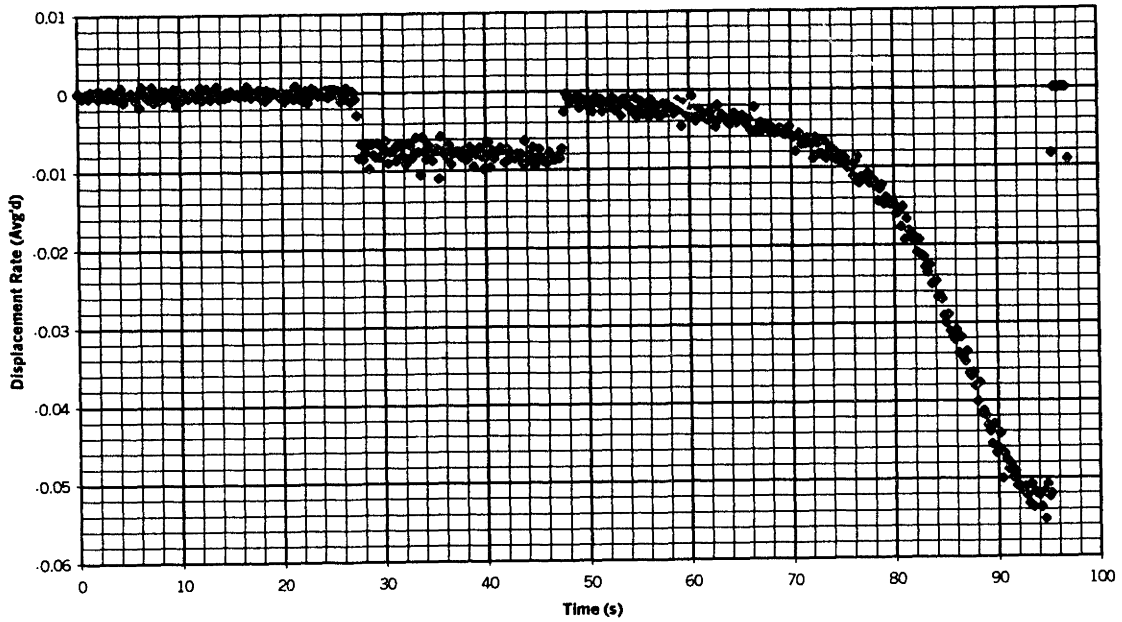
Displacement Rate vs. Time  
Si 1000 $\mu$ m, 9x45+mm, 800 $^{\circ}$ C 15.1N



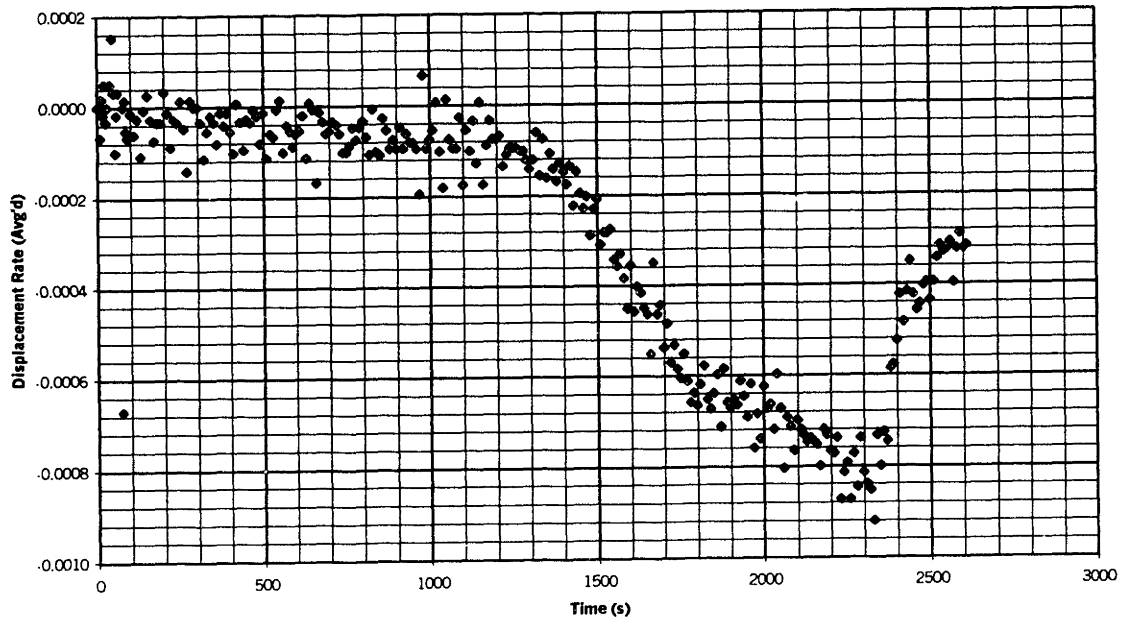
Displacement Rate vs. Time  
Si 1000 $\mu$ m, 9x45+mm, 800 $^{\circ}$ C 24.1N



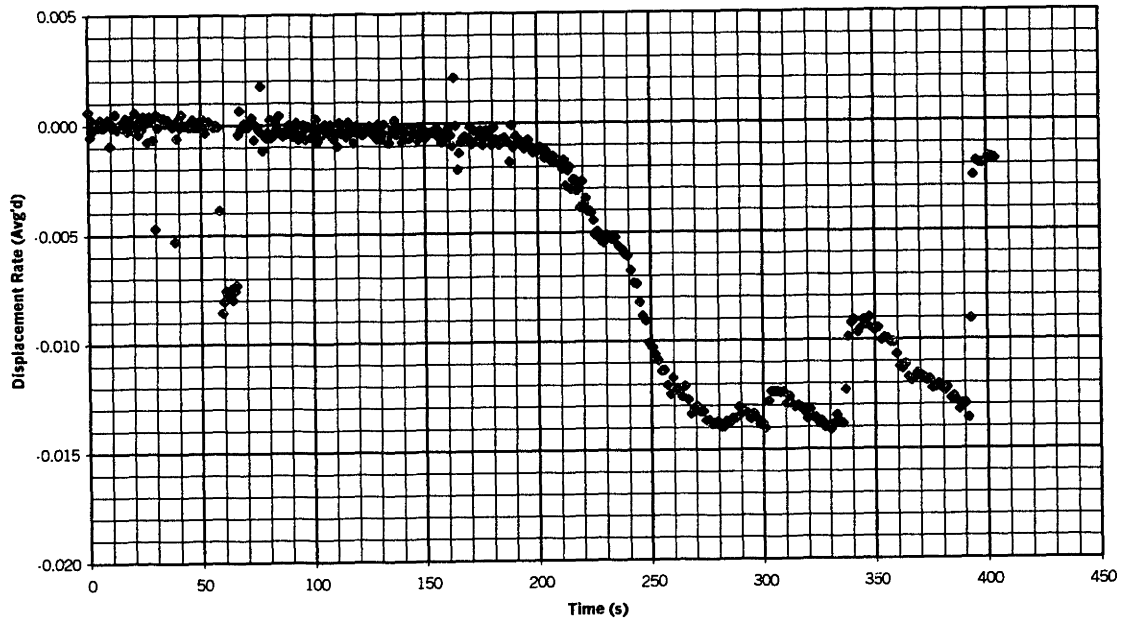
Displacement Rate vs. Time  
Si 1000 $\mu$ m, 9x45+mm, 800°C 30.0N



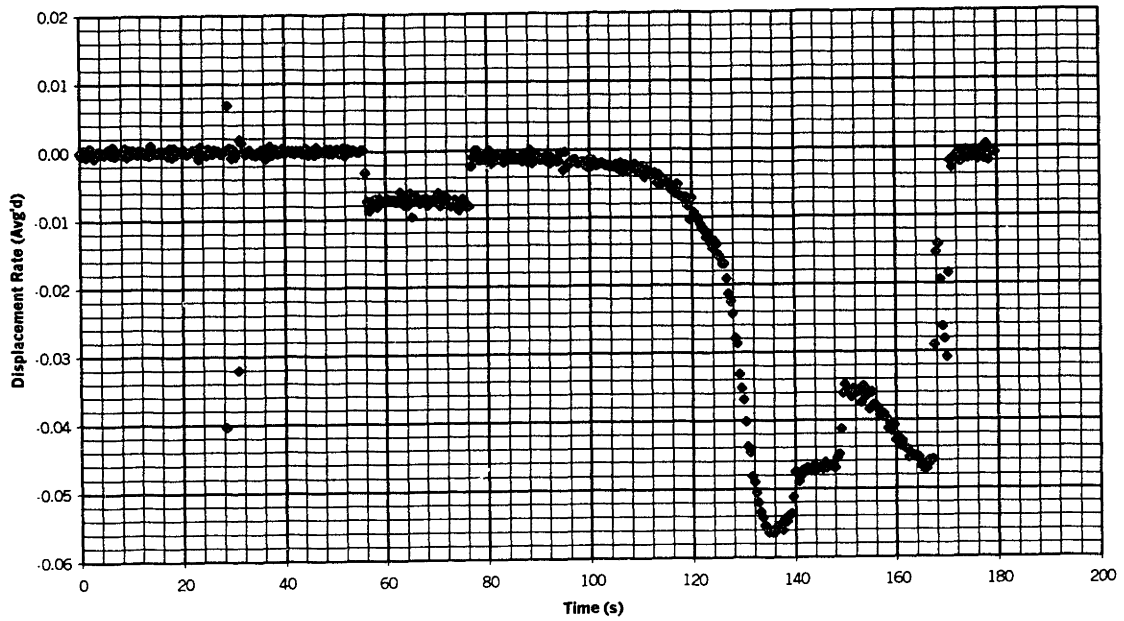
Displacement Rate vs. Time  
Si 1000 $\mu$ m, 9x45+mm, 850°C 9.1N



Displacement Rate vs. Time  
Si 1000 $\mu$ m, 9x45+mm, 850°C 15.2N

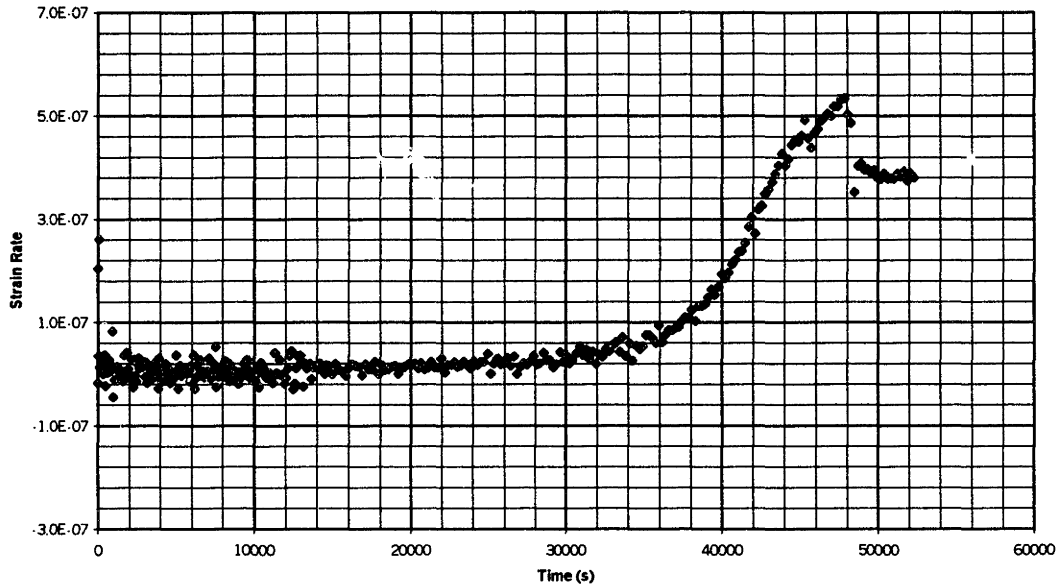


Displacement Rate vs. Time  
Si 1000 $\mu$ m, 9x45+mm, 850°C 24.3N

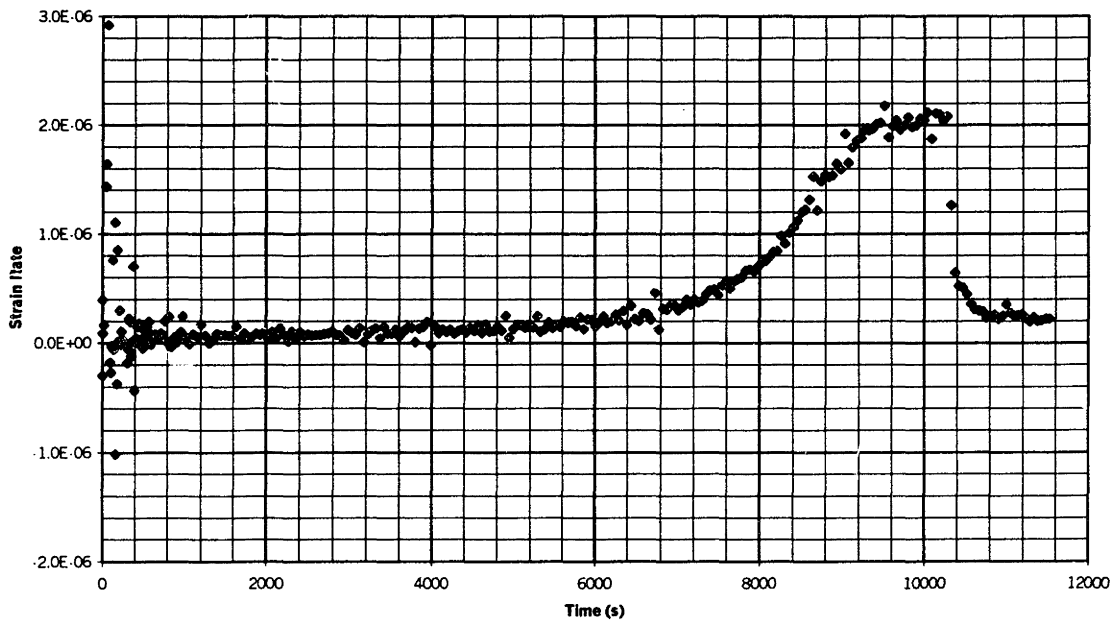


# APPENDIX A.10 Strain Rate (1/s) vs. Time (s) Plots

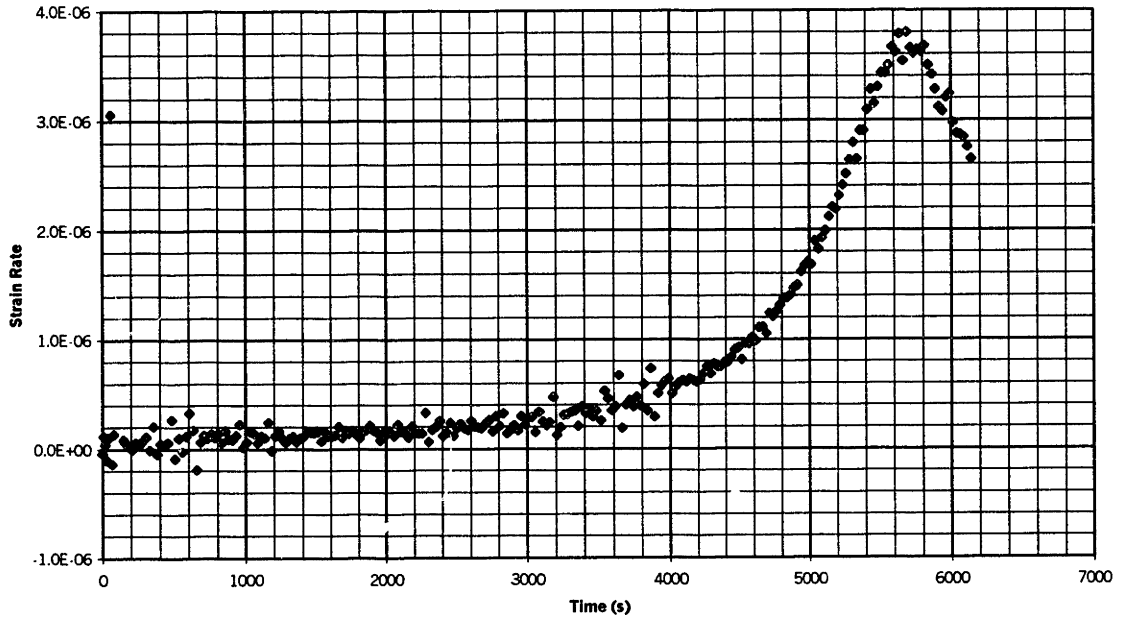
Strain Rate (Avg'd) vs. Time  
Si 1000 $\mu$ m, 9x45+mm, 600°C 30.3N



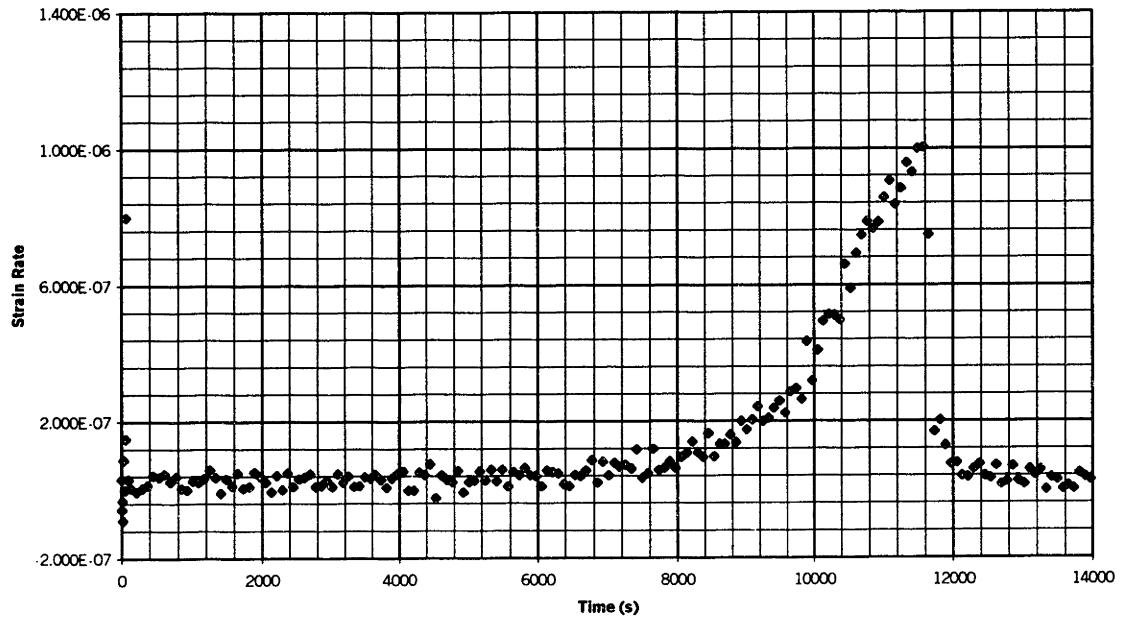
Strain Rate (Avg'd) vs. Time  
Si 1000 $\mu$ m, 9x45+mm, 600°C 45.5N



Strain Rate (Avg'd) vs. Time  
Si 1000 $\mu$ m, 9x45+mm, 600°C 60.4N

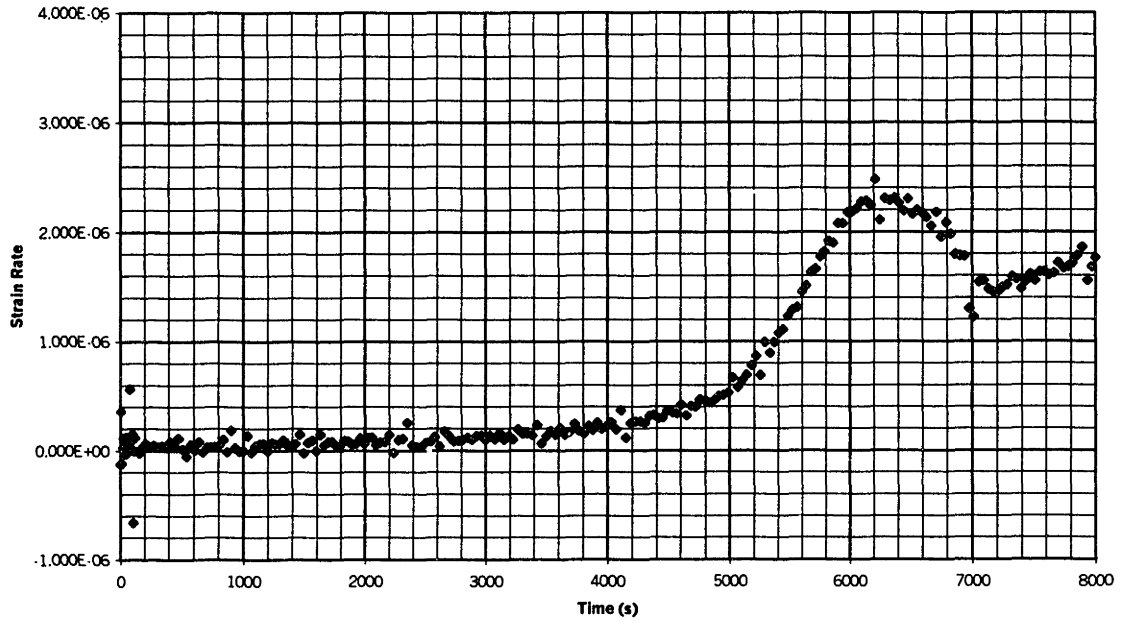


Strain Rate (Avg'd) vs. Time  
Si 1000 $\mu$ m, 9x45+mm, 650°C 24.2N

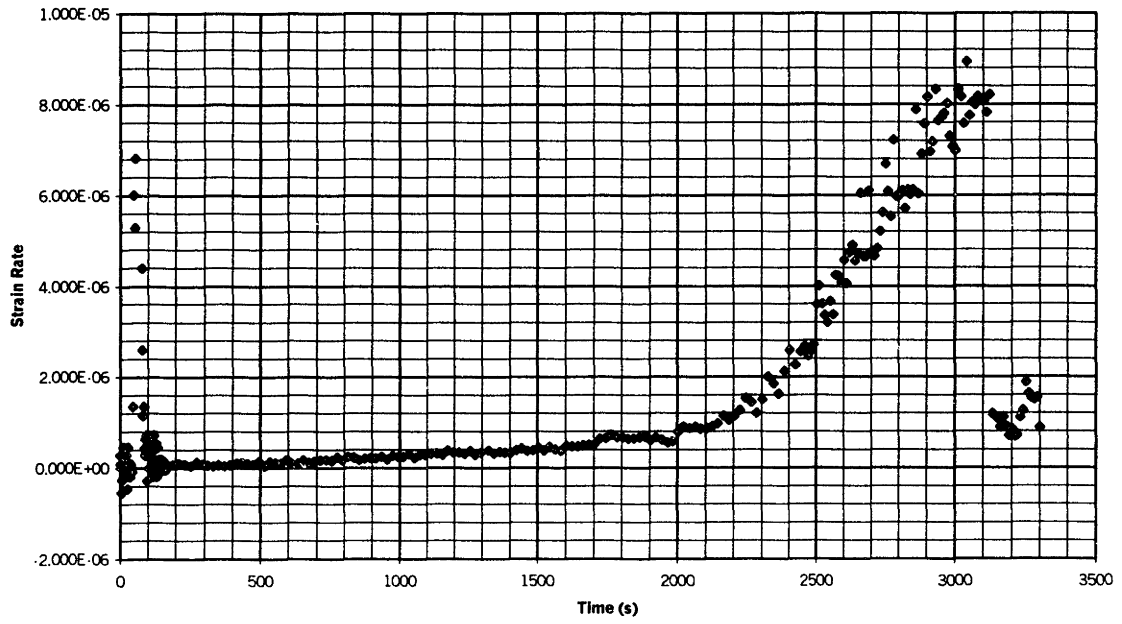




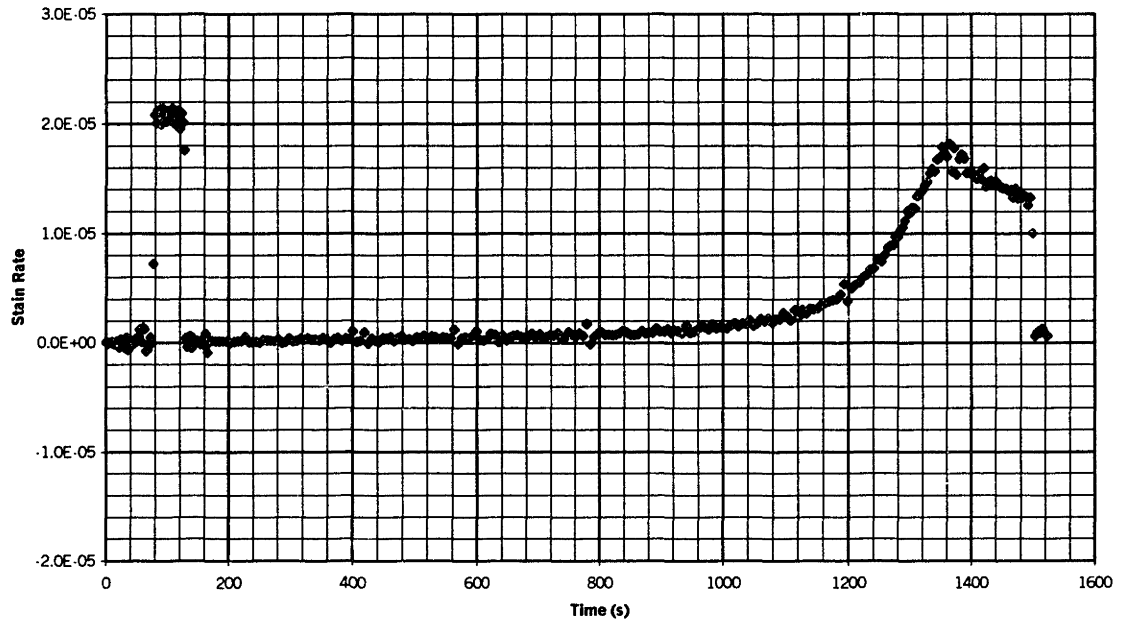
Strain Rate (Avg'd) vs. Time  
Si 1000 $\mu$ m, 9x45+mm, 650°C 30.3N



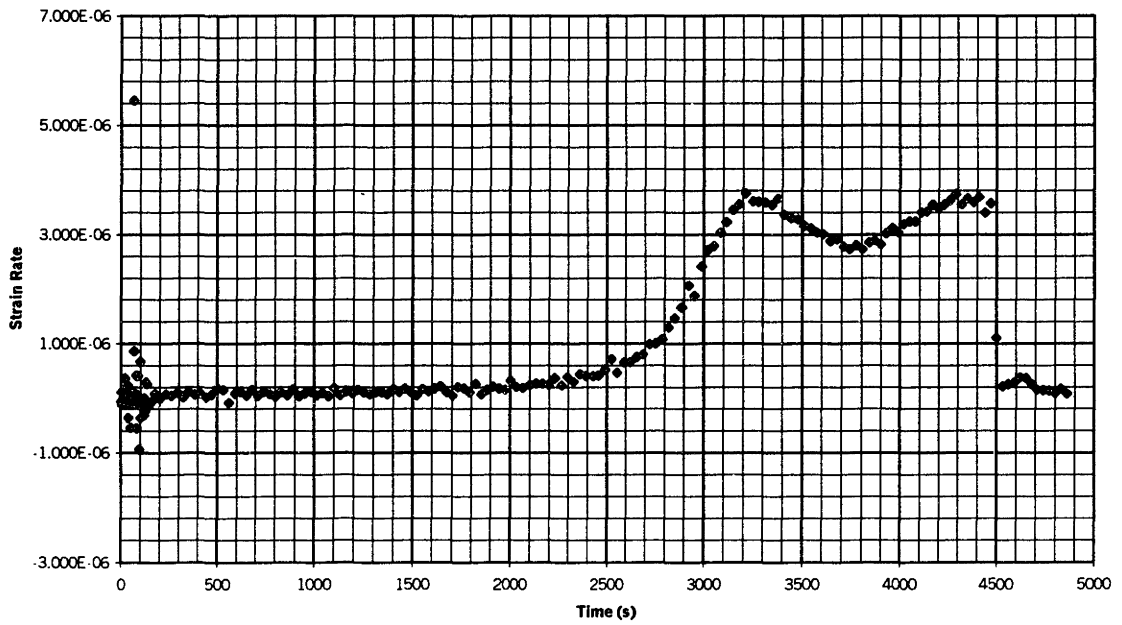
Strain Rate (Avg'd) vs. Time  
Si 1000 $\mu$ m, 9x45+mm, 650°C 45.5N



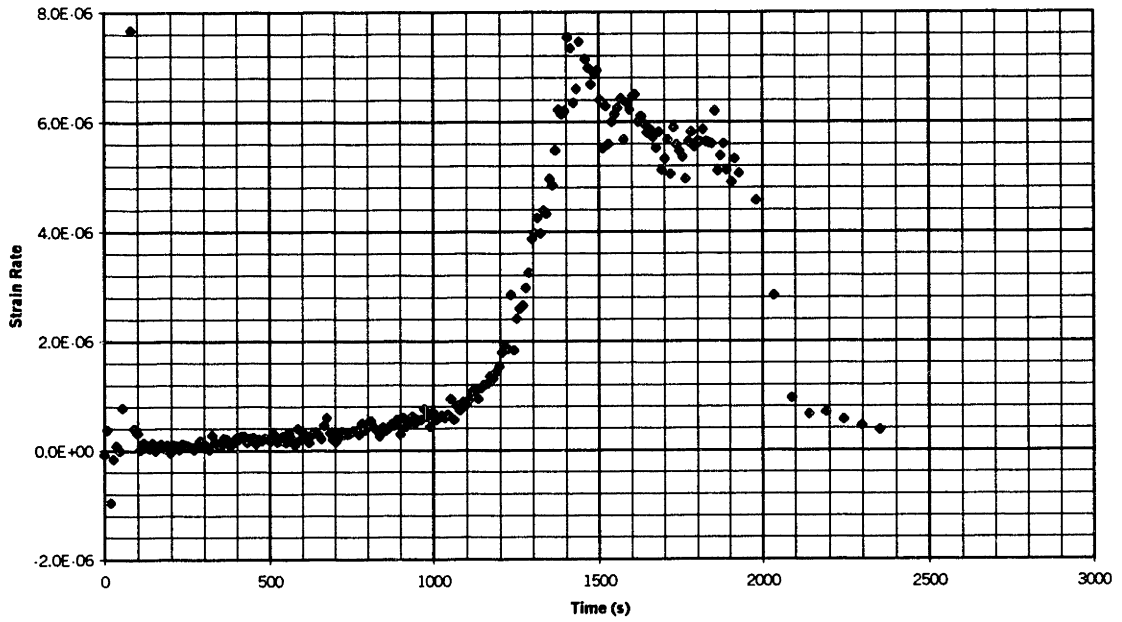
Strain Rate (Avg'd) vs. Time  
Si 1000 $\mu$ m, 9x45+mm, 650°C 60.1N



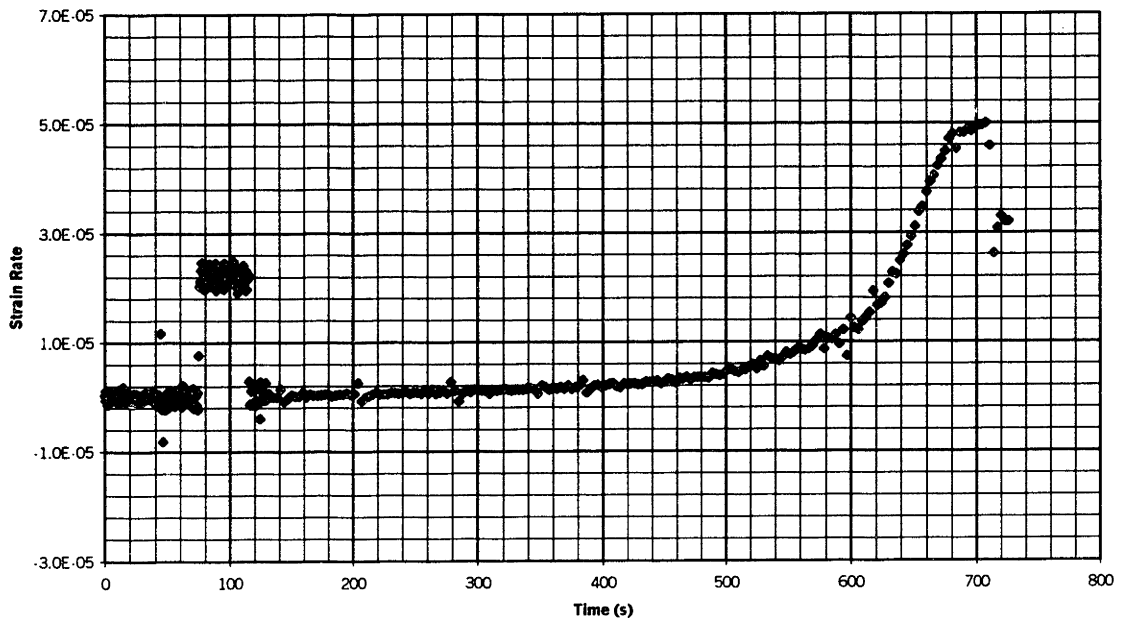
Strain Rate vs. Time  
Si 1000 $\mu$ m, 9x45+mm, 700°C 24.3N



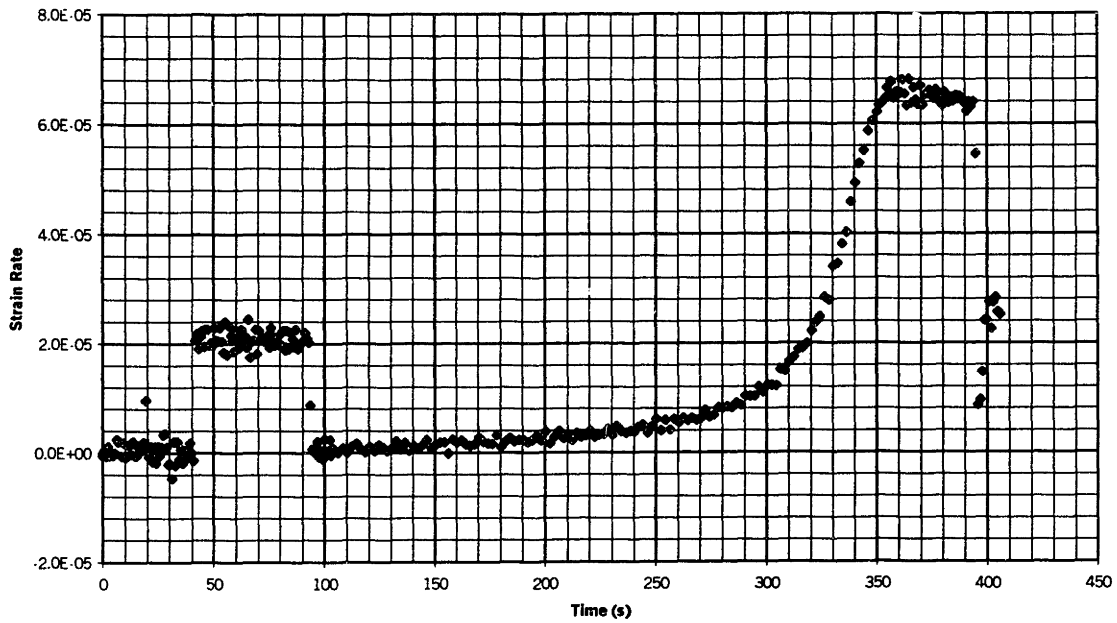
Strain Rate (Avg'd) vs. Time  
Si 1000 $\mu$ m, 9x45+mm, 700°C 30.3N



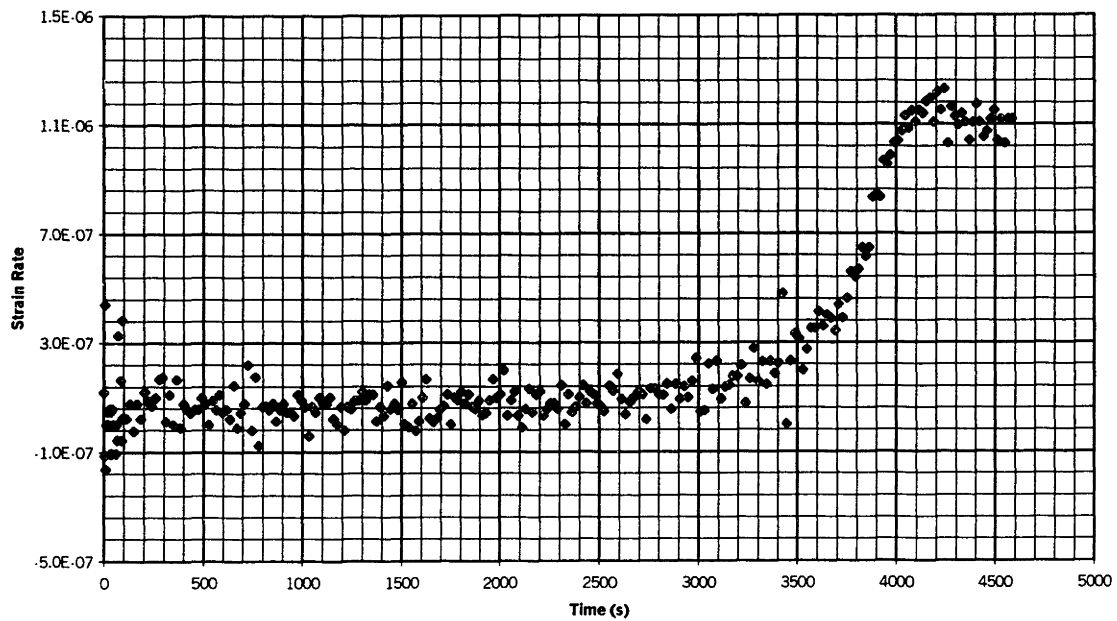
Strain Rate vs. Time  
Si 1000 $\mu$ m, 9x45+mm, 700°C 45.5N



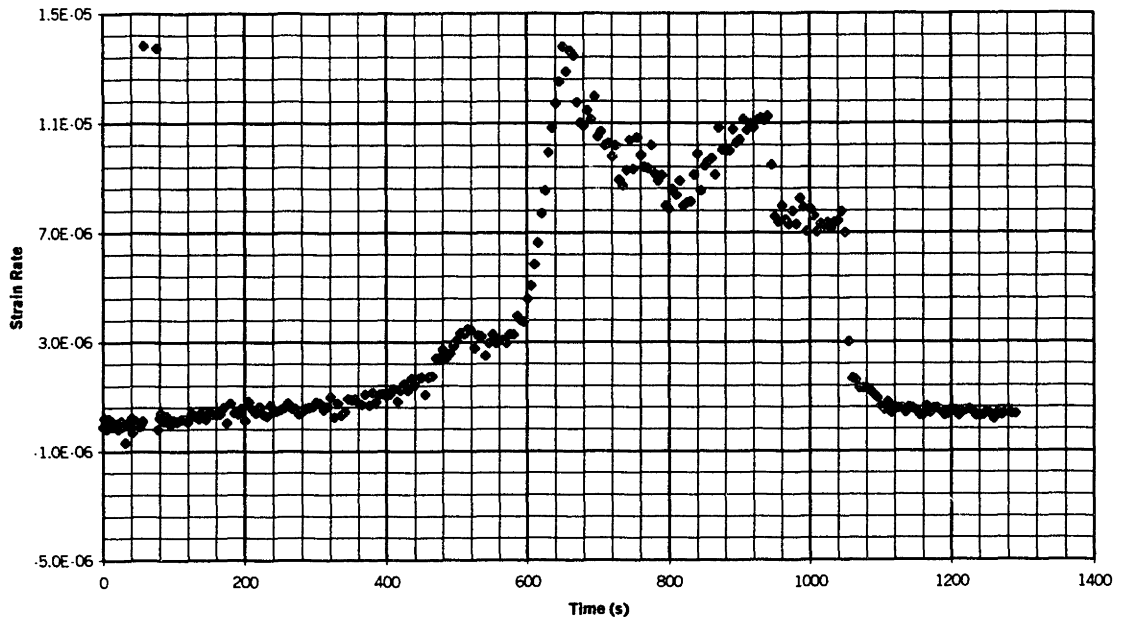
Strain Rate vs. Time  
Si 1000 $\mu$ m, 9x45+mm, 700°C 60.6N



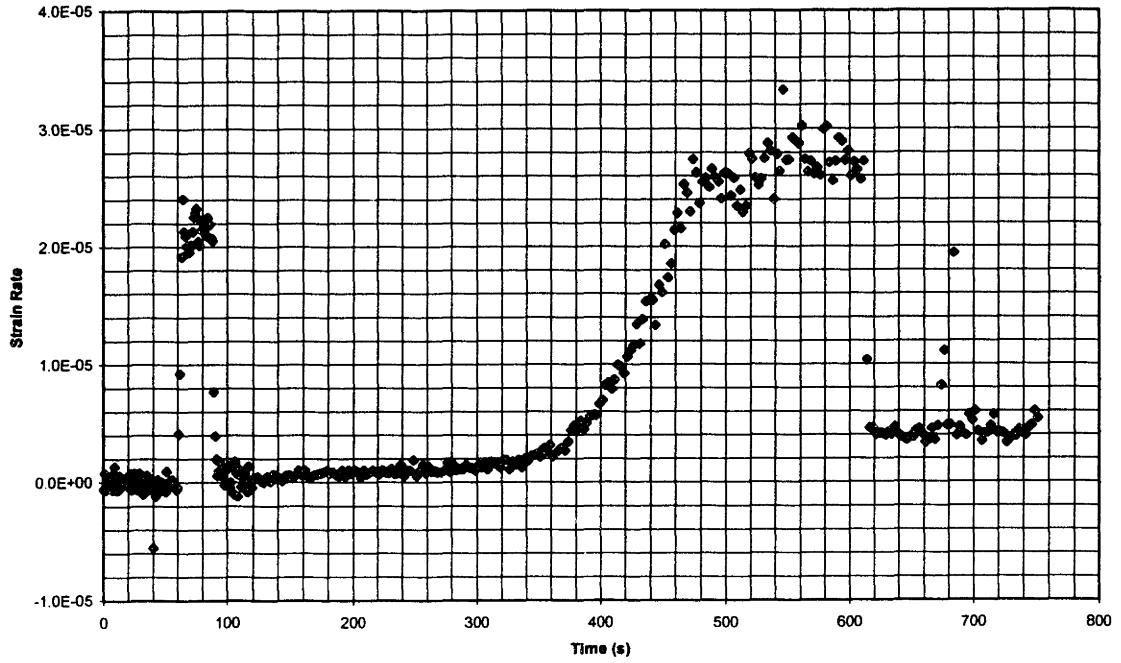
Strain Rate (Avg'd) vs. Time  
Si 1000 $\mu$ m, 9x45+mm, 750°C 15.2N



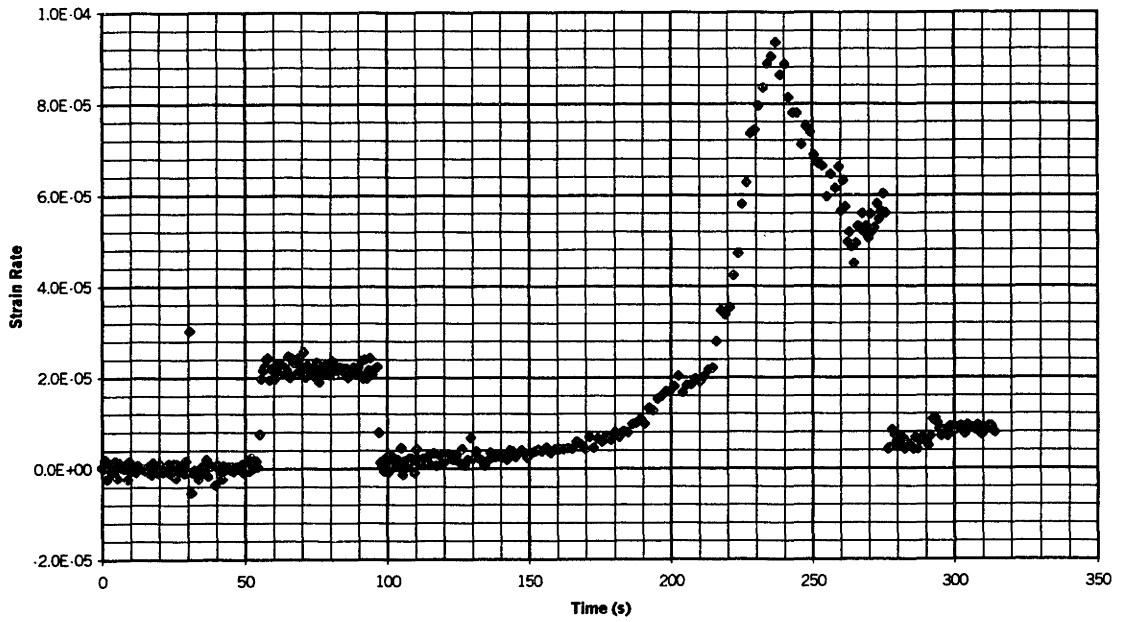
Strain Rate (Avg'd) vs. Time  
Si 1000 $\mu$ m, 9x45+mm, 750°C 24.2N



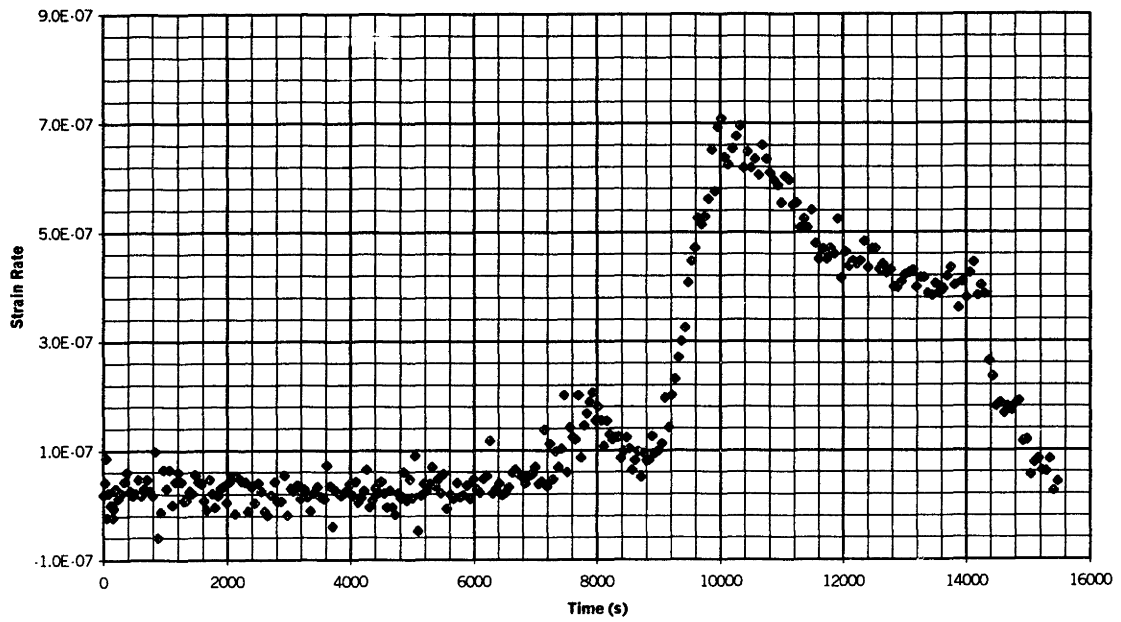
Strain Rate (Avg'd) vs. Time  
Si 1000mm, 9x45+mm, 750°C 30.3N



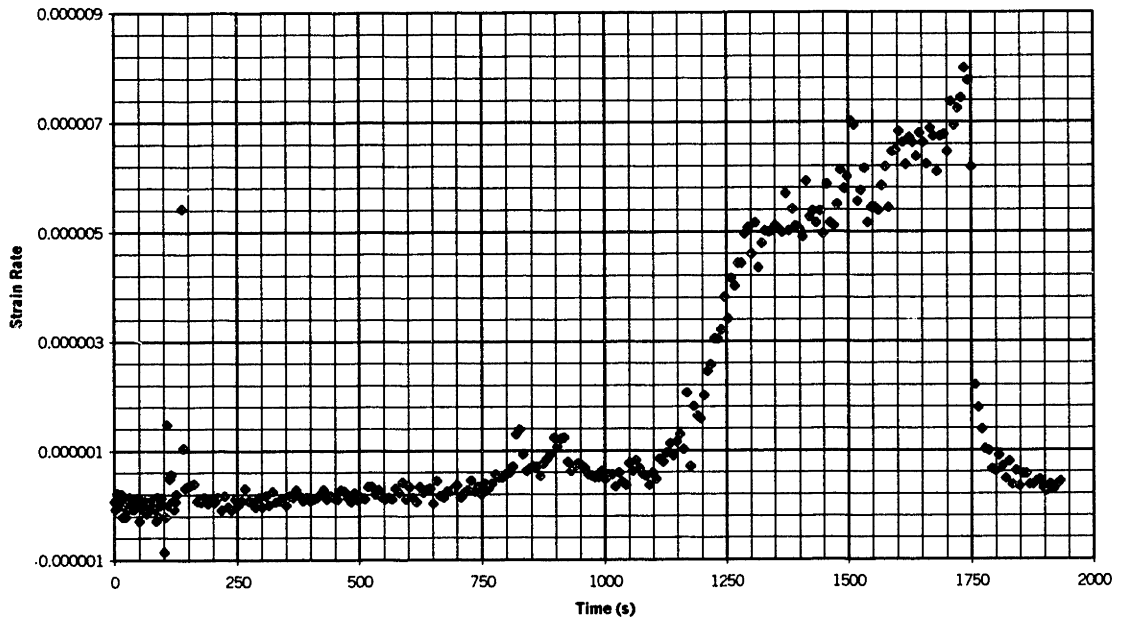
Strain Rate (Avg'd) vs. Time  
Si 1000 $\mu$ m, 9x45+mm, 750°C 45.0N



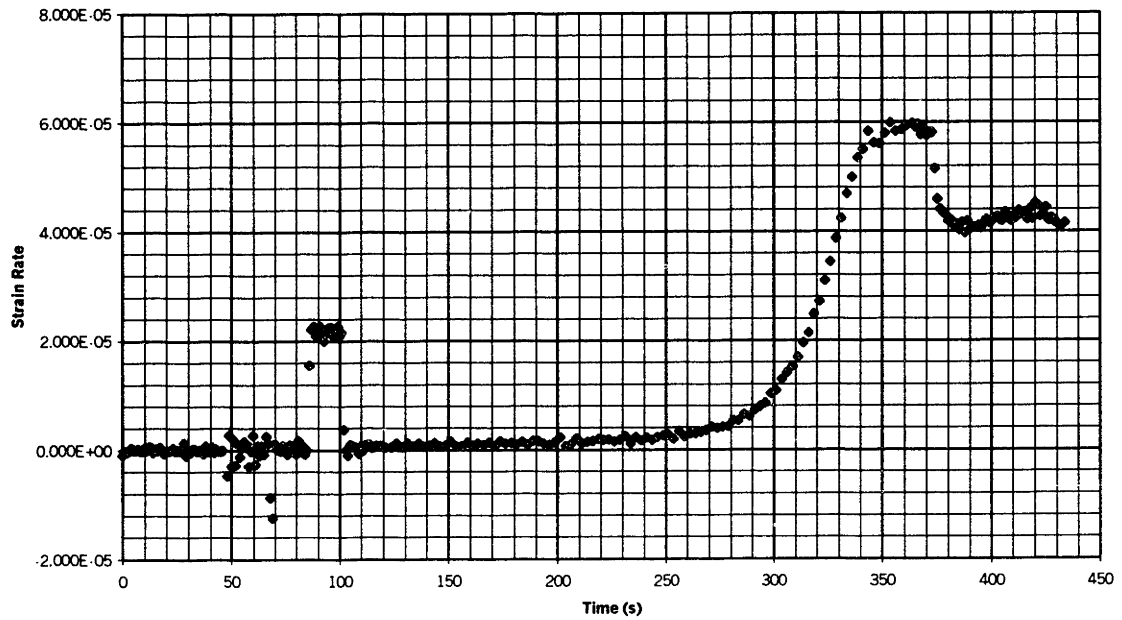
Strain Rate (Avg'd) vs. Time  
Si 1000 $\mu$ m, 9x45+mm, 800°C 9.09N



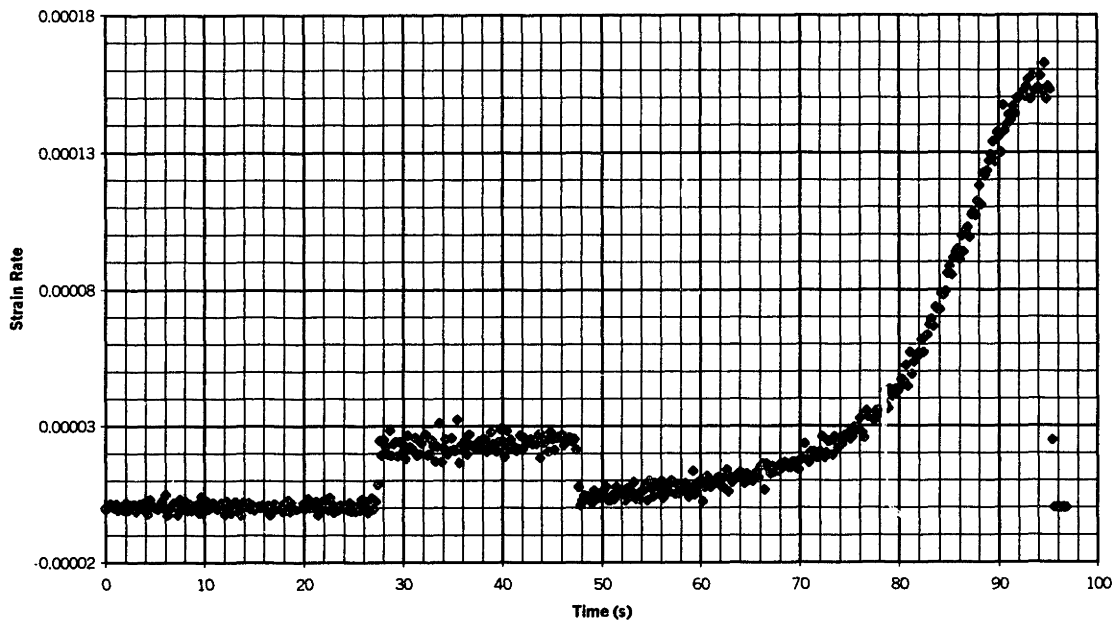
Strain Rate (Avg'd) vs. Time  
Si 1000 $\mu$ m, 9x45+mm, 800°C 15.1N



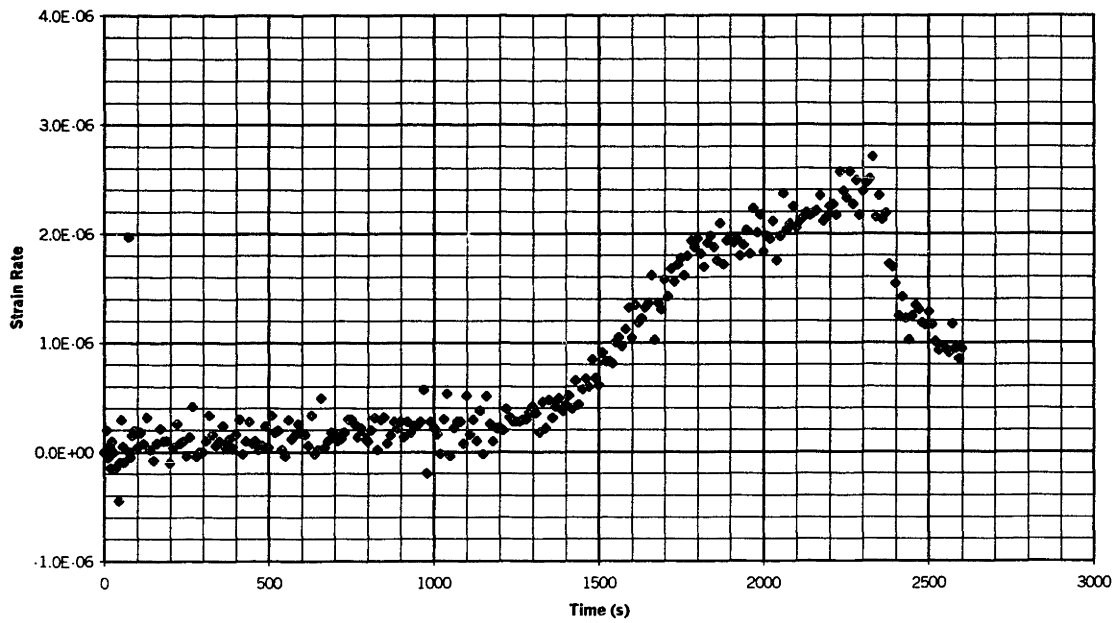
Strain Rate (Avg'd) vs. Time  
Si 1000 $\mu$ m, 9x45+mm, 800°C 24.1N



Strain Rate (Avg'd) vs. Time  
Si 1000 $\mu$ m, 9x45+mm, 800°C 30.0N

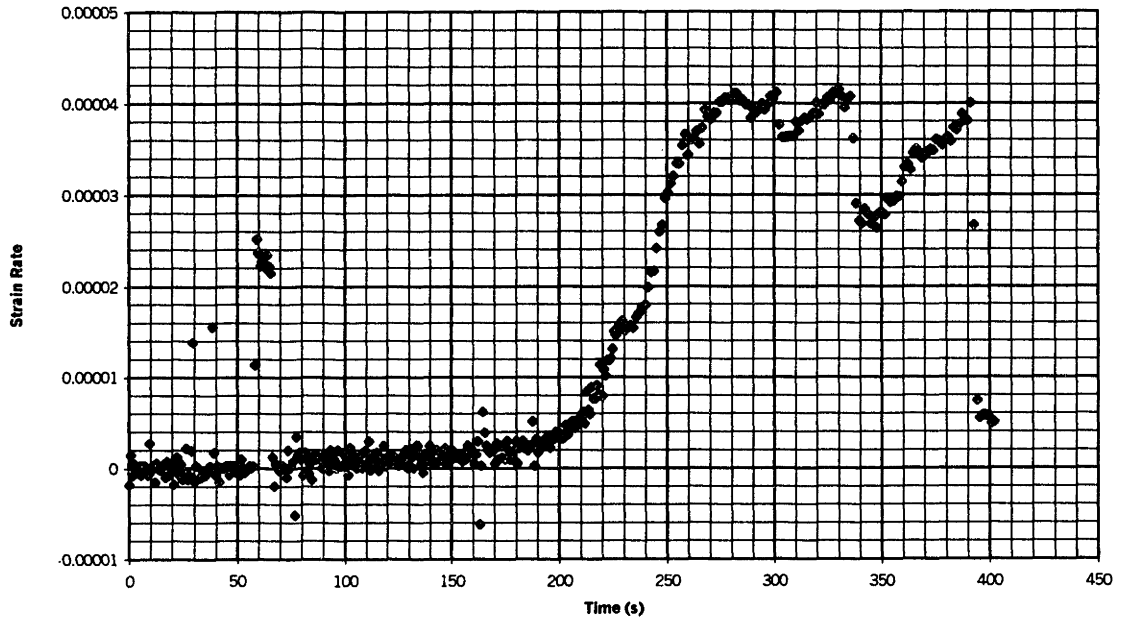


Strain Rate (Avg'd) vs. Time  
Si 1000 $\mu$ m, 9x45+mm, 850°C 9.1N

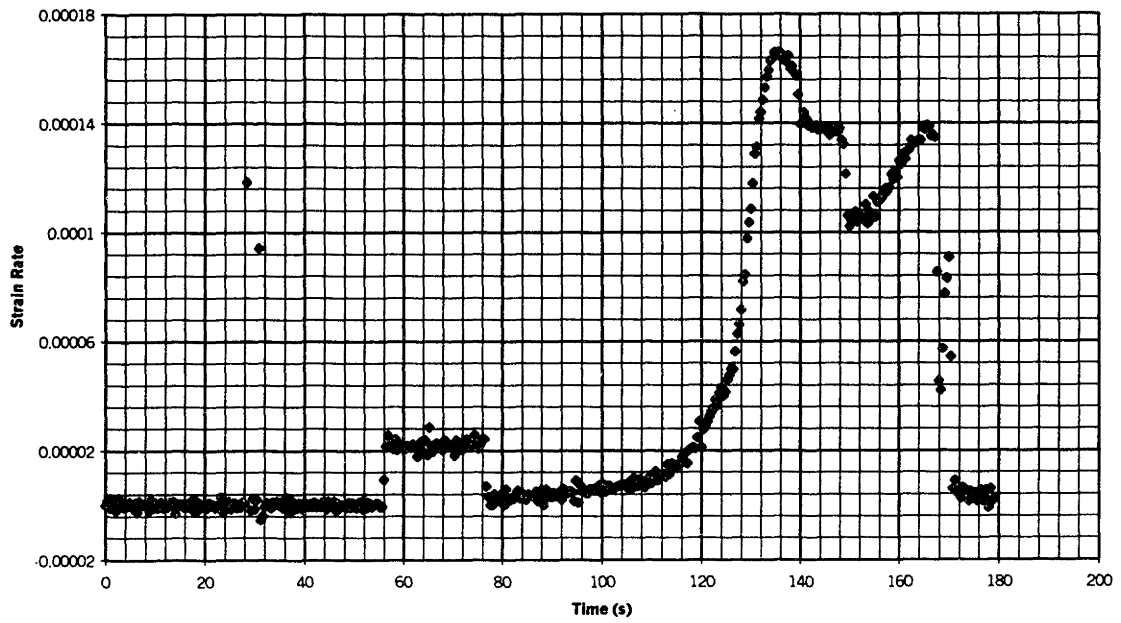




Strain Rate (Avg'd) vs. Time  
Si 1000 $\mu$ m, 9x45+mm, 850°C 15.2N



Strain Rate (Avg'd) vs. Time  
Si 1000 $\mu$ m, 9x45+mm, 850°C 24.3N



## APPENDIX A.11 ANSYS 5.4a Modeling Details: Finding the Proportionality Constant

The first step to determine the power law creep proportionality constant using an ANSYS finite element model is to generate the geometry. The geometry modeled is that of a 50 mm long test specimen, with a thickness of 1 mm and a width of 9 mm. Each of the 4-point bend fixture rollers is modeled with a nominal radius of 5 mm. Due to the symmetry associated with the test, only half of the setup is required to be modeled. The batch file used to run the ANSYS analysis is included in APPENDIX A.12.

The analysis is performed using a 2D ANSYS54a model. The structures within the model (specimen and rollers) are generated using PLANE42 solid elements with a real constant thickness value of 9 mm. Figure A10.1 shows the boundary conditions during the loading portion of the test.

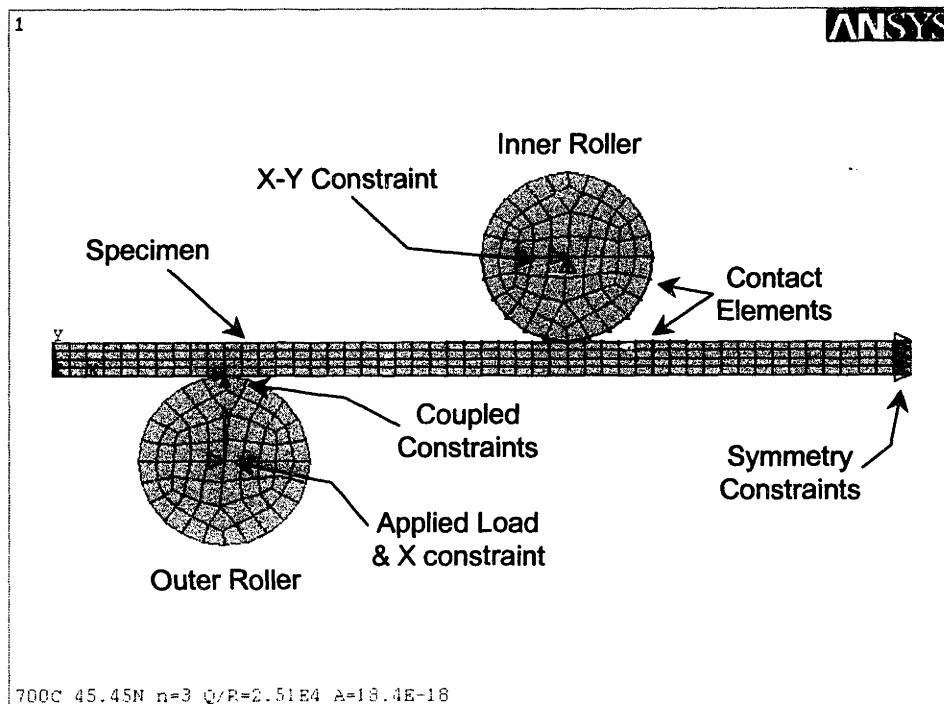


Figure A11.1: Finite element model boundary conditions.

To maintain the symmetry at the midspan of the specimen, zero DOF horizontal constraints are added to the nodes along the symmetry line. Consistent with the actual test conditions, the upper roller is constrained with zero DOF in both the horizontal and vertical directions. However, the roller is permitted to rotate freely. Compliance between the specimen and the upper roller is maintained using CONTAC48 contact elements. The lower roller provides the applied load, which is positioned on the center node of the roller. A zero DOF horizontal constraint is also placed on this node to ensure that the roller travels solely in the vertical direction. Since the lower roller is free to move vertically, compliance can be maintained by coupling the nodes at the contact point. Note that this is only valid for limited vertical travel of the lower roller. For the purpose of these tests, this constraint is valid.

The material properties in this model are listed in Table A11.1. The values for the elasticity moduli were taken from the work of Kuo-Shen Chen in the MIT Gas Turbine Lab<sup>23</sup>.

<b>Material Property</b>	<b>Value</b>	<b>Valid Temperature (K)</b>
Poisson's Ratio	0.27	All Tested
Density	22799 kg/m <sup>3</sup>	All Tested
Modulus of Elasticity	166 GPa	873
Modulus of Elasticity	162 GPa	923
Modulus of Elasticity	158 GPa	973
Modulus of Elasticity	154 GPa	1023
Modulus of Elasticity	150 GPa	1073
Modulus of Elasticity	146 GPa	1123

Table A11.1: ANSYS model material properties.

The model was run in 3 load cases. The first load case has no applied load on the lower roller. Instead, the lower roller is displaced upward a value of 0.05 mm using a vertical DOF constraint. This first load case improves model convergence by ensuring that the contact

elements between the specimen and upper roller are "talking" and will supply sufficient constraint to the model. Without this initial step, an applied load to the lower roller will usually send the unrestrained specimen out to infinite. The second load case removes the lower roller vertical displacement constraint and applies the desired load. The load is ramped from zero to full value at a rate of 1 Newton/second. Once the load reaches its full value the third load case begins. In this load case, the full load value is maintained at a constant level while the specimen is allowed to creep. A sample end of test deformed shape plot is shown in Figure A11..2.

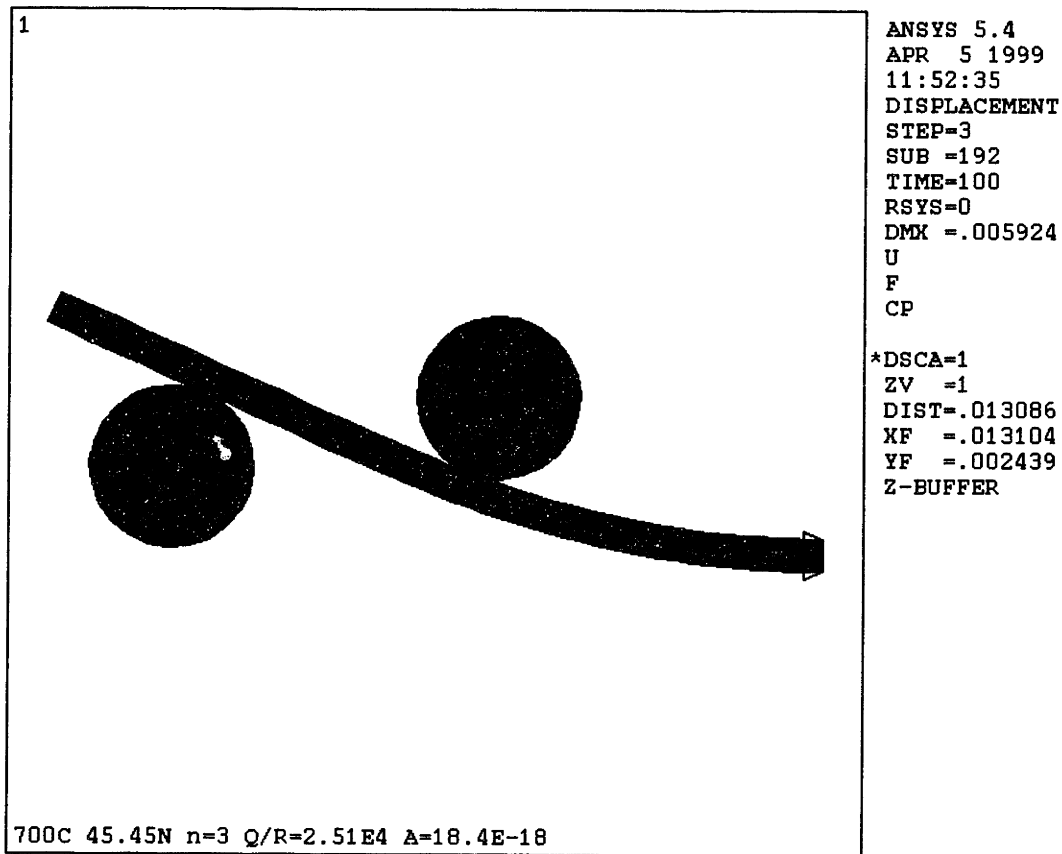


Figure A11.2: Sample deformed shape plot.

# APPENDIX A.12 ANSYS 5.4a Batch File: Finding the Proportionality Constant

```
/BATCH
/INPUT,start,ans,/afs/ae.ge.com/apps/ansys54a/docu/
/INPUT,maintbar,abr,/ansys54/
/PREP7
/UNITS,SI
/TITLE,700C 45.45N n=3 Q/R=2.51E4 A=18.4E-18
!
ET,1,PLANE42
!
KEYOPT,1,3,3
KEYOPT,1,5,2
KEYOPT,1,6,0
!
! ELEMENT THICKNESS DEFINED
!
R,1,.009
!
! MATERIAL PROPERTIES
!
UIMP,1,PRXY,,0.27,
UIMP,1,DENS,,22799,
UIMP,1,NUXY,,0.27,
UIMP,2,PRXY,,0.27,
UIMP,2,DENS,,22799,
UIMP,2,NUXY,,0.27,
MPTEMP,1,873,923,973,1023,1073,1123,
MPDATA,EX,1,1,166E9,162E9,158E9,154E9,150E9,146E9,
MPDATA,EY,1,1,166E9,162E9,158E9,154E9,150E9,146E9,
MPDATA,EZ,1,1,166E9,162E9,158E9,154E9,150E9,146E9,
MPDATA,EX,2,1,166E9,162E9,158E9,154E9,150E9,146E9,
MPDATA,EY,2,1,166E9,162E9,158E9,154E9,150E9,146E9,
MPDATA,EZ,2,1,166E9,162E9,158E9,154E9,150E9,146E9,
!
! *****
! * GEOMETRY DEFINED *
! *****
!
! SPECIMEN KEYPOINTS
!
K,1,0.0000,0.0000,0.0000
K,2,0.0015,0.0000,0.0000
K,3,0.0050,0.0000,0.0000
K,4,0.0085,0.0000,0.0000
K,5,0.0250,0.0000,0.0000
K,6,0.0250,0.0010,0.0000
K,7,0.0185,0.0010,0.0000
K,8,0.0150,0.0010,0.0000
K,9,0.0115,0.0010,0.0000
K,10,0.0000,0.0010,0.0000
```

```

!
! SPECIMEN LINES
!
L,1,2
L,2,3
L,3,4
L,4,5
L,5,6
L,6,7
L,7,8
L,8,9
L,9,10
L,10,1
!
! SPECIMEN AREAS
!
AL,ALL
!
! ROLLER KEYPOINTS
!
K,11,0.0050,-0.0025,0.0000
K,12,0.015,0.0035,0.0000
!
! ROLLER LINES
!
CIRCLE,11,0.0025
CIRCLE,12,0.0025
L,13,15
L,17,19
!
! ROLLER AREAS
!
AL,11,12,19
AL,13,14,19
AL,15,16,20
AL,17,18,20
!
! ELEMENT SIZE DEFINITIONS
!
LESIZE,1,,3
LESIZE,2,,7
LESIZE,3,,7
LESIZE,4,,33
LESIZE,5,,4
LESIZE,6,,13
LESIZE,7,,7
LESIZE,8,,7
LESIZE,9,,23
LESIZE,10,,4
LESIZE,11,,6
LESIZE,12,,6
LESIZE,13,,6
LESIZE,14,,6
LESIZE,15,,6
LESIZE,16,,6
LESIZE,17,,6
LESIZE,18,,6

```

```

LESIZE,19,,,10
LESIZE,20,,,10
!
ESHAPE,3,0
TYPE,1
MAT,1
!
LSEL,S,LINE,,1,4,1
LCCAT,ALL
LSEL,S,LINE,,6,9,1
LCCAT,ALL
!
! MESHING AREAS
!
ALLSEL,ALL
AMESH,1,1,1
MAT,2
AMESH,2,5,1
!
! CONTACT ELEMENT DEFINITION
!
LSEL,S,LINE,,17,18,1
NSLL,S,1
CM,ROLL1,NODE
ALLSEL,ALL
LSEL,S,LINE,,7,8,1
NSLL,S,1
CM,BEAM1,NODE
ALLSEL,ALL
!
ET,2,CONTAC48
!
KEYOPT,2,1,1
KEYOPT,2,2,0
KEYOPT,2,3,0
KEYOPT,2,7,0
!
R,2,1.42E9,,1E-7,,,1,
TYPE,2
MAT,1
REAL,2
!
GCGEN,ROLL1,BEAM1,,,TOP,
GCGEN,BEAM1,ROLL1,,,TOP,
!
! DEFINING COUPLED NODES
!
KSEL,S,KP,,3,14,11
NSLK,S
CPINTF,ALL,.0001
ALLSEL,ALL
!
FINISH
/SOLU
!
! *****
! * BOUNDARY CONDITIONS *

```

```

! *****
!
! LOAD STEP #1
!
DK,5,UX,0, ,1
DK,6,UX,0, ,1
NSEL,S,LOC,X,0.005
NSEL,R,LOC,Y,-0.0025
D,ALL,UX,0
D,ALL,UY,0.00005
ALLSEL,ALL
NSEL,S,LOC,X,0.015
NSEL,R,LOC,Y,0.0035
D,ALL,UX,0
D,ALL,UY,0
ALLSEL,ALL
!
TB,CREEP
!
! CREEP EQUATION
!
TBDATA,7,18.4E-18,3,,2.51E4,,1
!
BF,ALL,TEMP,973
TOFFST,0
!
ANTYPE,4
TRNOPT,FULL
LUMPM,0
NLGEOM,1
SSTIF,0
NROPT,AUTO, ,ON
EQSLV,FRONT, ,0,
!
TIME,2
AUTOTS,1
DELTIM,0.2,0.2,10,0
KBC,1
NEQIT,50
!
OUTRES,ESOL,1,
OUTRES,NSOL,1,
CRPLIM,.22,
!
LSWRITE,1,
!
! LOAD STEP #2
!
NSEL,S,LOC,X,0.005
NSEL,R,LOC,Y,-0.0025
DDELE,ALL,UY
!
! 1/2 APPLIED LOAD
!
F,ALL,FY,22.725
!
ALLSEL,ALL

```



```
!  
TIME, 4  
AUTOTS, 1  
DELTIM, 0.2, 0.2, 10, 0  
KBC, 0  
NEQIT, 100  
!  
LSWRITE, 2,  
!  
! LOAD STEP #3  
!  
TIME, 100  
!  
AUTOTS, 1  
DELTIM, 0.5, 0.5, 10, 0  
KBC, 0  
NEQIT, 100  
!  
LSWRITE, 3,  
!  
LSSOLVE, 1, 3, 1  
!  
/COLOR, NUM, BMAG, 1  
/COLOR, NUM, RED, 2  
/COLOR, NUM, CYAN, 3  
!  
/PBC, ALL, , 1  
!  
FINISH
```

## APPENDIX A.13 MIT Single-Crystal Silicon Yield Test Results

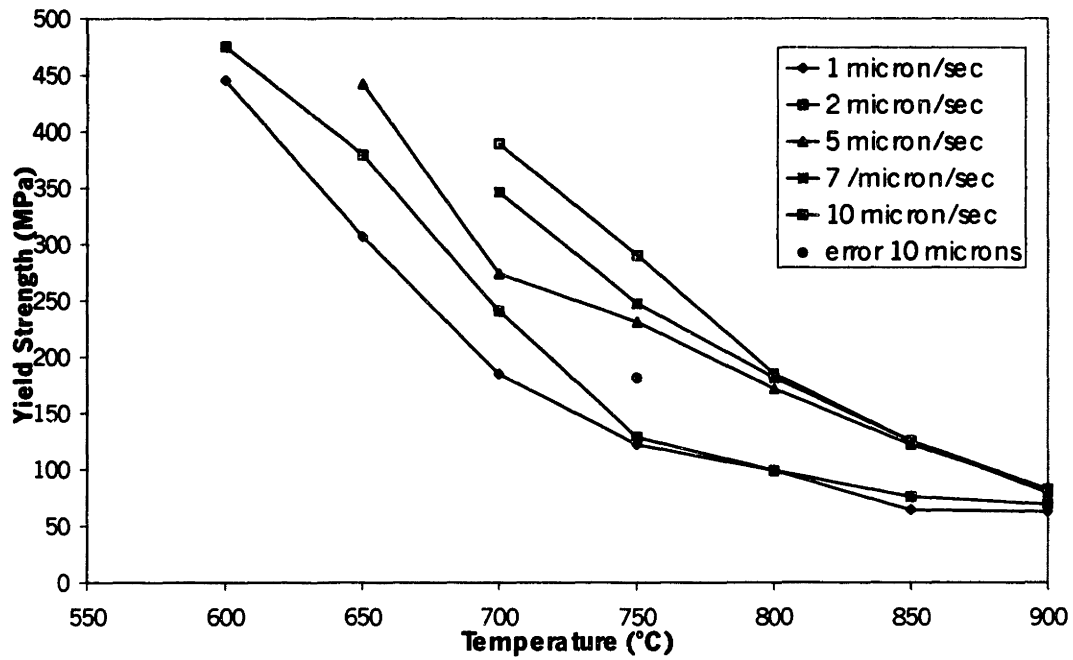


Figure A13.1: Yield strength curves at varying strain rates  
(Courtesy of K-S Chen)

## APPENDIX A.14 MathCAD Contact Stress Calculations

### Calculation of Contact Stresses

$$i := 1, 2..6$$

$$j := 1, 2..6$$

$$F_i :=$$

F = 1/2 of the Applied Force (N)

4.5 newton
7.5 newton
12 newton
15 newton
23 newton
30 newton

$$T_j :=$$

T = Temperature (K)

873.15K
923.15K
973.15K
1023.15K
1073.15K
1123.15K

### Silicon and Silicon Carbide Properties

#### Modulus of Elasticity

$$E_{Si_j} := -.045 \left( \frac{\text{GPa}}{\text{K}} \right) \cdot T_j + 198.79 \text{ GPa}$$

$$E_{SiC_j} := -.0338 \left( \frac{\text{GPa}}{\text{K}} \right) \cdot T_j + 401.89 \text{ GPa}$$

#### Diameters

$$d_{Si} := 99 \cdot 10^{-9} \cdot \text{m}$$

$$d_{SiC} := .005 \cdot \text{m}$$

#### Poisson's Ratio

$$v_{Si} := .27$$

$$v_{SiC} := .14$$

### Specimen width

$$l := .009\text{m}$$

### Calculating the half width

$$b_{j,i} := \sqrt{\frac{2 \cdot F_i}{\pi \cdot l} \cdot \frac{\frac{1 - v_{Si}^2}{E_{Si_j}} + \frac{1 - v_{SiC}^2}{E_{SiC_j}}}{\left(\frac{1}{d_{Si}} + \frac{1}{d_{SiC}}\right)}}$$

### Calculating the maximum pressure

$$P_{max_{j,i}} := \frac{2 \cdot F_i}{\pi \cdot b_{j,i} \cdot l}$$

### Calculating the contact stresses (on the surface)

$$\sigma_{x_{j,i}} := -2 \cdot v_{Si} \cdot P_{max_{j,i}}$$

$$\sigma_{y_{j,i}} := -P_{max_{j,i}}$$

$$\sigma_{z_{j,i}} := -P_{max_{j,i}}$$

### Calculating the bending stresses

#### Load-point span half lengths

$$L := .02\text{m}$$

$$a := .01\text{m}$$

#### Specimen height

$$h := .001\text{m}$$

$$\sigma_{\text{bend}_i} := \frac{-3 \cdot (2 \cdot F_i) \cdot (L - a)}{I \cdot h^2}$$

### Total combined stress

$$\sigma_{\text{total}_{j,i}} := \sigma_{y_{j,i}} + \sigma_{\text{bend}_i}$$

$$\sigma_{\text{total}} = \begin{bmatrix} -116.822 & -162.087 & -221.78 & -258.514 & -349.618 & -424.173 \\ -116.337 & -161.46 & -220.987 & -257.629 & -348.522 & -422.921 \\ -115.847 & -160.828 & -220.188 & -256.735 & -347.415 & -421.657 \\ -115.353 & -160.19 & -219.381 & -255.833 & -346.297 & -420.38 \\ -114.854 & -159.546 & -218.566 & -254.921 & -345.169 & -419.092 \\ -114.35 & -158.896 & -217.743 & -254.002 & -344.03 & -417.791 \end{bmatrix} \cdot \text{MPa}$$

$$\text{WRITEPRN}(\text{outest2}) := \sigma_{\text{total}}$$

## APPENDIX A.15 LARSON-MILLER PARAMETER DATA

Larson Miller P	Temperature (°C)	Bend Stress n=3 (MPa)	Bend Stress n=1 (MPa)	Contact Stress (MPa)	Total Stress (MPa)	Begin Time (seconds)	End Time (.5% Strain)	Total Time (hours)
11024.08	600	78.57	101.02	158.50	259.52	60	48378	13.422
10415.10	600	118.00	151.71	196.30	348.01	38	9733	2.693
10207.79	600	156.71	201.48	220.90	422.38	91	5702	1.559
11125.71	650	62.64	80.54	141.00	221.54	73	12960	3.590
10882.67	650	78.58	101.03	157.60	258.63	131	7159	1.962
10540.81	650	118.00	151.71	195.17	346.88	48	3043	0.832
10221.48	650	156.88	201.70	219.57	421.27	79	1429	0.375
11241.56	700	63.08	81.10	140.20	221.30	59	4131	1.131
10922.44	700	78.67	101.15	156.70	257.85	62	1975	0.532
10444.10	700	117.54	122.14	194.07	316.21	76	692	0.171
10182.16	700	156.88	201.70	218.37	420.07	42	374	0.092
12093.28	750	39.33	50.57	110.20	160.77	75	7620	2.096
11167.20	750	62.80	80.74	139.40	220.14	59	997	0.261
10904.28	750	78.47	100.89	155.80	256.69	62	581	0.144
10502.03	750	116.73	150.08	192.97	343.05	55	265	0.058
13080.70	800	23.57	30.30	84.90	115.20	137	17800	4.907
11623.21	800	39.06	50.22	109.50	159.72	129	903	0.215
11198.32	800	62.54	80.41	138.60	219.01	87	398	0.086
10892.09	800	78.65	101.12	154.90	256.02	80	241	0.045
12925.82	850	23.63	30.38	84.40	114.78	66	3750	1.023
11695.21	850	39.64	50.97	108.90	159.87	59	355	0.082
11170.17	850	62.60	80.49	137.70	218.19	56	157	0.028

## REFERENCES

- <sup>1</sup> A.H. Epstein, S.D. Senturia, O. Al-Midani, G. Anathasuresh, A. Ayon, K. Breuer, K-S Chen, F.E. Ehrich, E. Esteve, L. Frechette, G. Gauba, R. Ghodssi, C. Groshenry, S. Jacobson, J.L. Kerrebrock, J.H. Lang, C-C Lin, A. London, J. Lopata, A. Mehra, J.O. Mur Miranda, S. Nagle, D.J. Orr, E. Piekos, M.A. Schmidt, G. Shirley, S. M. Spearing, C. S. Tan, Y-S Tzeng, I.A. Waitz, "Micro-Heat Engines, Gas Turbines, And Rocket Engines - The MIT Microengine Project" 28<sup>th</sup> AIAA Fluid Dynamics and 4<sup>th</sup> AIAA Shear Flow Control Conference, June 1997.
- <sup>2</sup> A. Ayon, K. Breuer, J. Brisson, K-S Chen, F. Ehrich, A. Epstein, E. Esteve, L. Frechette, G. Gauba, R. Ghodssi, S. Jacobson, J. Lang, C. Lin, K. Lohner, A. Mehra, J. Miranda, S. Nagle, D. Orr, E. Piekos, J. Protz, M. Schmidt, S. Senturia, G. Shirley, M. Spearing, C. Tan, Y. Tzeng, S. Umans, I. Waitz, "Micro Gas Turbine Generators", MIT Interim Technical Progress Report for the U.S. Army Research Office, Report Number 33888CH-MUR, February 1998.
- <sup>3</sup> S.M. Hu, "Critical Stress in Silicon Brittle Fracture, and Effect of Ion Implantation and Other Surface Treatments", *Journal of Applied Physics*, Vol. 53, pp. 3576-3580, 1982.
- <sup>4</sup> K-S Chen, A. Ayon, and S.M. Spearing, "Tailoring and Testing the Fracture Strength of Silicon at the Mesoscale", submitted to the *Journal of American Ceramic Society*, 1997.
- <sup>5</sup> K-S Chen, A. Ayon, and S.M. Spearing, "Silicon Strength Testing for Mesoscale Structural Applications", Symposium N3.8, MRS Spring Meeting, April 13-17, San Francisco, CA, 1998.
- <sup>6</sup> P.B. Hirsch, S.G. Roberts, J. Samuels, and P.D. Warren, "The Ductile-to-Brittle Transition in Silicon", *Mechanics of Creep Brittle Materials -1*, A. Cocks and A. Ponter, Eds., Elsevier Applied Science, 1988.
- <sup>7</sup> H.E. Evans, "Mechanisms of Creep Fracture", Elsevier Applied Science, 1984.
- <sup>8</sup> M. Ashby, H. Frost, "Deformation-Mechanism Maps - The Plasticity and Creep of Metals and Ceramics", Pergamon Press, 1982.
- <sup>9</sup> B. Wilshire, "Creep Deformation of Engineering Ceramics", *Mechanics of Creep Brittle Materials -1*, A. Cocks and A. Ponter, Eds., Elsevier Applied Science, 1988.
- <sup>10</sup> T. Courtney, "Mechanical Behavior of Materials", McGraw-Hill, 1990.
- <sup>11</sup> H. Alexander, P. Haasen, "Dislocations in the Diamond Structure", *Solid State Physics - Advances in Research and Applications*, F. Seitz, D. Turnbull, H. Ehrenreich, Academic Press, 1968.
- <sup>12</sup> M.M. Myshlyaev, V.I. Nikitenko, and V.I. Nesterenko, "Dislocation Structure and Macroscopic Characteristics of Plastic Deformation at Creep of Silicon Crystals", *Phys. Stat. Sol.*, Vol. 36, 1969.
- <sup>13</sup> T.A. Taylor, and C.R. Barrett, "Creep and Recovery of Silicon Single Crystals", *Material Science and Engine*, Vol. 10, pp. 93-102, 1972.
- <sup>14</sup> D. Lewis III, "Tensile Testing of Ceramics and Ceramic-Matrix Composites", Patricia Han, ASM International, 1992.
- <sup>15</sup> G.W. Hollenberg, G.R. Terwilliger, and R.S. Gordon, "Calculation of Stresses and Strains in Four-Point Bending Creep Tests", *Journal of the American Ceramic Society*, Vol. 54, no. 4, pp. 196-199, 1971.
- <sup>16</sup> S. Sato, M-C Chu, Y. Kobayashi, and K. Ando, "Influence of SiC Particle Size on Creep Properties of Si<sub>3</sub>N<sub>4</sub>/SiC Composite Ceramics", *Journal of the Ceramic Society of Japan*, Vol.

---

104, no. 11, pp. 1035-1039, 1996.

- <sup>17</sup> B. Wilshire and H. Jiang, "Deformation and Failure Processes During Tensile Creep of Sintered Silicon Carbide", *British Ceramic Transactions*, Vol. 93, no. 6, pp. 213-218, 1994.
- <sup>18</sup> K. Jakus and S. Wiederhorn, "Creep Deformation of Ceramics in Four-Point Bending", *Journal of the American Ceramic Society*, Vol. 71, no. 10, pp. 832-836, 1988.
- <sup>19</sup> P. Talty and R. Dirks, "Determination of Tensile and Compressive Creep Behaviour of Ceramic Materials From Bend Tests", *Journal of Materials Science*, Vol. 13, pp. 580-586, 1978.
- <sup>20</sup> Z. Jou, A. Virkar, and R. Cutler, "High Temperature Creep of SiC Densified Using a Transient Liquid Phase", *Journal of Material Research*, Vol. 6, No. 9, pp. 1945-1949, September 1991.
- <sup>21</sup> T.-J. Chuang, "Estimation of Power-Law Creep Parameters from Bend Test Data", *Journal of Materials Science*, Vol. 21, pp. 165-175, 1986.
- <sup>22</sup> F.I. Baratta, "Requirements for Flexural Testing of Brittle Materials", *Methods for Assessing the Structural Reliability of Brittle Materials*, ASTM STP 844, S.W. Freiman and C. M. Hudson, Eds., American Society for Testing and Materials, Philadelphia, 1984, pp. 194-222.
- <sup>23</sup> K-S Chen, "Materials Characterization and Structural Design of Ceramic Micro Turbomachinery", MIT PhD Thesis, February 1999.
- <sup>24</sup> C.R. Calladine, "Plasticity for Engineers", Ellis Horwood Limited, 1985.
- <sup>25</sup> D. Hull, and D.J. Bacon, "Introduction to Dislocations - 3<sup>rd</sup> Edition", International Series on Materials Science and Technology, Vol. 37, pp. 207-209, Pergamon Press, 1984.
- <sup>26</sup> J.E. Shigley, and C.R. Mischke, "Mechanical Engineering Design - 5<sup>th</sup> Edition", pp. 73-74, McGraw-Hill, Inc., 1989.
- <sup>27</sup> A.H. Epstein et.al., "Micro Gas Turbine Generators and Technology Foundations for Micro Heat Engines - A Presentation to the MIT-Army Research Office", April 1999.
- <sup>28</sup> M.G. Jenkins, S.M. Wiederhorn, R.K. Shiffer, "Creep Testing of Advanced Ceramics", Mechanical Testing Methodology for Ceramic Design and Reliability, Marcel Dekker, Inc., pp. 171-222, 1998.
- <sup>29</sup> K.D. Debshutz, B. Caspers, G.A. Schneider, and G. Petzow, "Critical Evaluation of the Compression Creep Test", *Journal of the American Ceramic Society*, Vol. 76, pp. 2468-2474, 1993.
- <sup>30</sup> S.M. Wiederhorn, R.F. Krause, Jr. and J. Sun, "Coal Slag Penetration in a Magnesium-Chromite Refractory", *Bulletin of the American Ceramic Society*, Vol. 67, pp. 1201-1210, 1988.
- <sup>31</sup> R.F. Krause, Jr., "Compressive Strength and Creep Behavior of a Magnesium Chromite Refractory", *Ceram. Eng. Sci. Proc.*, Vol. 7, pp. 220-228, 1986.
- <sup>32</sup> F.F. Lange, B.I. Davis and D.R. Clarke, "Compressive Creep of Si<sub>3</sub>N<sub>4</sub> Alloys, Part 1 Effect of Composition", *Journal of Material Science*, Vol. 15, pp. 601-610, 1980.
- <sup>33</sup> S.M. Wiederhorn, D.E. Roberts, T-J Chuang, and L. Chuck, "Damage Enhanced Creep in Siliconized Silicon Carbide: Phenomenology", *Journal of the American Ceramic Society*, Vol. 71, pp. 602-608, 1988.
- <sup>34</sup> W.E. Luecke, S.M. Wiederhorn, B.J. Hockey, R. Krause, Jr. and G.G. Long, "Cavitation Contributes Substantially to Tensile Creep in Silicon Nitride", *Journal of the American Ceramic Society*, Vol. 78, pp. 2085-2096, 1995.
- <sup>35</sup> R. Becker, J.F. Butler, Jr., H. Hu, and L.A. Lalli, "Analysis of an Aluminum Single Crystal with Unstable Initial Orientation (001) [100] in Channel Die Compression", *Metallurgical Transactions A*, Vol. 22A, PP. 45-58, 1991.



# THESIS PROCESSING SLIP

FIXED FIELD: #. \_\_\_\_\_ name \_\_\_\_\_

index \_\_\_\_\_ biblio \_\_\_\_\_

► COPIES: Archives Aero Dewey Eng Hum  
Lindgren Music Rotch Science

TITLE VARIES: ►  \_\_\_\_\_

NAME VARIES: ►  Scott

IMPRINT: (COPYRIGHT) \_\_\_\_\_

► COLLATION: 136 l

► ADD: DEGREE: \_\_\_\_\_ ► DEPT.: \_\_\_\_\_

SUPERVISORS: \_\_\_\_\_

NOTES:

cat'r:

date:

page:

► DEPT: M.E. ► J142

► YEAR: 1999 ► DEGREE: S.M.

► NAME: WALTERS, Douglas S.